Chair of Physical Metallurgy and Metallic Materials

Doctoral Thesis

Austenite memory and spontaneous recrystallization and its influence on the martensitic substructure of a PH 15-5 steel during solution annealing

Dipl.-Ing. Dominik Brandl

October 2019

Preface

The present work is submitted for the purpose of obtaining the degree "Doktor der montanistischen Wissenschaften" at the "Montanuversität Leoben" and was supervised by ao. Univ. Prof. DI Dr. mont Reinhold Ebner. The project was realized in the time between October 2015 and March 2019 with project partners voestalpine Böhler Aerospace GmbH & Co KG and voestalpine Böhler Edelstahl GmbH & Co KG. The research leading to these results has received funding from Take Off program. Take Off is a Research, Technology and Innovation Funding Program of the Austrian Federal Ministry for Transport, Innovation and Technology (BMVIT) (850471). The Austrian Research Promotion Agency (FFG) has been authorized for the Program Management.

Affidavit

I declare on oath that I wrote this thesis independently, did not use other than the specified sources and aids, and did not otherwise use any unauthorized aids.

I declare that I have read, understood, and complied with the guidelines of the senate of the Montanuniversität Leoben for "Good Scientific Practice".

Furthermore, I declare that the electronic and printed version of the submitted thesis are identical, both, formally and with regard to content.

Date: 31.10.2019

Signature Author
Dominik, Brandl
Matriculation number: 01035018

Acknowledgement

I want to gratefully acknowledge ao. Univ. Prof. DI Dr. mont. Reinhold Ebner for the opportunity to write the PhD thesis at the Materials Center Leoben Forschung GmbH, his supervision and for numerous discussions shaping and improving the present work.

Additionally, I like to acknowledge Assoc. Prof. Dr. Jozef Keckes for valuable discussions and the supervision of the present work.

I like to gratefully thank DI Dr. mont. Gerald Ressel for his effort and the time he invested in the supervision of the PhD thesis and the associated project SmartForge containing numerous discussions with very helpful feedback.

Furthermore, I would like to acknowledge my PhD-colleagues and friends DI Joseph Pörnbacher and DI Dr. mont. Annika Eggbauer for numerous constructive discussions. Especially, I would like to thank DI Stephan Reisinger for the most productive coffee breaks.

Additionally, I would like to kindly acknowledge my laboratory-colleagues Bernhard Sartory, Bernhard Friessnegger, Katharina Auinger and Edgar Stipsits enabling the best results with competent discussions and test executions.

All student co-workers contributing to this thesis are acknowledged, especially Lukas Höfler for his support during the whole project.

I want to thank the project partners of voestalpine Böhler Aerospace GmbH & Co KG and voestalpine Böhler Edelstahl GmbH & Co KG. The constructive and friendly cooperation of Univ.-Prof. Dipl.-Ing. Dr.techn. Martin Stockinger and DI Sarah Ploberger is especially highlighted.

Additionally, I like to acknowledge DI Dr. mont. Stefan Marsoner for the opportunity to work in his research group and the support in the early days as student assistant.

Finally, I'd like to thank my parents for the strong and continual support during my academic education and the journey of life in general.

The art and science of asking questions is the source of all knowledge.

-Thomas Berger (American novelist, 1924 - 2014)

Abstract

The aim of the present work is to describe the microstructural evolution of austenite in PH 15-5 during solution annealing and its influence on the evolving martensitic substructure.

In recent research, questions such as the relationship between austenite grain size and martensitic substructure are not conclusively clarified. However, the martensitic substructure such as packet-, block- and subblock-size and the distribution of martensitic variants affect the mechanical properties of a component and is therefore a crucial parameter in order to optimize strength and fracture toughness.

Therefore, the formation of austenite and its transformation to martensite during solution annealing is investigated by means of state-of-the-art *in-situ* observation techniques such as high temperature electron backscatter diffraction, high temperature x-ray diffraction, high temperature confocal laser scanning microscopy and dilatometry measurements.

During solution annealing, phenomena such as the so-called "austenite memory effect" and "spontaneous recrystallization" are observed for the first time in PH 15-5. These phenomena affect the inner structure of austenite concerning dislocation density, twin boundaries and grain size and are rarely investigated *in-situ* in literature up to now. However, in this thesis the formation mechanism of the austenite memory effect in PH 15-5 is determined and its influence on spontaneous recrystallization and furthermore on the developing martensitic substructure is investigated. Therefore, a novel approach concerning a quantitative martensite variant indexing for material states with a variation in austenite grain size was carried out, revealing a more homogenous variant distribution for larger austenite grains in combination with a smaller martensite block size.

The observations indicate a direct correlation between martensite variant distribution and martensite block size. It is assumed that if the range of the elastic stress field, induced by the first forming martensite variants, exceeds austenite grain boundaries, strain compensation after martensitic transformation proceeds over grain boundaries and neighbouring austenite grains. Therefore, a smaller austenite grain size leads to an inhomogeneous martensite variant distribution and to a larger martensite block size.

Kurzfassung

Ziel der vorliegenden Arbeit ist es, die mikrostrukturelle Entwicklung von Austenit in PH 15-5 während des Lösungsglühens und deren Einfluss auf die entstehende martensitische Substruktur zu beschreiben.

Im aktuellen Kenntnisstand zur martensitischen Umwandlung finden sich Lücken, wie zum Beispiel die Korrelation zwischen Austenitkorngröße und martensitischer Substruktur. Zur martensitischen Substruktur zählen die Paket-, Block- und Subblockgröße sowie die Martensitvariantenverteilung. Diese beeinflussen die mechanischen Eigenschaften eines Bauteils und sind daher ein entscheidender Parameter zur Optimierung von Festigkeit und Bruchzähigkeit.

Aus diesem Grund beschäftigt sich die vorliegende Arbeit mit der mikrostrukturellen Charakterisierung des Austenits und seiner Umwandlung zu Martensit während des Lösungsglühens und der anschließenden Abkühlung. Diese Charakterisierung wurde mit Hilfe moderner *in-situ* Untersuchungstechniken wie Hochtemperatur-Elektronenrückstreu-Diffraktion, Hochtemperatur-Röntgenbeugung, Hochtemperatur-Laser-Scanning-Mikroskopie und Dilatometriemessungen durchgeführt.

Während des Lösungsglühens wurden in PH 15-5 erstmals Phänomene wie der sogenannte „Austenit-Memory-Effekt“ und „spontane Rekristallisation“ beobachtet. Diese Phänomene beeinflussen die innere Struktur von Austenit in Bezug auf dessen Versetzungsdichte, Zwillingsgrenzen und Korngröße und wurden in der Literatur bis jetzt erst selten durch *in-situ* Methoden untersucht. In dieser Arbeit wird der Bildungsmechanismus des Austenit-Memory-Effekts in PH 15-5 und dessen Einfluss auf die spontane Rekristallisation und die entstehende martensitische Substruktur untersucht. Hierfür wurde ein neuartiger Ansatz zur quantitativen Indizierung von Martensitvarianten für Materialzustände mit einer Variation der Austenitkorngröße entwickelt. Dieser ergab eine homogenere Variantenverteilung für größere Austenitkörner in Kombination mit einer kleineren Martensitblockgröße.

Die Beobachtungen zeigen eine direkte Korrelation zwischen der Martensitvariantenverteilung und der Martensitblockgröße. Es wird angenommen, dass, wenn die Reichweite des elastischen Spannungsfeldes, das durch die zuerst gebildeten Martensitvarianten induziert wird, die Austenitkorngrenzen überschreitet, die Dehnungskompensation nach der Martensitumwandlung über die Korngrenzen hinweg auch in den benachbarten Austenitkörner

erfolgt. Eine geringere Austenitkorngröße führt demnach zu einer inhomogenen Martensitvariantenverteilung und zu einer größeren Martensitblockgröße.

Abbreviations

fcc	Face centered cubic
bcc	Body centered cubic
bct	Body centered tetragonal
γ	Austenite
α'	Martensite
θ	Cementite
OR	Orientation relationship
KS	Kurdjumov-Sachs
NW	Nishiyama-Wassermann
GT	Greninger-Troiano
V1 - V24	Martensitic variant 1 - 24
P1 - P4	Martensitic packet 1 - 4
B1 - B3	Martensitic block 1 - 3
EBSD	Electron backscatter diffraction
IPF	Inverse pole figure
IQ	Image quality
KAM	Kernel average misorientation
CI	Confidence index
OIM	Orientation imaging micrograph
HT-CLSM	High temperature confocal laser scanning microscopy
M_s	Martensite start temperature

M_f	Martensite finish temperature
A_1	Equilibrium temperature between $\alpha + \theta$ and $\alpha + \gamma$
A_3	Equilibrium temperature between $\alpha + \gamma$ and γ
EAR	Experimental as-received
IAR	Industrial as-received
AS	After solution annealing
CG	Coarse grain
LAGB	Low angle grain boundary
GND	Geometrically necessary dislocations
ω	Angular deviation between one hexagonal EBSD pixel and its neighbors for the calculation of the KAM

Formula symbols

$\overline{T}_n$	First Input OR (i.e. KS OR) for the iterative calculation of an OR
$T_{n+1,k}$	Output OR of the nth iteration for the kth grain pairing
C_i , C_j	Symmetry operators of the cubic crystal system
M_k	Misorientation angle between the kth neighboring martensitic grains obtained by EBSD measurement
$\overline{T}_{n+1}$	Average OR calculated for all intergranular misorientations M_k used as input of subsequent iteration steps
λ	Wavelength
d	Lattice spacing
θ	Scattering angle
θ_B.	Bragg angle
x, y	Real space coordinates
θ', ρ'	Hough space coordinates
ρ_{GND}	Geometrically necessary dislocation density
$EBSD_{Step\ Size}$	Step size of the EBSD measurement
b	Burgers vector
V_1	Number of votes for the most likely solution from the indexing algorithm of the EBSD measurement
V_2	Number of votes for the second likely solution from the indexing algorithm of the EBSD measurement
V_{ideal}	Total number of possible votes for all solutions
$\bar{d}_{num.fract.}$	Mean martensite block size according to number fraction

$\bar{d}_{ar.fract.}$	Mean martensite block size according to area fraction
d_i	Equivalent circle diameter of the ith martensite block
A_i	Area of the ith martensite block
N	Total number of all detected martensite blocks
$GS_{\mu m}^{+/-}$	Error bars of the grain size in µm
n_G	Number of grains in a grain size measurement
γ_{SFE}	Stacking fault energy
F_N	Driving force for recrystallization
ρ	Dislocation density
G	Shear modulus
GS_{ASTM}	Grain size according to ASTM number
$GS_{\mu m}$	Grain size in µm
f_i	Number fraction of the ith martensitic variant

Table of Contents

1 Introduction

1.1 History of PH 15-5

PH 15-5 is a precipitation hardenable steel grade and belongs to the group of low carbon martensitic stainless steels, i.e. steels with 11.5 - 16 m.% Cr, 4 - 8 m.% Ni and a carbon content <0.07 m.% [1].

The alloy design of the low carbon martensitic stainless steel is based on the ternary Fe-Cr-Ni system with additions of Mn, Mo and Si. A fine balancing of austenite and ferrite stabilizing elements is necessary in order to fulfil the requirements on the alloy system. This is necessary to avoid the formation of δ-ferrite during solution annealing, to avoid reaustenitization during tempering at 700 °C for 5 h as well as to ensure an almost complete martensitic transformation by keeping the martensite start temperature (M_s) above 200 °C on the other [2]. Therefore, Irvine et al. [2] postulated the steel composition Fe–0.1C–12Cr–2Ni–1.5Mo–0.3V (m.%) in the 1960s exhibiting good combination of strength and toughness.

In order to enhance corrosion resistance, more Cr was added to the alloy systems which requires additional austenite stabilizing elements. One of the most effective austenite stabilizing element is C but it produces $M_{23}C_6$ with Cr, which reduces the Cr content in the matrix, thus, reducing the corrosion resistance of the alloy. Therefore, Ni is chosen as the most promising substitution for C. Another beneficial effect of Ni is the increase of impact toughness of fresh formed martensite [1,3]. In the mid-60s the Swedish steel manufacturers Bofors and Avesta reduced the C content to 0.06 m.% and developed soft martensitic stainless steel for pressure vessel applications.

Typical for this alloy group is the small amount of retained austenite and the formation of reverted austenite during inter-critical annealing which is beneficial for toughness properties [1,4,5]. Originating from these so-called soft martensitic steels, precipitation hardenable steels evolved by adding significant amounts of Cu, Mo or Nb in order to enable precipitation hardening. PH 15-5 contains approximately 3.3 m.% Cu in order to enable precipitation hardening and is in the focus of steel research for aerospace industry since the late 1960s [6]. Today, it is a well established steel grade for structural components in aircrafts due to its outstanding combination of strength, toughness and corrosion resistance [7]. Nevertheless, PH 15-5 is still topic of recent research because of its complex composite microstructure of martensite, austenite and fine dispersed precipitations [5,8–12].

Besides nm-sized Cu precipitations embedded in a low carbon martensitic matrix, the microstructure of PH 15-5 contains fine lamellar austenite and NbC in order to suppress grain coarsening during hot deformation and subsequent heat treatment [8]. The heat treatment consists of solution annealing at approximately 1030 °C for 0.5 h in order to dissolve Cu precipitates and create a defined precipitation state for the subsequent annealing treatment. Furthermore, solution annealing is the last austenitization treatment and therefore it is a crucial step in order to adjust austenite grain size and the evolving martensitic substructure of the final component [13–19]. During precipitation hardening, Cu precipitates form and the dislocation density of martensite decreases [1,5,8,10,20,21]. Additionally, fine lamellae of reverted austenite forms on martensite lath and block boundaries enhancing toughness properties [1,3,22].

1.2 Motivation of the work

Pushing the limits of component properties for the next generation of aircrafts requires a detailed understanding of microstructural development of austenite and the evolving martensitic microstructure in order to optimize the production and component properties. The inner structure of austenite, such as grain size, twin size and dislocation density affects the evolving martensite substructure size [23], which is a crucial parameter for the mechanical properties of the final component [13–19]. Especially, the martensite block size influences the fracture toughness of cleavage fracture [24] and is therefore an essential parameter for the optimization of the final component with regard to safety issues.

The investigation of the interplay between austenitic microstructure during solution annealing and martensitic structure after heat treatment is related to the state of the art of investigation techniques. Previous studies investigated the austenite transformation to martensite after heat treatment by using optical light microscopy or transmission electron microscopy [25–27]. Valuable information concerning the orientation relationship (OR) between martensite and retained austenite or the formation mechanism of austenite after inter-critical annealing are gained from these investigations [26,28–30]. However, these investigation methods require the presence of retained austenite and crystallographic information at the scale of one austenite grain could not be obtained.

During the last two decades, electron backscatter diffraction (EBSD) has been widely used in order to measure precise crystallographic orientations

over a wide range [31–33]. Actually, the EBSD-data enable the detailed examination of the martensitic substructure such as packets, blocks and subblocks by variant identification methods [24,34,43,44,35–42]. These investigations opened a new insight in the hierarchical structure of martensite and enabled the correlation of mechanical properties with specific parts of the martensitic substructure [15,17,24,43–45].

Furthermore, new algorithms are able to reconstruct the prior austenite grain orientation out of the martensite crystal orientation due to the strict OR between martensite and austenite [46–48]. However, the exact inner structure of austenite (e.g. misorientation) cannot be investigated by such *ex-situ* investigations or reconstruction methods. Recently, high temperature *in-situ* EBSD is developed enabling the direct observation of austenitization and martensite formation over a wide surface area [49–51].

Therefore, the recent work combines the previously discussed investigation techniques with high temperature *in-situ* EBSD measurements in order to examine the microstructural development of austenite and its influence on the evolving martensite substructure during solution annealing of PH 15-5. Austenitization phenomena such as austenite memory effect and spontaneous recrystallization are evidenced for the first time in the PH 15-5 alloy. Furthermore, the block size and variant distribution of the evolving martensite substructure is determined and correlated to the prior austenite grain size. This examination reveals a finer martensite block size in combination with a more homogeneous variant distribution for a coarser austenite grain.

The results presented in this work expand the understanding of the formation of austenite microstructure during solution annealing of PH 15-5 and its influence on the evolving martensite substructure. Furthermore, new insights of the interplay between austenite grain size and martensite block size are presented, which may help to adapt the martensite block size and therefore optimize the mechanical properties of the final component.

2 Fundamentals

The following chapter deals with the fundamental literature in order to discuss the development of austenite and martensite microstructure during solution annealing of PH 15-5.

2.1 Martensite

Martensite is a phase formed by a diffusionless allotriomorphic transformation in numerous types of alloys [52]. This chapter focusses on crystallographic relationships of martensite in steels and its hierarchical substructure. Furthermore, the inner structure and strength of austenite is discussed as influencing parameter to the martensite substructure.

2.1.1 Crystallography of martensite

Originating from the diffusionless transformation of martensite, a strong orientation relationship (OR) between prior austenite and martensite is present resulting in a hierarchical substructure [53]. In the following chapters, martensite is described in a crystallographic point of view especially concerning OR, formation and nomenclature of the hierarchical substructure.

2.1.1.1 Orientation relationship

For transformations of the crystal structure such as coherent precipitation reactions or displacive phase transformations, the OR determine the crystallographic orientation of the daughter phase with respect to the parent phase by indicating a pair of parallel planes and directions [53,54]. Therefore, each OR has a specific number of possible crystal orientations for the daughter phase out of one parent crystal orientation, i.e. variants. In the following, the most popular OR for austenite and martensite are presented.

Kurdjumov-Sachs (KS)

KS is the most common OR to describe the martensitic transformation $\gamma \rightarrow \alpha'$ in low carbon steel [53,55]. It is assumed that closed packed planes and directions of austenite and martensite are parallel, i.e. $\{111\}_{\gamma}||\{011\}_{\alpha'}$ and $\langle 011\rangle_{\gamma}||\langle 111\rangle_{\alpha'}$.This assumption leads to 24 possible martensite variants out of one austenite grain by cyclic variations of non-equivalent planes and directions, shown in Table 1. The characteristic pattern in a (001) pole figure for a KS OR is given in Fig. 1 and Fig. 2c with a numeration of each reflex

of a martensite variant. The different colors of the martensite reflexes (squares) correspond to different habit planes (triangles) and therefore to different martensite packets, which are further described in chapter 2.1.1.3. Additionally, a detailed description of the martensitic substructure on the basis of Table 1 is given in chapter 2.1.1.3 of this work.

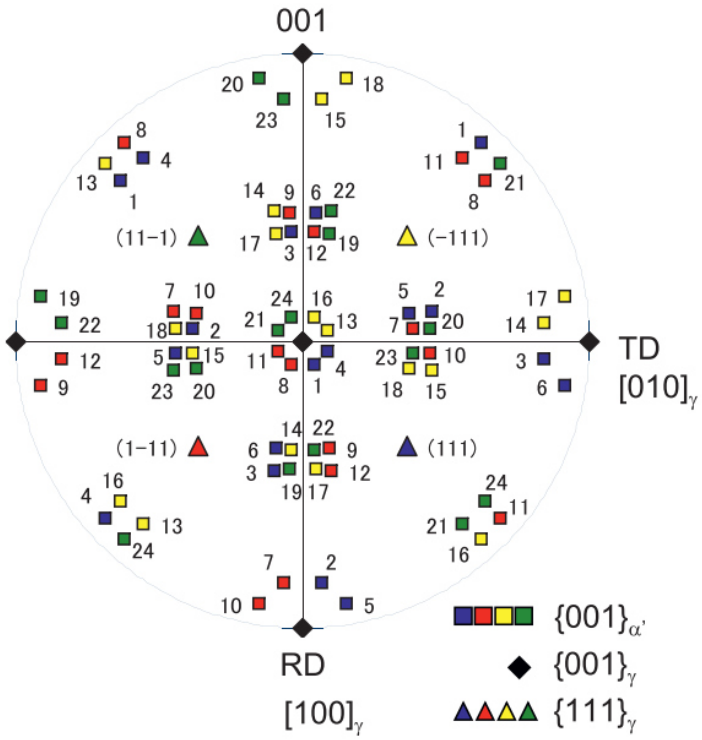

Fig. 1: Characteristic pattern of martensite reflexes (colored squares) out of one austenite crystal orientation (black tilted squares) in a (001) pole figure for KS OR. The numbering of each reflex corresponding to a KS variant of martensite in a (001) pole figure with respect to the prior austenite crystal orientation (black). Variants corresponding to the habit plane (i.e. corresponding to the same packet) are illustrated with the same color (blue, red, yellow, green) [56]*. For details regarding the numbering see also Table 1.*

Nishiyama-Wassermann (NW)

For steels with carbon content higher than 0.8 m.%, the NW OR is often used to describe crystallographic relations between martensite and austenite [52,57]. It has in common with KS OR that closed packet planes are parallel but distinguishes from KS OR by the assumption that the parallel directions are $\langle 011\rangle_{\gamma}||\langle 100\rangle_{\alpha'}$ [57]. Therefore, the cyclic variation of non-equivalent planes and directions causes only 12 possible variants for martensite with NW OR out of one austenite grain. The characteristic pattern in pole figures of NW OR is illustrated in Fig. 2b.

Greninger-Troiano (GT)

Concerning the resulting pattern in pole figures, the GT OR is between KS and NW and therefore is used to describe OR between austenite and martensite more close to real experimental data for some alloy types [58]. The GT OR is defined as $\{111\}_{\gamma}||\{011\}_{\alpha'}$ and $\langle 123\rangle_{\gamma}||\langle 133\rangle_{\alpha'}$ which is equal to a 1.85° deviation from $\langle 011\rangle_{\gamma}||\langle 111\rangle_{\alpha'}$ [43,59]. The GT OR causes also 24 possible variants for martensite illustrated in (001) pole figure in Fig. 2d. The presented OR are models based on crystallographic assumptions and therefore real measurements may deviate as it is illustrated in Fig. 2.

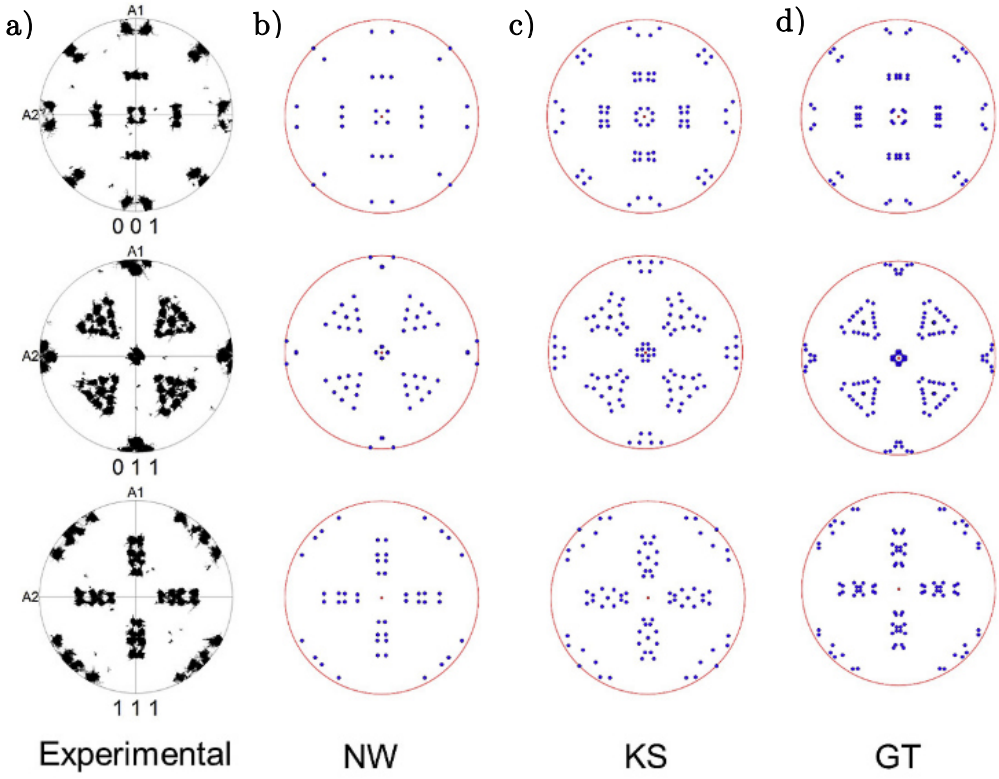

Fig. 2: Comparison of experimental data, obtained from Zilnyk et al. [60] *in a binary Fe-Ni alloy with 31.5 m.% Ni, with the most popular OR models for the martensite in steel. Each model deviates slightly from the experimental OR.*

Table 1: The 24 crystallographic variants (V1 - V24) of KS OR between austenite (γ) and martensite (α′) with indicated parallel planes and directions between parent and daughter phase according to [53]*. The 24 variants are divided into 4 packets (P1 - P4), corresponding to the same habit plane in austenite, and subdivided into 3 blocks per packet (B1 - B3), corresponding to the Bain axis of the martensitic transformation.*

Variant	Packet	Parallel plane	Block	Parallel direction
V1	P1	$(111)_\gamma \| (011)_{\alpha'}$	B1	$[\bar{1}01]_\gamma \| [\bar{1}\bar{1}1]_{\alpha'}$
V2			B2	$[\bar{1}01]_\gamma \| [\bar{1}1\bar{1}]_{\alpha'}$
V3			B3	$[01\bar{1}]_\gamma \| [\bar{1}\bar{1}1]_{\alpha'}$
V4			B1	$[01\bar{1}]_\gamma \| [\bar{1}1\bar{1}]_{\alpha'}$
V5			B2	$[1\bar{1}0]_\gamma \| [\bar{1}\bar{1}1]_{\alpha'}$
V6			B3	$[1\bar{1}0]_\gamma \| [\bar{1}1\bar{1}]_{\alpha'}$
V7	P2	$(1\bar{1}1)_\gamma \| (011)_{\alpha'}$	B1	$[10\bar{1}]_\gamma \| [\bar{1}\bar{1}1]_{\alpha'}$
V8			B2	$[10\bar{1}]_\gamma \| [\bar{1}1\bar{1}]_{\alpha'}$
V9			B3	$[\bar{1}\bar{1}0]_\gamma \| [\bar{1}\bar{1}1]_{\alpha'}$
V10			B1	$[\bar{1}\bar{1}0]_\gamma \| [\bar{1}1\bar{1}]_{\alpha'}$
V11			B2	$[011]_\gamma \| [\bar{1}\bar{1}1]_{\alpha'}$
V12			B3	$[011]_\gamma \| [\bar{1}1\bar{1}]_{\alpha'}$
V13	P3	$(\bar{1}11)_\gamma \| (011)_{\alpha'}$	B1	$[0\bar{1}1]_\gamma \| [\bar{1}\bar{1}1]_{\alpha'}$
V14			B2	$[0\bar{1}1]_\gamma \| [\bar{1}1\bar{1}]_{\alpha'}$
V15			B3	$[\bar{1}01]_\gamma \| [\bar{1}\bar{1}1]_{\alpha'}$
V16			B1	$[\bar{1}01]_\gamma \| [\bar{1}1\bar{1}]_{\alpha'}$
V17			B2	$[110]_\gamma \| [\bar{1}\bar{1}1]_{\alpha'}$
V18			B3	$[110]_\gamma \| [\bar{1}1\bar{1}]_{\alpha'}$
V19	P4	$(11\bar{1})_\gamma \| (011)_{\alpha'}$	B1	$[\bar{1}10]_\gamma \| [\bar{1}\bar{1}1]_{\alpha'}$
V20			B2	$[\bar{1}10]_\gamma \| [\bar{1}1\bar{1}]_{\alpha'}$
V21			B3	$[0\bar{1}\bar{1}]_\gamma \| [\bar{1}\bar{1}1]_{\alpha'}$
V22			B1	$[0\bar{1}\bar{1}]_\gamma \| [\bar{1}1\bar{1}]_{\alpha'}$
V23			B2	$[101]_\gamma \| [\bar{1}\bar{1}1]_{\alpha'}$
V24			B3	$[101]_\gamma \| [\bar{1}1\bar{1}]_{\alpha'}$

2.1.1.2 Crystallographic interpretation of the martensitic transformation

According to the presented OR, a pair of planes and directions of the parent crystal structure austenite (austenite - face centered cubic) and the daughter crystal structure (martensite - body centered cubic) are parallel. This requirement leads to the crystallographic interpretation of the martensitic transformation and is discussed in this chapter for the KS OR.

The face centred cubic (fcc) crystal structure is also interpretable as body centered tetragonal (bct) crystal structure as it is illustrated in Fig. 3. The lower symmetry of bct compared to fcc is not practicable for classical crystallographic interpretations but elucidate the relation of closed packed planes and directions in fcc and bct before martensitic transformation. The closed packed plane $(011)_{\mathrm{bct}}$ is obviously parallel to the closed packed plane $(111)_{\mathrm{fcc}}$ as well as the closed packed directions $[\bar{1}\bar{1}1]_{\mathrm{bct}} \parallel [\bar{1}01]_{\mathrm{fcc}}$ are parallel as highlighted in Fig. 3.

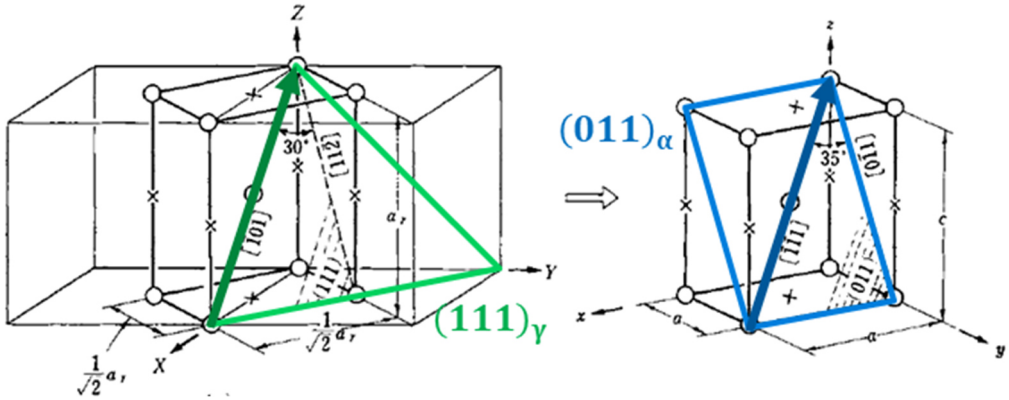

Fig. 3: Pair of parallel planes in fcc and bct crystal structure before martensitic transformation. The martensitic transformation causes a compression of bct along the z-axis (i.e. Bain axis) and an expansion along the x and y axis (i.e. Bain strain) (Adaption of Nishiyama et al. [52]).

The martensitic transformation causes a shrinkage of the bct unit cell along the longest side (z axis in Fig. 3) and an expansion in the other two directions (x and y axis in Fig. 3) which is called Bain strain [54,61,62]. In this scenario, a transformation from bct to an ideal body centered cubic (bcc) crystal structure without tetragonal distortion is assumed. Therefore, the tilt of the closed packed plane and direction changes for the bcc unit cell with respect to the fcc unit cell. In order to maintain the KS OR, i.e. closed packed planes and direction in fcc and bcc are parallel, the bcc unit cell rotates with respect to the fcc unit cell, as it is schematically illustrated in Fig. 4. The highlighted planes and directions, $(011)_{\alpha'} \parallel (111)_{\gamma}$ $[\bar{1}\bar{1}1]_{\alpha'} \parallel [\bar{1}01]_{\gamma}$ are corresponding to KS variant 1 and are exact parallel. The bcc unit cell is slightly tilted forward and to the right side. A cyclic variation of planes and directions, as it is given in Table 1, leads to a different rotation of the bcc unit cell after martensitic transformation and therefore causes the characteristic pattern of martensite reflexes in pole figures (Fig. 1) [62]. The same principle is also valid for other OR but with other parallel planes and directions resulting in a different pattern of reflexes in pole figures (Fig. 2).

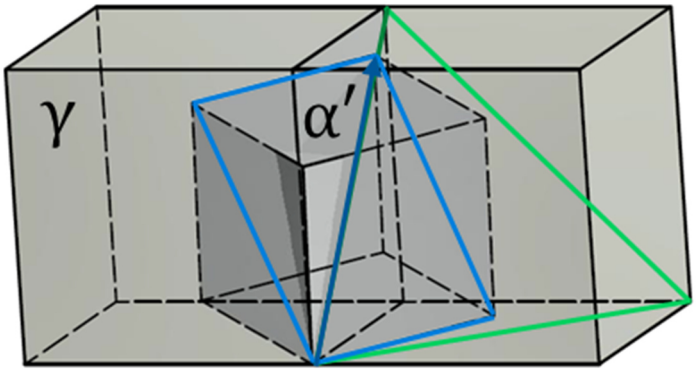

Fig. 4: A combination of Bain strain and OR leads to the rotation of martensite unit cell after martensitic transformation with respect to the prior austenite crystal orientation (here for KS variant 1) and causes the characteristic pattern of martensite reflexes in pole figures (Fig. 1, Fig. 2c and Fig. 12).

2.1.1.3 Hierarchical substructure

The hierarchical substructure of martensite is caused by the combination of the OR between austenite and martensite and an accommodation of elastic strain fields induced by the volume expansion due to martensite formation [13,14,62]. In the following the hierarchical substructure is explained according to KS OR illustrated in Table 1.

One austenite grain is partitioned into 4 different packets corresponding to the 4 different {111} habit planes. Furthermore, each packet is partitioned into 3 blocks corresponding to the 3 different compression directions of the Bain strain (i.e. the Bain axis). The crystallographic relationships of each substructure element are presented in Table 1. Each block contains a maximum of 2 different variants called subblocks exhibiting a specific twin relationship to each other. Eventually, each variant consists of crystallographic homogenous laths with only a few hundred nm in width [36,53,58].

This hierarchical structure is illustrated in Fig. 5. Packet and block boundaries are high angle boundaries (i.e. misorientation above 15°) with specific angles between variants depending on the exact OR between austenite and martensite. Subblock boundaries are low angle boundaries (i.e. misorientation below 15°) which exact misorientation is also depending on the exact OR. Lath boundaries exhibit the smallest angular misorientation which is below 5° inside one martensite variant [63]. This hierarchical substructure is identical for GT and NW OR but for NW no subblocks are present [43,44].

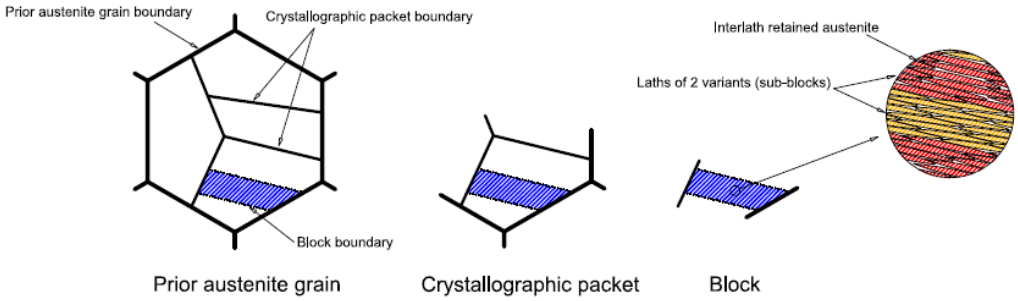

Fig. 5: Hierarchical substructure of martensite partitions one austenite grain into packets, blocks, subblocks and laths [64]. *The crystallographic relation of the different components of the martensitic substructure is given in Table 1 for KS OR.*

2.1.2 Influence of austenite strength on martensitic microstructure

As the austenite strength is one important determining factor for martensite formation, this chapter deals with the state-of-the-art of its effects on the martensite formation process and the evolving martensite packet, block and lath size.

The formation of martensite starts on austenite grain boundaries with the repeated nucleation of laths of the same martensite variant adjacent to each other. This transformation causes plastic deformation of austenite and fresh formed martensite as well as elastic strain accumulation inside the austenite grain due to the volume expansion of the ferritic phase [13]. In order to compensate the generated elastic strain, another martensite variant with oppositional strain direction is activated. This activation of different variants and induction of elastic strain fields proceed during the martensitic transformation and causes the formation of different packets and blocks. This process is called self-accommodation [13,14,65].

According to Qi et al. [62], self-accommodation promotes the formation of all 24 KS variants with equal volume fraction out of an ideal undeformed austenite grain and causes a martensitic transformation without net shear deformation and only net dilatation. The arrangement of packets, blocks and subblocks inside one austenite grain without a net shear component is illustrated in Fig. 6.

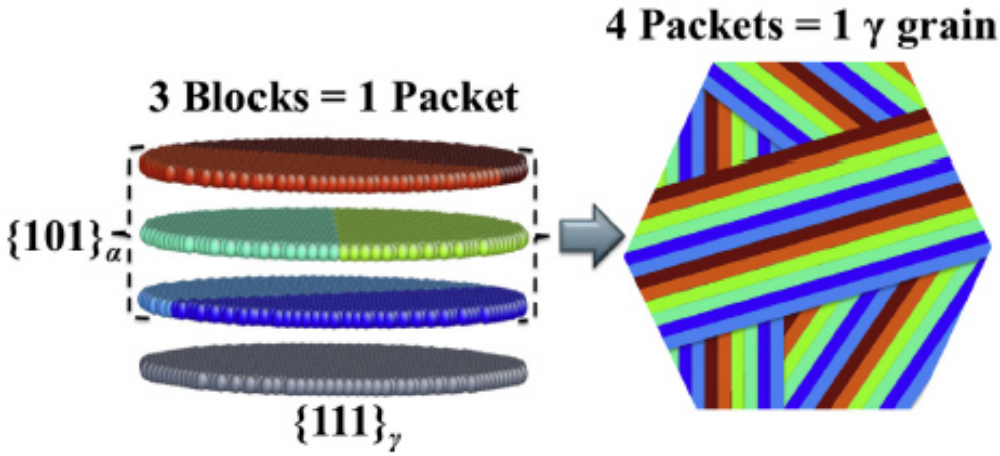

Fig. 6: Formation of 4 packets with 3 blocks containing 2 subblocks (illustrated with lighter and darker shades of red, green and blue) according to KS OR can cause a transformation from austenite to martensite without net shear component for equal volume fraction of all variants inside an austenite grain [62].

With increasing austenite strength, the plastic deformation of austenite is shifted to a higher stress level, resulting in a higher elastic stress in austenite adjacent to the fresh formed martensite variant. According to Morito et al. [13], the higher elastic stress causes a more frequent formation of martensite variants with opposite strain directions. Therefore, the martensite block size decreases with increasing austenite strength.

A similar trend has been observed by Morsdorf et al. [23] for the development of martensite lath size in a Fe–0.13C–5.1Ni–<0.002S–<0.002P (m.%) model alloy during cooling from austenitization temperature of 900 °C to room temperature. Morsdorf et al. [23] postulated that an increasing austenite strength causes a decrease of martensite lath size. As main influence on the austenite strength and further on the martensite lath size, the temperature range of the martensitic transformation (i.e. M_s and M_f), carbon content, prior austenite grain size and dislocation density are discussed.

Fig. 7a schematically shows the increase of the dislocation density ρ of austenite (γ) and martensite (α') due to the plastic deformation during martensitic transformation. The color code ranges from yellow for a low ρ to red for a high ρ and is a schematic representation of the mean ρ inside a γ grain or α' variant. Therefore, the austenite strength is increased with propagating martensite formation due to enhanced dislocation density and the lower temperature. Additionally, Morsdorf et al. [23] investigated the influence of grain size and carbon content on the austenite strength, which is illustrated in Fig. 7b. In Fig. 7b, the color code corresponds to the strength of austenite. The yellow color is the reference material state, which is the same as used

in Fig. 7a. The lighter red color represents an enhanced austenite strength due to a smaller austenite grain size, which is adjusted by a lower austenitization temperature of 850 °C of the Fe–0.13C–5.1Ni alloy. The darker red color represents a stronger increase of the austenite strength by a higher amount of carbon (Fe–0.3C–5Ni).

It is stated that higher strength of austenite due to higher dislocation density, lower temperature, higher carbon content or smaller austenite grain size causes a decrease in martensite lath size [23].

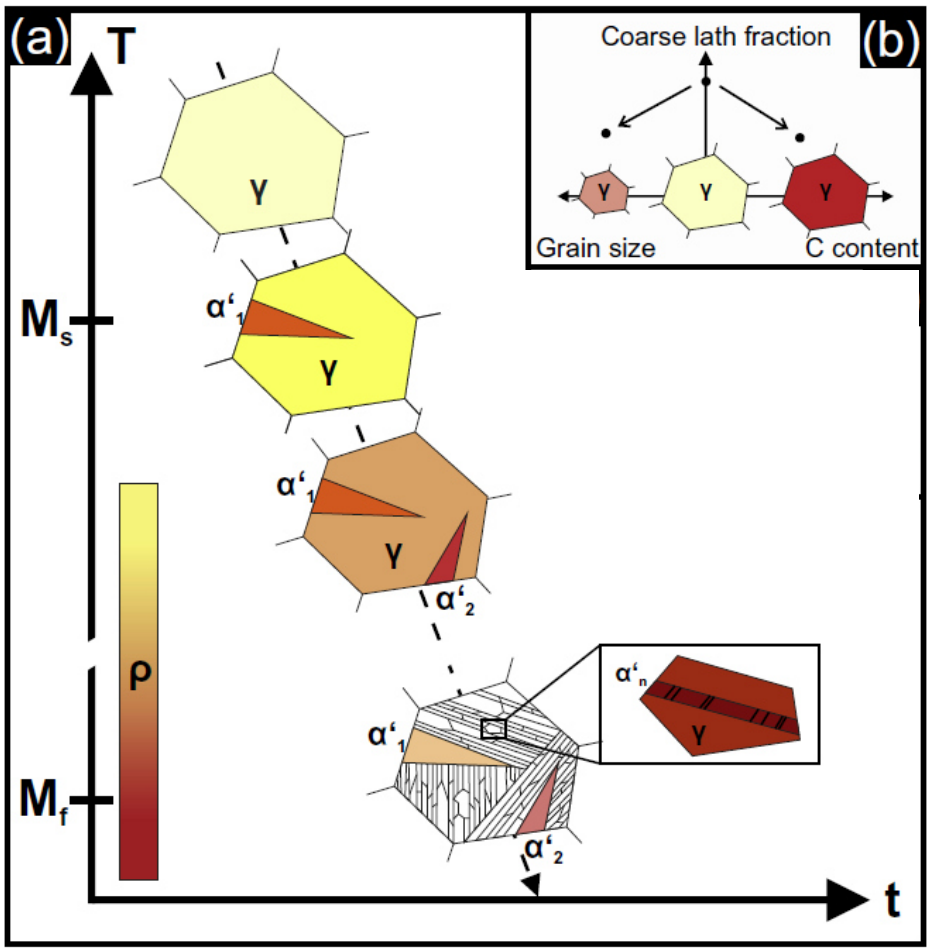

Fig. 7: Increasing γ strength by increasing dislocation density (a), decreasing grain size (b) and increasing carbon content (b) causes a decrease of the α′ lath size. (a) Schematic representation of the increasing dislocation density ρ (from yellow to red) during martensitic transformation of one γ grain between martensite start (M_s) and martensite finish temperature (M_f). Austenite is strengthened by the increasing dislocation density and decreasing temperature leading to a smaller martensite lath size. In (b) the color code from yellow to red represents the γ strength. A smaller γ grain is realized by a 50 °C lower austenitization temperature of the Fe–0.13C–5.1Ni alloy. A higher carbon content is realized by an adaption of the alloy composition (Fe–0.3C–5Ni) [23].

2.1.3 Inheritance of inner structure of austenite to martensite

Besides the austenite strength as a function of the martensitic transformation progress, described in the previous chapter, also the inner structure of initial austenite (i.e. austenite before martensitic transformation), such as misorientation, dislocation density and deformation textures, affect the martensitic substructure. Consequently, the following chapter deals with the inheritance of the inner structure of initial austenite to martensite.

Bhadeshia et al. [34,66,67] observed the inheritance of misorientation from austenite to bainite. In Fig. 8, a single crystal of austenite (a) partially transformed into bainite (b) is illustrated in a (100) pole figure. The misorientation of austenite is visible due to the spread of crystal orientations in the pole figure. In bainite, an identical orientation spread of approximately 10° is observed. He concluded that every distorted part of the austenite grain transforms with a strict OR between austenite and bainite and therefore inherits the crystal orientation spread from austenite to bainite. This conclusion is transferable to martensite because of the similar OR between austenite and martensite.

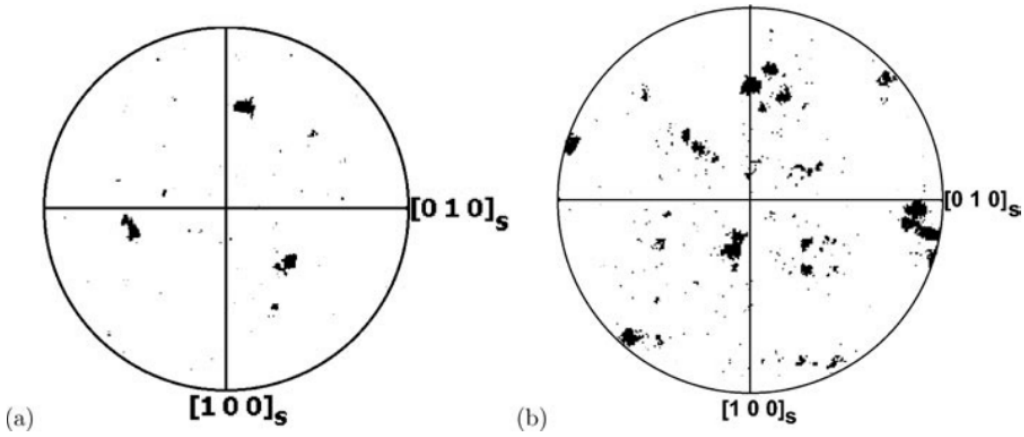

Fig. 8: Inheritance of misorientation from single crystalline austenite (a) to bainite (b) due to the strict OR observed by Bhadeshia et al. [66]*. This is indicated by the same range of the spread in austenite and bainite reflexes.*

The misorientation inside austenite is also related to its dislocation density [49,50,66]. In contrast to the previous chapter, here, differences in dislocation density of the initial austenite grain and not the increasing dislocation density during martensitic transformation are discussed. Such differences in dislocation density can be observed e.g. in partially recrystallized austenite. Shirazi et al. [50] investigated the evolving martensite microstructure of such partially recrystallized austenite. Fig. 9 summarizes the findings of binary Fe-Ni alloys with 18 to 23 m.% Ni. Shirazi et al. [50] claimed that martensite

transformed from dislocation rich austenite exhibit a finer microstructure size than martensite transformed from recrystallized austenite. Therefore, it can be conducted that the dislocation density of austenite affects the martensitic substructure size. This fact may be also attributed to the higher austenite strength due to work hardening. A quantitative relation between dislocation density and martensite packet, block and subblock size is not given by Shirazi et al. [50].

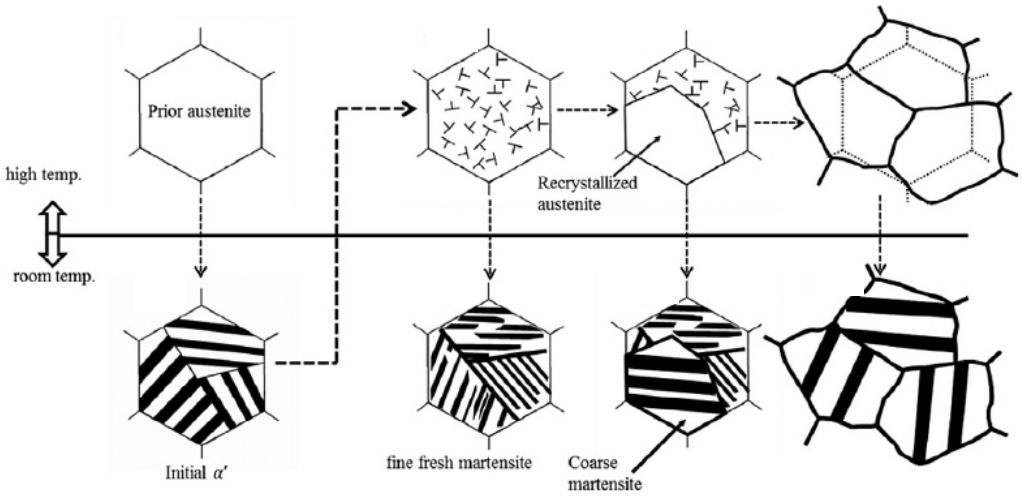

Fig. 9: Influence of prior austenite dislocation density on the evolving martensite microstructure size. Recrystallized prior austenite with lowered dislocation density promotes the formation of coarser martensite with respect to unrecrystallized austenite [50].

For martensite transforming from deformed austenite, self-accommodation causes the formation of preferred variants, blocks or packets in order to compensate the net shear component. Therefore, not all martensite variants are formed in the same amount, i.e. variant selection [35,39–42,68]. Miyamoto et al. [35] observed the preferred formation of single packets with increasing deformation of austenite previously to the martensitic transformation in low carbon lath martensite. Fig. 10 illustrates the martensite variant distribution (V1 to V24) for different deformation states of austenite. According to Miyamoto et al. [35], it is characteristic for lath martensite evolving from deformed austenite with an OR slightly different to KS. Therefore, packets are preferred with near {111} habit planes minimizing the total shear strain from deformation and martensitic transformation. Therefore, the deformation texture of austenite also inherits to the martensitic microstructure in a way that the variant distribution differs from undeformed austenite due to variant selection.

Finally, it can be summarized that the inner structure of austenite such as misorientation, dislocation density and deformation texture affect the

evolving martensitic substructure in terms of orientation spread of single variants, martensitic substructure size and formation of preferred packets (i.e. variant selection), respectively.

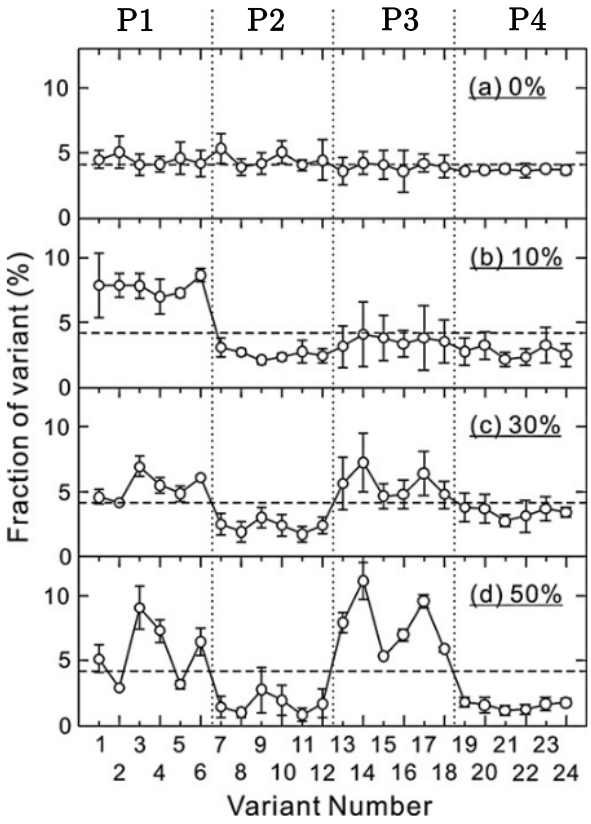

Fig. 10: Martensite variant distribution evolving out of 0 % (a), 10 % (b), 30 % (c) and 50 % uniaxially compressed austenite of a Fe–0.15C–3Ni–1.5Mn–0.5Mo steel at a deformation temperature of 700 °C and a strain rate of 1 s^{-1}, which is immediately after deformation quenched with He gas [35]. *Specific martensitic packets (P1 - P4) are formed dominantly for increasing compression strain. The figure is an adaption of* [35].

2.1.4 Martensite variant identification

The following chapter deals with the description of the identification approach of martensite variants used in the actual work and the limits and challenges of martensite variant identification in general.

2.1.4.1 Identification approach

In order to identify martensite variants, specific angles between martensite crystal orientation and prior austenite crystal orientation [24,67] or specific angles between different martensite crystal orientations [24,36,58] are compared with reference angles according to a reference OR. Therefore, it is

necessary to obtain the martensite crystal orientation, e.g. by EBSD measurements, as well as to choose a suitable reference OR. In literature, often ideal OR such as KS, NW or GT are used as reference OR [36,53,58]. However, comparing the experimental crystal orientation with a chosen OR is only reasonable for steel exhibiting an OR close to these ideal OR. According to the phenomenological theory of martensite [46,54], real OR deviate from idealized OR models and therefore this approach is inaccurate.

Another problem of this described approach arises if many variants are missing in the experimental obtained pattern and a comparison is not feasible. In this case, the presence of retained austenite is necessary in order to determine the correct orientation of the pattern and identify the variants [48]. However, retained austenite is often missing in sufficient extension in order to resolve it with EBSD measurements. Therefore, the martensite variant identification of the present work uses a reconstruction of the prior austenite grain orientation. Prior austenite is reconstructed by the iterative determination of an OR between martensite and austenite from Nyyssönen et al. [46]. The algorithm is based on following equation:

$$T_{n+1,k} = C_j^{-1} C_i \overline{T}_n M_k \tag{1}$$

In Equation (1), $\overline{T}_n$ is the input OR for an iteration and results in the output OR $T_{n+1,k}$. As initial input OR, KS is used. M_k represents the misorientation angle between neighboring martensitic grains obtained by EBSD measurements. A martensitic grain boundary is defined in this context by a misorientation angle above 3° between two pixels. C_i and C_j represent the symmetry operators of the cubic crystal system and have to be found for every iteration step using the experimental EBSD data. The average $\overline{T}_{n+1}$ calculated for all intergranular misorientations M_k is used as input of the subsequent iteration step. Therefore, the calculated OR deviates with every iteration step from the ideal KS OR and gets closer to the real OR. A martensite variant identification with calculated OR leads generally to reliable results [46]. Fig. 11 illustrates the angular deviation between KS OR and calculated OR as function of the iteration number. The plateau indicates the end of the iteration and exhibits the angular deviation of the real OR from KS OR by indicating the angular deviation between closed packed planes (i.e. $\{111\}_\gamma$ and $\{011\}_{\alpha'}$) and closed packed directions (i.e. $\langle 110\rangle_\gamma$ and $\langle 111\rangle_{\alpha'}$). These angular deviations are zero for ideal KS OR, as it is described in chapter 2.1.1.1.

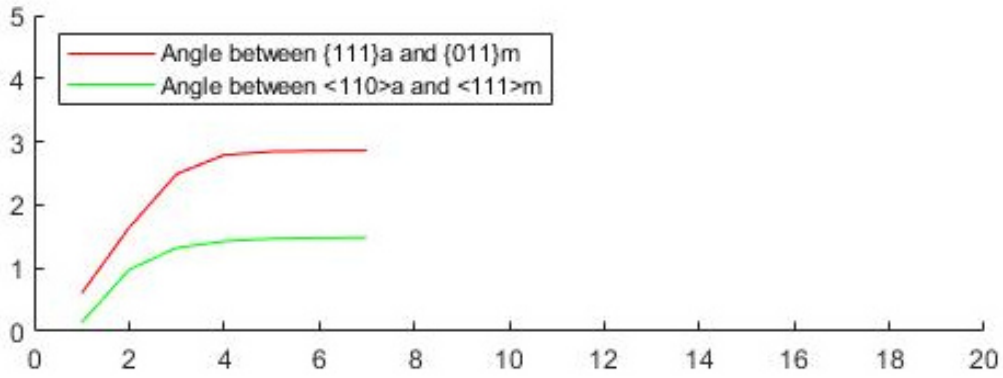

Fig. 11: Angular deviation of the calculated OR from KS OR for closed packed planes (i.e. $\{111\}_\gamma$ *and* $\{011\}_{\alpha'}$*) and directions (i.e.* $\langle 110\rangle_\gamma$ *and* $\langle 111\rangle_{\alpha'}$*) as function of the iteration number. The plateau indentifies the end of the iteration process and exhibits the real OR. This graph is calculated by the open source MatLab code of Nyyssönen et al.* [46].

A visualization of the variant identification by a comparison between experimental crystal orientation of martensite and a reference OR is given in Fig. 12 in a (001) pole figure. Here, a KS OR is chosen as reference pattern. Experimentally determined crystal orientations of martensite (grey points) are assigned to martensite variants of the reference OR (numbered blue circles) with the lowest angular deviation.

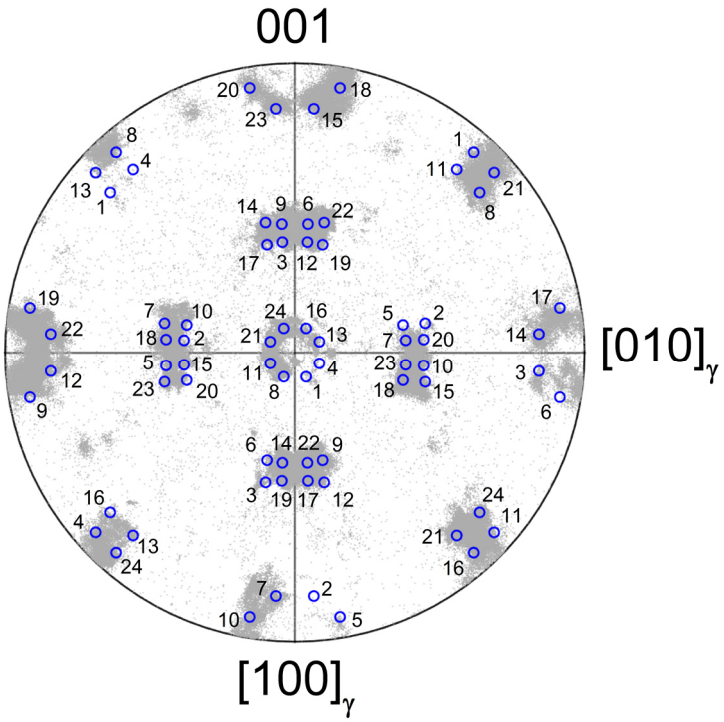

Fig. 12: Comparison of an exemplary experimental pattern of (001) reflexes of martensite (grey points) inside one prior austenite grain and an ideal KS-OR (blue circles) in order to illustrate martensite variant identification. Martensite reflexes with the lowest angular deviation to a specific martensite variant are identified.

The identification of martensite variants with inverse pole figure (IPF) color coding is not appropriate due to the symmetry of the IPF. This is illustrated in Fig. 13 with the 24 equal regions for IPF inside a (001) pole figure. A comparison with the pattern of KS OR (Fig. 12) exhibiting the same IPF color coding for different martensite variants (e.g. 7 and 23, 3 and 12, 2 and 15 or 14 and 22 and so on) is therefore not suitable for martensite variant identification.

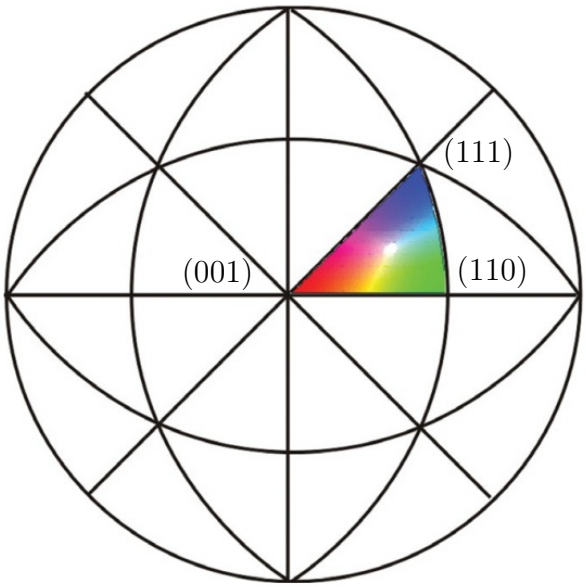

Fig. 13: The 24 equivalent regions for the color coding with inverse pole figure (IPF) in a (001) pole figure. A comparison with the characteristic pattern of the KS OR in Fig. 1 exhibits the same IPF color coding for different martensite variants. For example, the projection points of the variants 1, 4, 8, 11, 13, 16, 21 and 24 in the center of the (001) pole figure exhibit exactly the same red color coding according to IPF. Therefore, a variant identification due to IPF color coding is not possible. This figure is an adaption of [69].

2.1.4.2 Limits of martensite variant identification

Although, the identification of martensite variants is well described in literature, crystallographic relations between different prior austenite grains and imperfections of the prior austenite grain impede an absolute accurate identification.

Germain et al. [48], calculated the probability that two neighboring austenite grains with random crystal orientation forming similar martensite crystal orientation with misorientation tolerance up to 5°. In Fig. 14 this probability is given as “occurrence of specific boundaries” and drawn over the misorientation tolerance angle between the two closest martensite crystal orientations that evolve from the austenite grains with KS and NW OR.

The probability for two similar martensite crystal orientations with 5° misorientation evolving out of two neighboring austenite grains with KS OR is thus 26.5 %. The occurrence of these two martensite crystal orientations in the same austenite grain boundary area may therefore cause a misidentification because of the different martensite variant numbers according to the different austenite crystal orientations. It is assumed that the real percentage of misidentification is significantly lower than the mentioned 26.5 % because independently forming martensite crystals out of two prior austenite grains have to occur in the same grain boundary area.

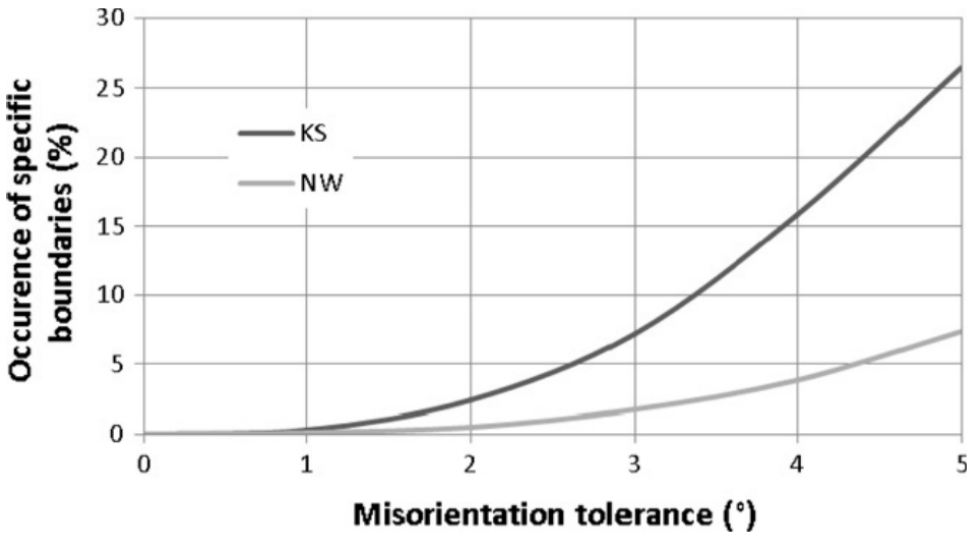

Fig. 14: Probability of two neighboring austenite grains with random crystal orientation forming martensite variants with misorientation tolerance up to 5° to each other. This calculation illustrates the high propability for KS OR to find a similar martensite variant in neighboring austenite grains.

In addition, a twin relationship of prior austenite grains may cause a misidentification of evolving martensite variants. Fig. 15 illustrates the pattern of martensite reflexes with KS OR out of two prior austenite grains with twin relation in a (001) pole figure. Six martensite variants out of 24, i.e. 25 %, exhibiting exactly the same crystal orientation according to KS OR [48]. Therefore, the assignment of these martensite variants to one prior austenite twin is unfeasible because of the same crystallographic orientation. However, again for a misidentification of the martensitic variant the both evolving martensite crystals have to occur at the same grain boundary area and therefore the real percentage of misidentification is significantly lower than 25 %.

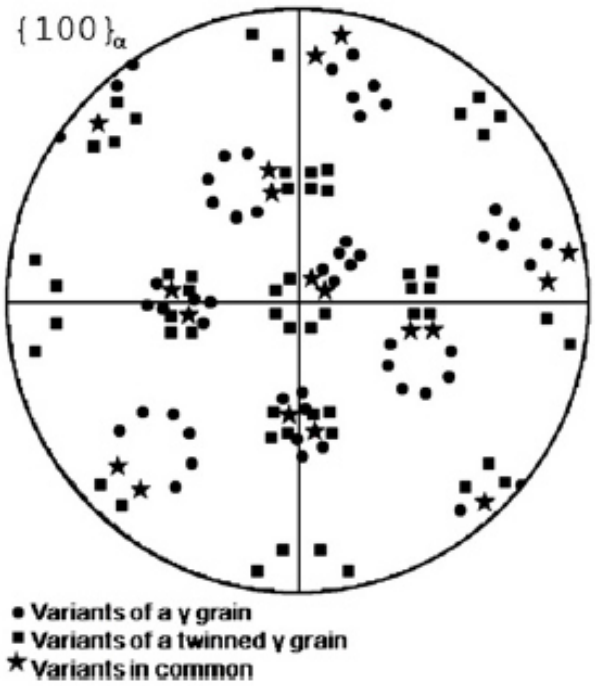

Fig. 15: Equal martensitic variants exhibiting KS OR evolving out of two prior austenite grains with a twin relationship [48]*. 6 variants out of 24 exhibiting the same crystal orientation and may therefore lead to misidentifications.*

Beneath those influences on the identification of martensite variants concerning the crystal orientation of idealized austenite grains with homogenous crystal orientation and KS OR, also imperfections of austenite grains can cause misidentification. According to Bhadeshia et al. [34,66], misorientation inside one prior austenite grain inherit the spread of orientation to the martensitic phase because of the strict OR between austenite and martensite, which is already described in chapter 2.1.3. This orientation spread can reach a magnitude of approximately 10°. Comparing Fig. 12, this spread can cause an overlapping of neighboring reflexes in (001) pole figure and therefore impedes an accurate identification. In addition, the misorientation inside one prior austenite grain changes with progressing martensite formation because of the transformation induced strains. Thus, the orientation spread inside pole figures increases with progressing martensite transformation and additionally complicates the martensite variant identification.

2.2 Austenitization phenomena

Besides the formation of the martensitic phase of PH 15-5 but also of other steels, austenitization is another crucial process influencing the final component properties, especially regarding microstructural evolution. During austenitization of soft martensitic steel but also low alloyed steel, phenomena such as austenite memory effect and subsequent recrystallization-like processes (i.e. spontaneous recrystallization) shaping the austenite microstructure concerning dislocation density, twin boundaries and grain size and therefore differ from classical austenitization. In the following, a literature summary of such phenomena is given.

2.2.1 Austenite memory effect

Austenite memory effect describes the inheritance of crystal orientation, grain size and grain shape from prior austenite to reversed austenite out of a martensitic matrix. The phenomenon was first observed in the 1960s [26,70,71] where austenitization cycles are applied on soft martensitic steels in order to obtain fine grained austenite and improve the mechanical properties. Nowadays the austenite memory effect is also known for low alloyed steel [49,72]. The prevention of grain refinement during austenitization caused by the austenite memory effect motivated to investigate this phenomenon.

The progress in understanding of the austenite memory effect is linked to the progress of investigation methods resolving the crystal orientation of fresh formed austenite and surrounding martensite such as transmission electron microscopy (TEM) or enable *in-situ* observations of austenite formation such as high temperature confocal laser scanning microscopy (HT-CLSM). Recent developments of *in-situ* observation techniques such as high temperature electron backscatter diffraction (EBSD), which are also applied in this work, open a new path for observation and understanding of austenite memory effect [49–51,72,73].

For the austenite memory effect four different formation mechanisms are postulated in literature: (I) cementite and martensite lath controlled reversed austenite formation [74,75], (II) retained austenite controlled reversed austenite formation [76,77], (III) reversed austenite formation by diffusionless shear [50], and (IV) internal martensite stress and martensite lath controlled reversed austenite formation [70].

Mechanism (I): Cementite and martensite lath controlled reversed austenite formation.

Watanabe et al. [74] postulated that austenite nucleates at martensite lath boundaries adjacent to cementite. For nucleation at the martensite/cementite interface, austenite exhibit a near KS OR to the martensitic matrix and a Pitch OR to cementite. For the nucleation and growth of reverted austenite on martensite laths 2 crystal orientations of austenite are favored because of crystallographic limitations [70]. The additional Pitch OR of austenite to cementite reduces the favored crystal orientations of austenite to one, i.e. the orientation of prior austenite, and therefore causes the austenite memory effect. Zhang et al. [75] added to this mechanism that only one variant of cementite (i.e. crystal orientation) has to be present inside one prior austenite grain in order to ensure the formation of reversed austenite with only one crystal orientation, i.e. the crystal orientation of prior austenite. Therefore, only cementite which exhibits an Isaichev OR [61] to the martensitic matrix should show the above mentioned variant restriction and cause the austenite memory effect. A schematic illustration of this assumption is illustrated in Fig. 16.

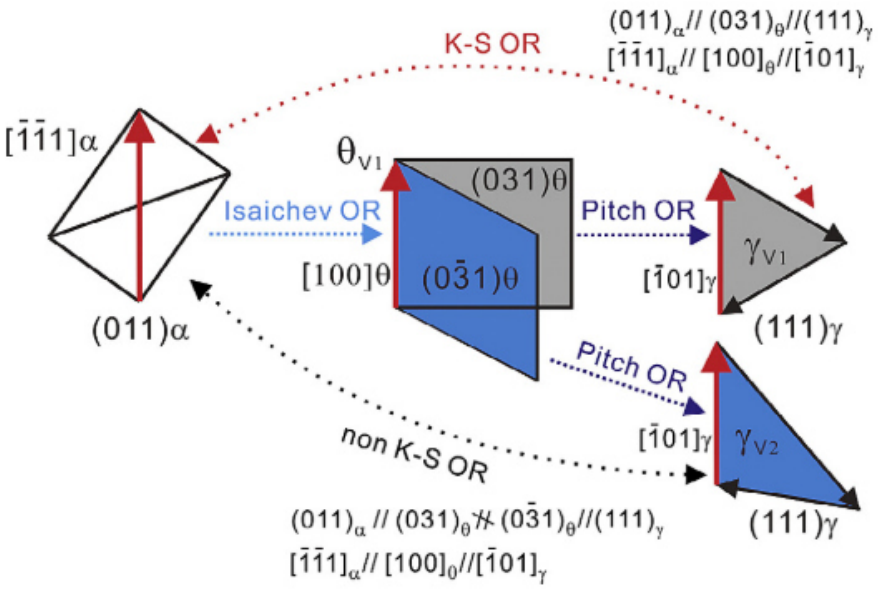

Fig. 16: Schematic illustration of the resulting KS OR between austenite and martensite as interaction of Isaichev OR between martensite and cementite as well as a Pitch OR between cementite and austenite by Zhang et al. [75].

Mechanism (II): Retained austenite controlled reversed austenite formation

Kimmins et al. [77] postulated the diffusional growth of retained austenite films located at martensite lath boundaries. Furthermore, impingement and coalescence of neighboring retained austenite films restore grain size and shape of prior austenite. According to Liu et al. [76] mechanism (II) is preferred among the existing four if inter-lath retained austenite is present because no nucleation of reversed austenite is needed.

Mechanism (III): Reversed austenite formation by diffusionless shear

Mechanism (III) describes a diffusionless shear transformation from martensite to austenite reverse to the austenite to martensite transformation and therefore causes the same crystal orientation as prior austenite. Diffusionless transformations from martensite to austenite is promoted by high heating rates, low carbon content and a high Ni/Cr ratio (i.e. low A_1 and A_3 temperatures) [22,25,78,79]. Investigations of Shirazi and Nakada et al. [50,80] on binary iron-nickel alloys suggested the austenite memory effect caused by diffusionless shear-transformation for Ni contents above 18 m.% and heating rates of 20 and 30 °C/s, respectively. Owing to the higher Cr content of soft martensitic steels compared to binary Fe-Ni alloys, A_1 and A_3 temperatures are raised and diffusional martensite to austenite transformation gets favorable and therefore makes a shear transformation more improbable [1].

Mechanism (IV): Internal martensite stress and martensite lath controlled reversed austenite formation

Nakada et al. [70] postulated a diffusion controlled mechanism for the austenite memory effect without the presence of carbides or retained austenite in a 13Cr-6Ni soft martensitic steel. It is claimed that austenite nucleates at martensite lath-boundaries with a near KS OR, i.e. closed packed planes and directions of austenite and surrounding martensite are nearly parallel. Such OR is favorable because of the lowest nucleation energy for $\{111\}_\gamma||\{011\}_{\alpha'}$ and the lowest interface energy for $\langle 011\rangle_\gamma||\langle 111\rangle_{\alpha'}$ growth direction. These crystallographic limitations enable the formation of five crystal orientations for reversed austenite inside one prior austenite grain. In order to observe the austenite memory effect one of these five possible orientations of austenite has to be dominant. According to Nakada et al. [70]

internal stress fields in the martensitic matrix, induced by the transformation from prior austenite to martensite, promote the formation of reversed austenite with equal crystal orientation to prior austenite. The postulation is validated by a comparison of reversed austenite crystal orientation formed after intercritical annealing at 640 °C (Fig. 17a - d) and formed after the same heat treatment but simultaneously uniaxial loading of 100 MPa (Fig. 17e, f). The comparison indicates that reversed austenite inside one prior austenite grain forms more different crystal orientations by applying an external load and therefore impedes the austenite memory effect based on mechanism (IV).

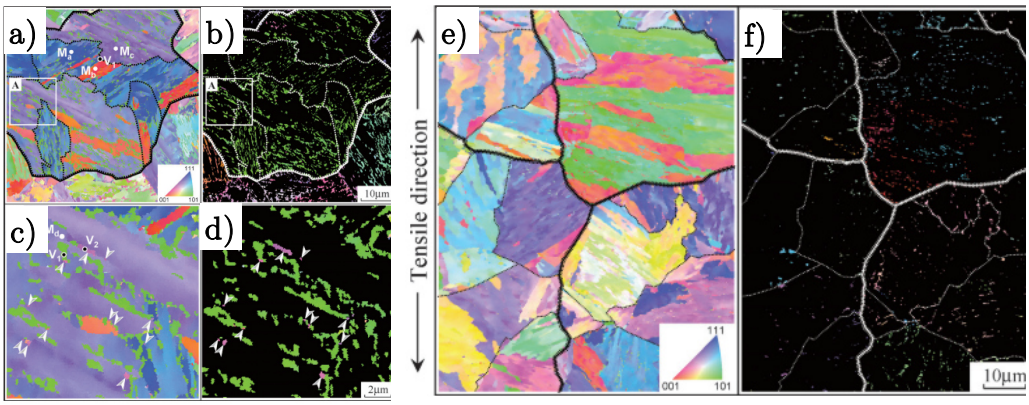

Fig. 17: IPF of the martensitic phase (a) and reversed austenite (b) after intercritical annealing at 640 °C for 1800 s in a 13Cr-6Ni steel without external load with magnification of the highlighted areas in a and b (c,d). IPF of the martensitic phase (e) and reversed austenite (f) after intercritical annealing at 640 °C for 900 s with simultaneously uniaxial tensile stress of 100 MPa. Comparing (b) and (d) with (f), more different reversed austenite crystal orientations are obtained inside one prior austenite grain. This observation indicates that the applied external load impedes the austenite memory effect for this alloy (f) (adaption of [70]*).*

Mechanism (IV) is also reported by Shinozaki et al. [49,72] for low alloy steel with a low heating rate of 0.05 °C/s. Fig. 18 shows the *in-situ* evidence of the austenite memory effect by high temperature *in-situ* EBSD. According to Shinozaki et al. [49], mechanism (IV) is present because too less cementite and no retained austenite is present in the alloy and additionally the heating rate is too low for reverted austenite formation by diffusionless shear.

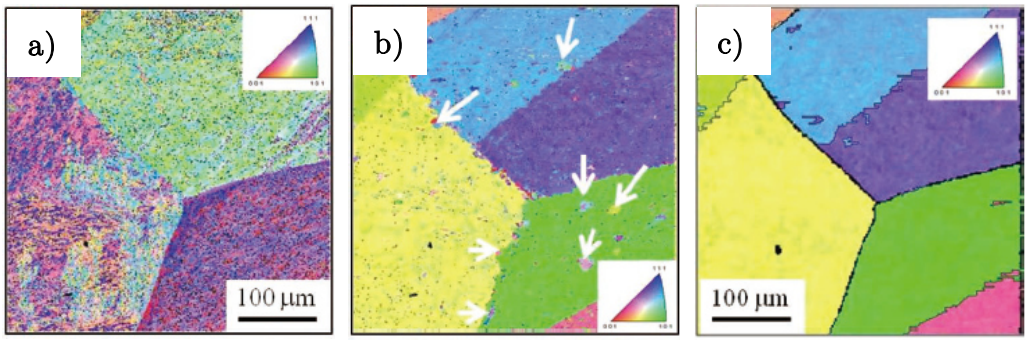

Fig. 18: Evidence of the austenite memory effect by Shinozaki et al. [49] *formed by mechanism (IV) in a low alloyed steel with IPF of initial martensitic microstructure at 700 °C (a), reversed austenite at 850 °C (b) and a reconstruction of prior austenite based on the martensitic microstructure (c) (adaption of* [49]*).*

2.2.2 Spontaneous recrystallization

In this work, the term spontaneous recrystallization describes the reduction of austenite grain size after complete austenitization in combination with a re-formation of austenite crystal orientation such as it is observed for classical recrystallization but without previous deformation. Therefore, the driving force (i.e. enhanced dislocation density) for the rearrangement of crystal orientation has to be produced by some internal mechanism. This mechanism may be related to austenite memory effect because spontaneous recrystallization is only observed subsequent to this phenomenon [49,50,72,76,81].

Shirazi et al. [50] observed spontaneous recrystallization in a binary Fe-Ni alloys (18 to 23 m.% Ni) after complete austenitization exhibiting the austenite memory effect. The formation mechanism of reversed austenite was identified as mechanism (III) according to the austenite memory effect (i.e. reversed austenite formation by diffusionless shear). Therefore, Shirazi et al. [50] assumed that the enhanced dislocation density, induced by mechanism (III), provides the driving force for spontaneous recrystallization.

Fig. 19a illustrates the martensitic microstructure (IPF color coding) at room temperature after austenitization at 700 °C for 3 min with a heating rate of 20 °C/s. Fig. 19b provides the corresponding image quality (IQ) information. The prior austenite grain γ_1(M) exhibits a coarser martensite microstructure size, a higher IQ and a smaller orientation spread in the (001) pole figure in comparison to the prior austenite grains γ_2(M), γ_3(M) and γ_4(M). Therefore, a decrease of dislocation density of the prior austenite grain γ_1(M) due to spontaneous recrystallization is postulated by Shirazi et al. [50] (cf. chapter 2.1.3). However, Fig. 19 shows a very early stage of

spontaneous recrystallization and therefore no prior austenite grain refinement is quantified. Additionally, no high temperature *in-situ* examination of the austenitic phase was conducted. However, austenite grain refinement for a later stage can be assumed because also other recrystallized austenite grains are visible in Fig. 19a and highlighted with yellow, black and green dashed lines located adjacent to prior austenite grain boundaries.

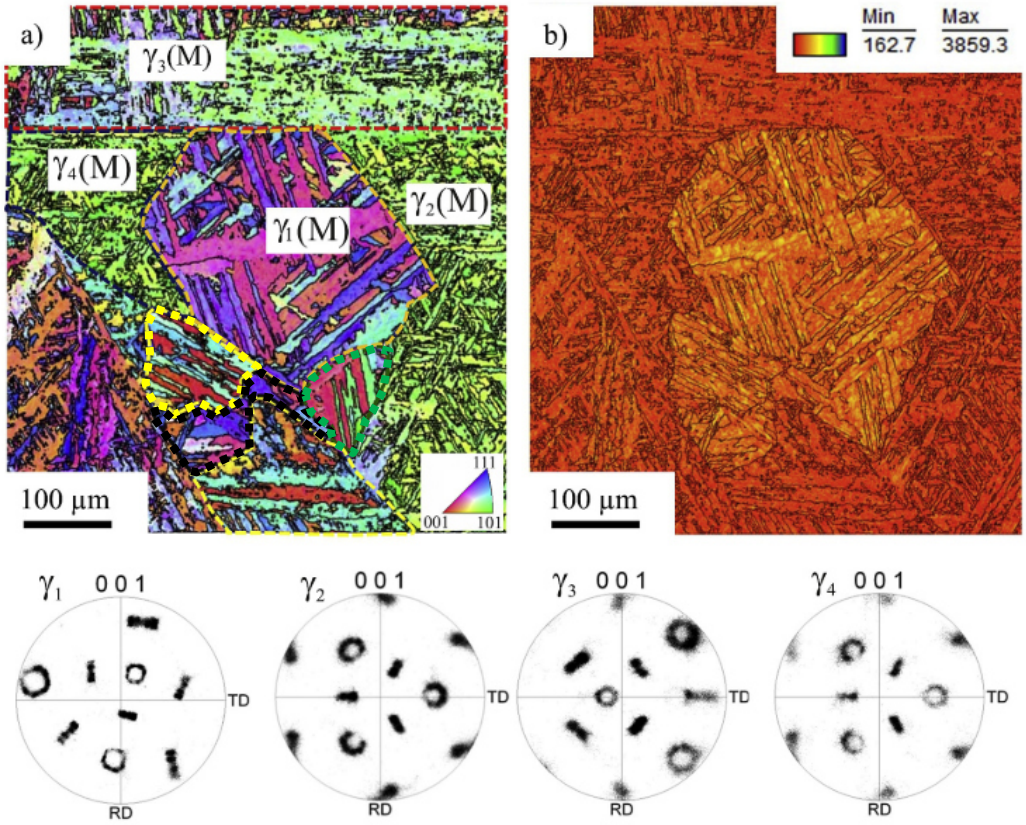

Fig. 19: EBSD measurement of the martensitic microstructure of a binary Fe-23 Ni alloy at room tempearture in IPF (a) and IQ (b) color coding. The prior austenite grain $\gamma_1(M)$ exhibits a higher IQ, a coarser martensite substructure size and a lower spread of the reflexes in the (001) pole figure in comparison to the other prior austenite grains $\gamma_2(M)$, $\gamma_3(M)$ and $\gamma_4(M)$. Therefore, spontaneous recrystallization of the $\gamma_1(M)$ grain is evidenced. Additionally, other recrystallized prior austenite grains are highlighted with yellow, black and green dashed lines [50].

Spontaneous recrystallization is also observed in steels with lower Ni content subsequent to austenite re-formation according to the austenite memory effect formed by a diffusion controlled mechanism [49,72,76,81]. Liu et al. [76,81] evidences spontaneous recrystallization *in-situ* after complete austenitization exhibiting the austenite memory effect in a 13Cr-5Ni steel with HT-CLSM at an austenitization temperature of 930 °C with a heating rate of 10 °C/min. Fig. 20 illustrates the process of austenite grain refinement in a

temperature range between 860 °C (Fig. 20a) and 930 °C (Fig. 20d). According to Liu et al. [76,81], a competition between different types of austenite, called acicular and globular austenite, causes the spontaneous recrystallization phenomenon. Acicular austenite nucleates on martensite lath boundaries exhibiting a KS OR to the martensitic matrix and a coherent interface resulting in the same crystal orientation as prior austenite. Globular austenite nucleates at prior austenite grain boundaries and exhibits no OR to the martensitic matrix and an incoherent interface resulting in a random crystal orientation.

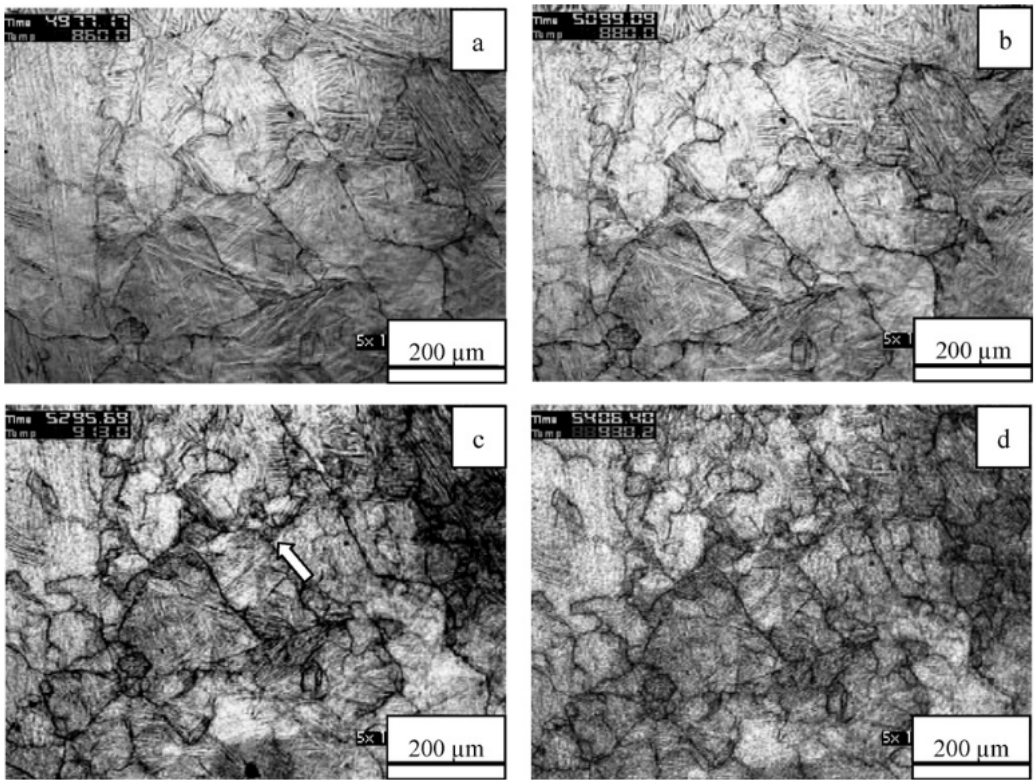

Fig. 20: In-situ evidence of spontaneous recrystallization of austenite after complete austenite formation in a 13Cr-5Ni steel by Liu et al [81]. *Part (a) and (b) illustrates the austenitic microstructure at 860 °C (a) and 880 °C (b) exhibiting the same grain size as prior austenite (i.e. austenite memory effect according to Liu et al.* [81]*). At 913 °C (c) spontaneous recrystallization starts and proceeds until the austenitization temperature of 930 °C (d).*

High temperature *in-situ* EBSD measurements of Shinozaki et al. [49,72] in low alloyed steel (0.36C-0.22Si-0.79Mn-0.007P-0.003S-3.04Cr-1.46Ni-0.43Mo-0.1V-0.03Al) affirming the postulations of Liu et al [76,81] concerning the simultaneous formation of globular and acicular austenite. Fig. 21a illustrates the austenite microstructure in IPF color coding at a temperature of 850 °C exhibiting the austenite memory effect (cf. Fig. 18). Additionally, Fig. 21c gives the corresponding kernel average misorientation (KAM). White arrows are highlighting globular austenite predominantly at prior

austenite grain boundaries and exhibiting a lower KAM corresponding to a lower density of geometrically necessary dislocations (GND) [82,83]. According to Shinozaki et al. [49], the surrounding austenite exhibits a higher KAM and therefore it is assumed that acicular austenite is coalesced. For further heating up to 900 °C, austenite regions with lower KAM and new crystal orientations form, evidencing the presence of spontaneous recrystallization. According to Shinozaki et al. [49], the formation of spontaneous recrystallization is attributed to the growth of globular austenite driven by the consumption of dislocations density of coalesced acicular austenite. However, some of the globular austenite regions are still present in the already fully recrystallized state indicating that not all of the observed globular austenite regions contribute to spontaneous recrystallization. Although, Shinozaki et al. [49] distinguishes between globular austenite and spontaneous recrystallization it is not clear if globular austenite was present before spontaneous recrystallization or globular austenite is the first stage of spontaneous recrystallization.

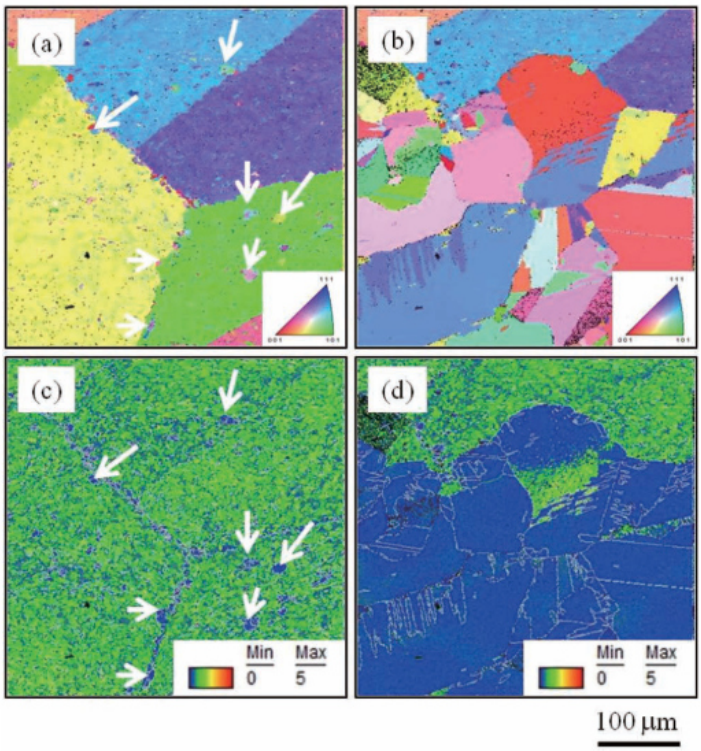

Fig. 21: Spontaneous recrystallization after austenite memory effect (cf. Fig. 18) in a low alloyed steel by Shinozaki et al. [49]. *IPF color coding exhibits the austenite grain refinement between 850 °C (a) and 900 °C (b). Additionally, the KAM color coding illustrates the corresponding decrease of misorientation of the fresh formed austenite grains from austenite exhibiting the austenite memory effect at 850 °C (c) to austenite after spontaneous recrytsallization at 900 °C (d) indiacted by the blue areas.*

Zhang et al. [75,84] investigated the formation of globular and acicular austenite in a Fe-2Mn-1.5Si-0.3C alloy during inter-critical annealing. He assigned the formation of acicular austenite to a nucleation on martensite lath boundaries and partitional growth. Austenite stabilizing elements such as Mn and Ni are therefore enriched in austenite during the early stages of acicular austenite formation and ferrite stabilizing elements such as Si and Cr are depleted in austenite. However, the formation of globular austenite is assigned to a nucleation on prior austenite grain boundaries and cementite and subsequent partitionless growth. According to the findings of Zhang et al. [84], acicular austenite is formed predominantly at lower temperatures (~720 °C) and globular austenite at higher temperatures (~820 °C). Although, the absolute transformation temperatures depend on the observed alloying system, this conclusion is consistent with observations of Liu and Shinozaki et al. [49,72,76,81] and indicate the growth of globular austenite as possible reason for spontaneous recrystallization.

3 Experimental

3.1 Material states

The investigated steel alloy PH15-5 was produced by voestalpine Böhler Edelstahl GmbH & Co KG with the chemical composition given in Table 2. After casting the ingot was remelted in vacuum and subsequently hot forged.

Table 2: Chemical composition of PH 15-5 in m.%.

C	Si	Mn	Cr	Ni	Cu	Nb	N
0.032	0.29	0.54	15.01	5.10	3.21	0.27	0.013

In this work two different as-received material states are investigated, an experimental as-received material state in order to set the exact deformation parameters due to the smaller sample size, and an industrial as-received material state in order to investigate the microstructure of industrial forgings.

Industrial as-received (IAR) material state

The industrial forging was carried out by voestalpine Böhler Aerospace GmbH & Co KG and consists of three deformation steps at a deformation temperature of 1100 °C. The degree of deformation of the very last forging step was between 30 % and 40 %. This material state was used in order to analyze the continuous austenitization behavior during solution annealing and the subsequent martensitic transformation during cooling to room temperature (chapter 4.2 and 4.3). In the following, this material state is referred to as IAR material state.

Experimental as-received (EAR) material state

In order to get a more defined material state compared to the industrial as-received material state, an experimental material state was produced with more precise process parameters. The experimental as-received material state was generated by one single forging step on a Gleeble 3800 system at a temperature of 1150 °C with a deformation of 30 % and a deformation rate of 0.1 s^{-1}. This material state was used in order to analyze the martensitic microstructure of the initial state (chapter 4.1) and for comparison to

the microstructure of the IAR material state. In the following, this material state is referred to as EAR material state.

Additionally, two further material states were generated in order to investigate the influence of the austenitization parameters on martensitic microstructure in chapter 4.3 of the work.

After solution annealing (AS) material state

This material state was generated by the solution annealing in the course of the high temperature *in-situ* EBSD measurements of the IAR material state. The temperature-time profile of this solution annealing procedure is illustrated in Fig. 29. For solution annealing the material was heated-up with a heating rate of approximately 3.3 °C/s followed by isothermal annealing at a temperature of 1030 °C for 10 min. In the following, this material state is referred to as AS material state.

Coarse grain (CG) material state

This material state was generated by an additional coarse grain annealing at 1150 °C for 40 min of the industrial solution annealed (1030 °C, 30 min) and tempered (560 °C, 4 h) material state of PH 15-5. The heating rate until the annealing temperature and tempering temperature were reached was approx. 3.3 °C/s. Subsequently, to the coarse grain annealing the conventional industrially used solution annealing and tempering is repeated in order to investigate the influence of the initial austenite grain size on spontaneous recrystallization. In the following, this material state is referred to as CG material state. The temperature-time profile of the CG material state is shown in Fig. 22.

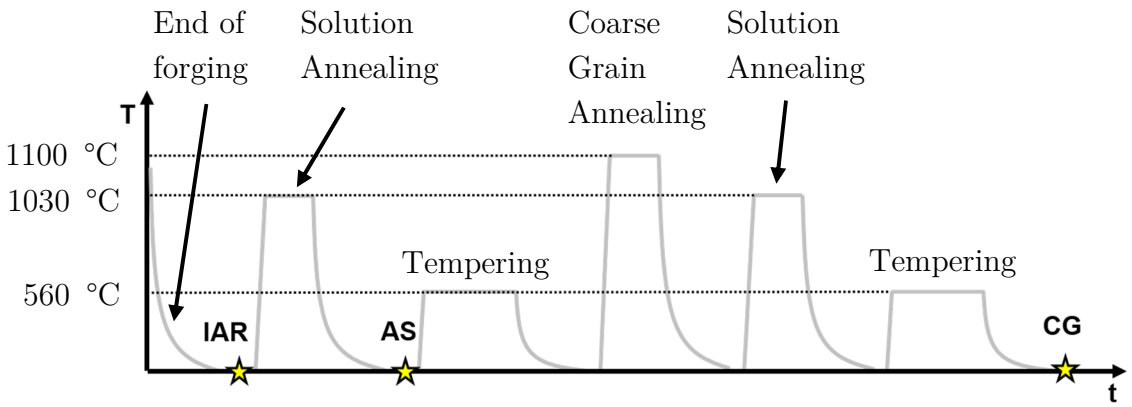

Fig. 22: Schematic illustration of the heat treatment condition of the analyzed material states industrial as-received (IAR), after solution annealing (AS) and coarse grain (CG).

3.2 Investigation methods

The following chapters deal with the investigation methods used in the present work and describe the basic principles and experimental parameters used in the various methods.

3.2.1 Electron Backscatter Diffraction

Electron backscatter diffraction (EBSD) is a useful investigation method in order to analyze crystal orientations over a wide area [32]. Especially for the characterization of martensite, EBSD enables the investigation of its hierarchical substructure with strict crystallographic OR over a measurement field containing many prior austenite grains in order to obtain good statistics [32,48]. In the following chapters, the generation of EBSD data and their representation methods are described in detail.

3.2.1.1 Generation of EBSD data

EBSD enables a point by point determination of the local crystal orientation of crystalline solids in a scanning electron microscope with a maximum lateral resolution of about 20 nm [32]. The crystal orientation is automatically determined by comapring the orientation of a Kikuchi-pattern with a reference coordinate system. In the following, the formation of Kikuchi-pattern and the subsequent calculation of the crystal orientation is briefly described.

Kikuchi-pattern originate by diffraction of electrons on lattice planes fulfilling Bragg's law. Bragg's law (Equation (2)) describes diffraction of an incident beam with wavelength λ and with an angle θ relative to the considered lattice planes with the spacing d. An illustration of the diffraction is given in Fig. 23. Constructive interference is present for diffraction of the incident beam with the Bragg angle $\theta = \theta_B$.

$$n * \lambda = 2 * d * \sin(\theta) \tag{2}$$

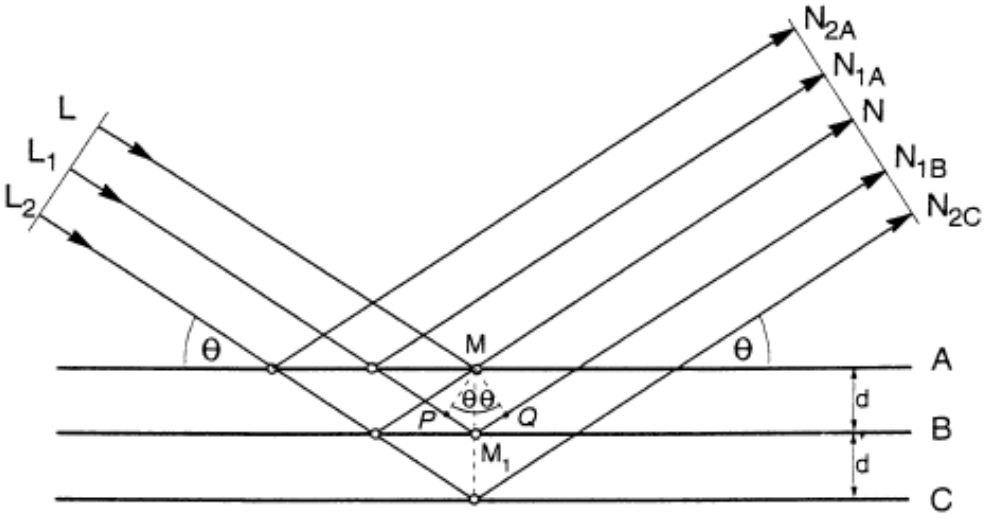

Fig. 23: Diffraction on a crystal lattice as for the derivation of Bragg's law; Equation (2). Constructive interference occurs for $\theta = \theta_B$ [32].

When the incident electron beam enters the tilted sample, it is inelastically scattered in all directions, i.e. the energy of the electrones reduces [32]. This is schematically illustrated in Fig. 24.

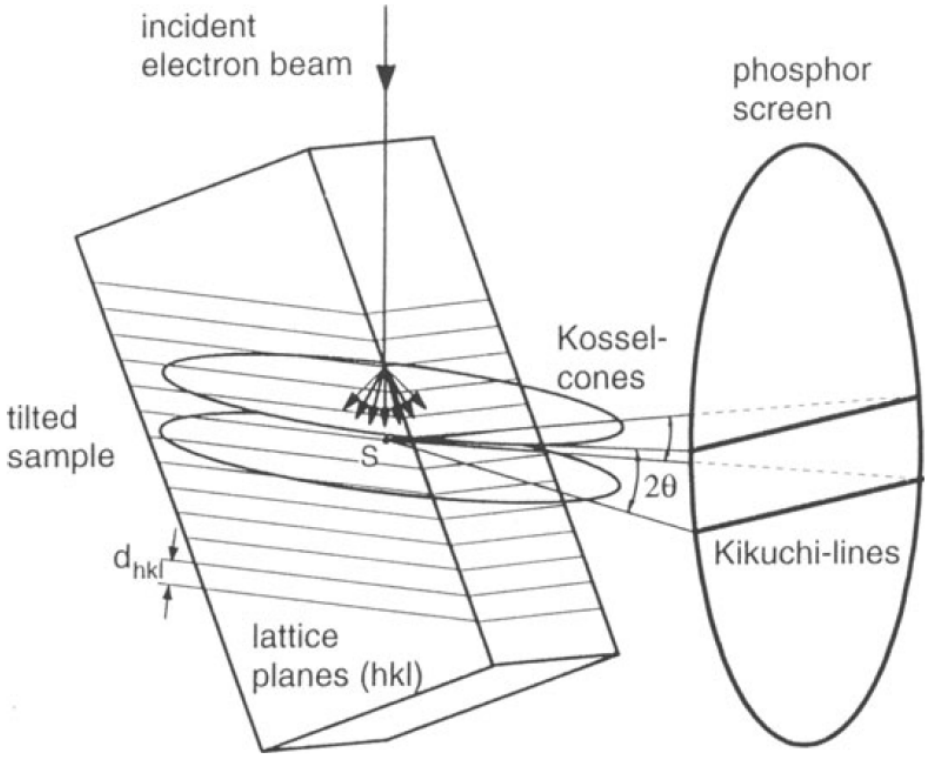

Fig. 24: Formation of Kikuchi lines due to diffraction of the incident electron beam on lattice planes by fulfilling Bragg's law (i.e. Kossel-cones). Kikuchi-lines are generated by the intersection of the Kossel-cones with the phosphor screen (i.e. the detector). Kikuchi-lines of different hkl lattice planes form the Kikuchi-pattern [32]. *The orientation of the Kikuchi-pattern with respect to a reference coordinate system determines the crystal orienration of one pixel in the EBSD measurement.*

For the explanation, an inelastic scattering event is assumed located between two lattice planes, illustrated in Fig. 24 at point S. From this point, electrons are inelastically scattered in all directions. Therefore, braggs law is fulfilled at every set of lattice planes and the scatterd electrons are diffracted also for the illustrated hkl plane. The Bragg angle in EBSD applications is very small (approximately 0.5°), thus, the diffracted beam is nearly parallel to lattice planes [32]. Furthermore, diffraction occurs in all directions appearing as so-called Kossel-cones in Fig. 24. The assumption of the inelastic scattering event between two planes lead to the formation of two parallel Kossel-cones originatig from electrons diffracted above and below the scattering event. The intersections of these Kossel-cones with the electron sensitive phosphor screen creates the Kikuchi-lines. Two parallel Kikuchi-lines form a Kikuchi-band. As metioned above, braggs law is fulfilled for every set of lattice planes and therefore a whole pattern of Kikuchi-bands appear on the phosphor screen of a real EBSD experiment. This specific arrangement of Kikuchi-bands is called Kikuchi-pattern. However, this is a simplification of the real process because inelastic scattering occurs not in one point such as Point S in Fig. 24 but in an excitation volume. Kikuchi-lines are not sharp in real EBSD measurements and consisting of brighter and darker lines [85]. However, such detailed analysis is used for elastic-strain mappings in high resolution EBSD [85–87] but is not further discussed in the present work.

The Kikuchi-pattern gives information about the crystal orientation of the position where the incident beam hits the sample. In order to automatically identify this orientation, a transformation of the pattern into the Hough-space is carried out by applying Equation (3).

$$\rho' = x * \cos(\theta') + y * \sin(\theta') \tag{3}$$

The transformation is schematically illustrated in Fig. 25 representing three points on one Kikuchi-band (Fig. 25a). Each point (1 - 3) in Fig. 25a is transformed to a graph in Fig. 25b (1 - 3) All points, which are lying on one Kikuchi-band in real space (x, y) in Fig. 25a exhibit a common intersection in Hough space (θ', ρ') in Fig. 25b. The intersections appear as bright points in Hough space and are easily detectable for the software [88].

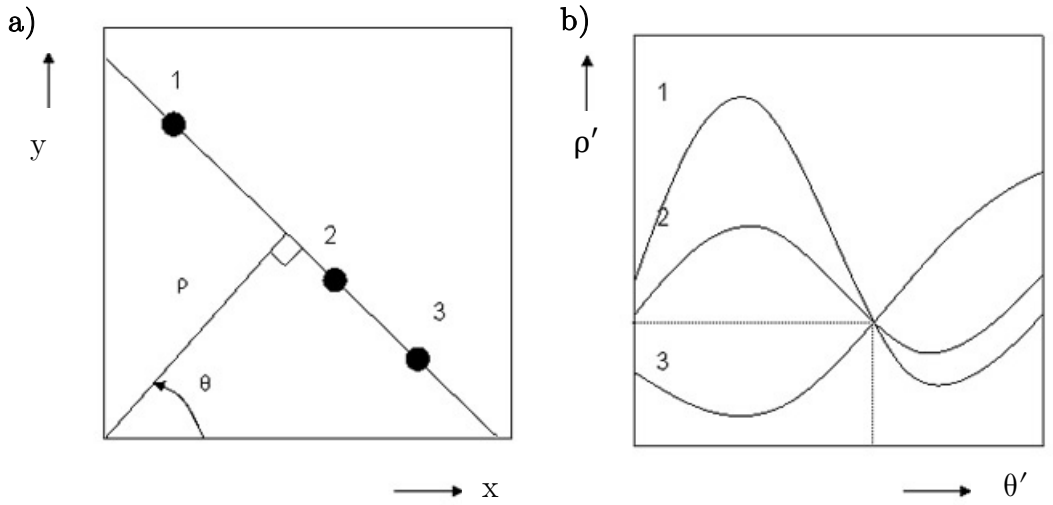

Fig. 25: Hough transformation from lines in real space (a) to points in the Hough space (b). Points 1, 2 and 3 in real space (a) are lying on a straight line and therefore exhibit a common intersection in Hough space (b). This procedure improves the performance of the detection of Kikuchi-bands by the EBSD software (adaption of [88]*).*

Finally, the detected Kikuchi-bands are transformed back in real space (x, y) and are indexed by comparing the angles between Kikuchi-bands with a data-base of inter-planar angles for a specific crystal system, i.e. a specific phase [89]. In order to specify crystallographic orientations, a reference coordinate system is defined, which enables the record of the crystal orientation with respect to the reference coordinate system by 3 angles, i.e. Euler-angles [32].

This routine is conducted for each position of the incident electron beam on the sample and therefore results in an array of data consisting of the x and y coordinates on the samples surface with the corresponding crystal orientation represented by Euler-angles.

3.2.1.2 Processing and representation of EBSD data

In the following, processing and representation methods of the generated EBSD data are presented, which are used in this work.

Inverse pole figure (IPF)

The IPF color coding is an approach to illustrate crystallographic orientations of the same plane family, which are parallel to the sample surface, with the same color. Fig. 13 illustrates the color coding of the different crystal orientations by an overlap of the IPF color coding triangle with a (001) pole figure. For example, {001} planes parallel to the sample surface are drawn in red, {011} planes parallel to the sample surface are drawn in green

and {111} planes are drawn in blue. Higher indexed planes, located between the mentioned planes, are represented with a mixture of red, green and blue according to the IPF color map in Fig. 13. Therefore, the IPF color coding is a useful approach for the fast identification of different crystal orientations, e.g. different prior austenite grains. However, the distinction of different martensite variants is not possible because of the symmetry of the IPF color map leading to the same color for different martensite variants. Therefore, a specific approach for martensite variant identification has to be conducted, which is presented in chapter 2.1.4 of this work.

Kernel average misorientation (KAM)

The KAM is a useful approach in order to visualize crystallographic misorientations inside a crystal. The KAM is used for the investigation of subgrain boundaries, plastic deformation textures and recrystallization phenomena in materials science [32,49,50,83]. For the determination of the KAM, the average misorientation of a pixel is calculated with respect to its neighbors. Therefore, the range of neighbors has to be defined, e.g. first neighbors, second neighbors, first and second neighbors and so on. Additionally, the angular limit has to be defined up to which angle the KAM is calculated. Pixel exhibiting larger angular deviations are summarized. The calculation of the KAM for the first neighbor is schematically illustrated in Fig. 26. Here, ω is the angular deviation between one hexagonal EBSD pixel and its neighbors. Hexagonal EBSD grids are usually used by EDAX software, which is also used in the present work.

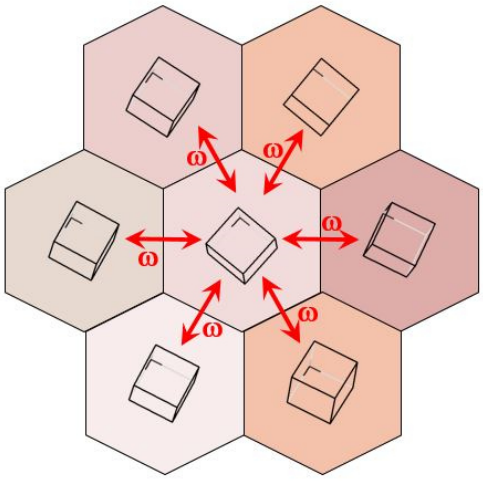

Fig. 26: Schematic illustration of the KAM determination for one hexagonal pixel by calculating the average angular misorientation ω to its first neighbors [90].

However, the KAM is a useful parameter in order to calculate the geometrically necessary dislocation density (ρ_{GND}) of a material. The relationship between KAM and ρ_{GND} is given by Equation (4) [82,83].

$$\rho_{GND} = \frac{2 * KAM}{EBSD_{Step\ Size} * b} \tag{4}$$

Beside the Burgers vector b, the ρ_{GND} is influenced by the step size of the EBSD measurement, i.e. the lateral spacing between two pixel. Fig. 27 illustrates, the higher the EBSD step size, the lower is the calculated ρ_{GND} (blue line) and verifies it with a theoretical prediction (red line) [91]. Therefore, it can be summarized that the ρ_{GND} calculated by KAM is only an approximation of the real ρ_{GND} of the material. Additionally, the dislocation density inside a material consists of GND and statistically stored dislocations and this second type of dislocations is not resolvable with KAM [91].

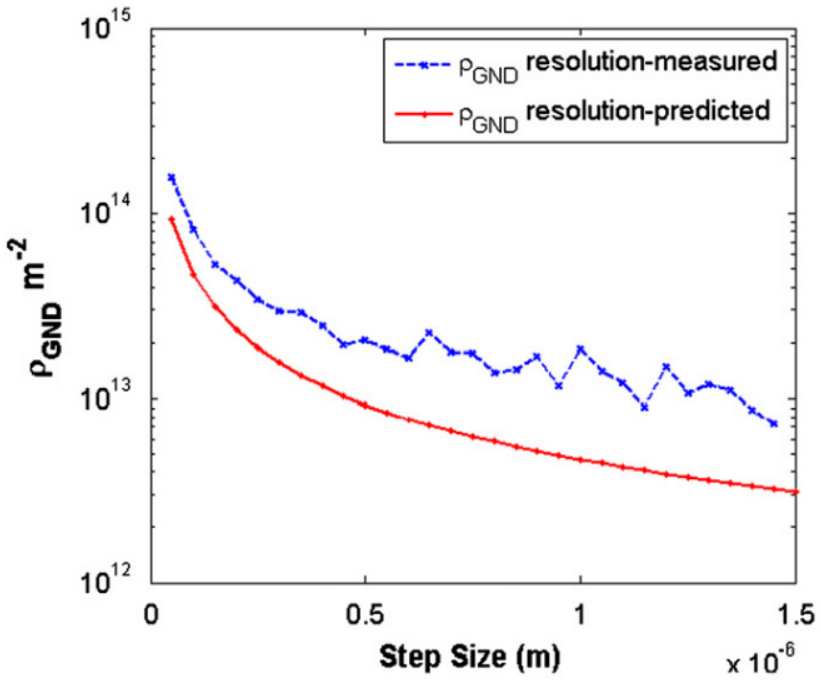

Fig. 27: Influence of the EBSD step size on the calculated (blue) and predicted (red) geometrically necessary dislocation density ρ_{GND} in silicon by Jiang et al. [91]. Both trends show an increase of ρ_{GND} with decreasing EBSD step size. The term "resolution" describes the minimum detectable ρ_{GND} for a given angular resolution ($5*10^{-5}$ rad) of the EBSD detector and a given EBSD step size. Therefore, the quantitative determination of ρ_{GND} with KAM is inaccurate but a qualitative comparison of ρ_{GND} between two different material states with the same EBSD step size is practicable.

However, a qualitative comparison of the KAM between different material states measured with the same EBSD step size is practicable in order to investigate qualitative differences in ρ_{GND} [49,91].

Confidence Index (CI)

The CI classifies the reliability of the indexing of Kikuchi-bands and ranges from 0 (i.e. not reliable) to 1 (i.e. reliable). According to Equation (5) [92] the CI is defined as:

$$CI = \frac{V_1 - V_2}{V_{ideal}} \tag{5}$$

V_1 represents the number of votes for the most likely solution from the indexing algorithm, V_2 represents the number of votes for the second likely solution and V_{ideal} represents the total number of possible votes for all solutions. As an example, the investigation of fcc materials reveals that 6 identified Kikuchi-bands (correct or incorrect identified) inside one Kikuchi pattern lead to a solution, which was correct in 95 % of the cases with a CI greater than 0.1 [92]. Therefore, the CI is a useful parameter in order to exclude data points with bad reliability e.g. for KAM analysis.

Phase information

As mentioned above, the orientation of a crystal is determined by the comparison of angles between Kikuchi-bands of a specific phase. The expected phases have to be defined before the EBSD measurement in order to restrict the possible crystal systems and enhance the processing speed. The phase information gives the best fitting phase for a specific Kikuchi-pattern for each pixel. Therefore, it enables the fast differentiation between the different phases of an EBSD measurement.

Image quality (IQ)

There are different approaches for the definition of IQ [93]. In the present work, the IQ represents the intensity of the peaks in the Hough-space originating from the transformed Kikuchi bands of the real space. Hence, the IQ is a measure for the quality of the Kikuchi-pattern [93]. Sharp Kikuchi-pattern exhibit larger intensity peaks in Hough-space and thus a good (i.e. high) IQ. Therefore, the IQ is a useful representation method of EBSD data in order to illustrate microstructural features such as grain boundaries because of the bad quality of Kikuchi-pattern and therefore bad IQ of this

regions. However, the IQ is influenced by the sample preparation, vacuum during the EBSD measurement, quality of the electron beam, etc. and can therefore hardly be used to directly compare results from different measurements [93]. In general, the IQ is a not normalized number ranging between one and a few ten-thousand counts but exhibits no upper limit.

Martensite block size determination

A martensite block is defined in the present work by an area of pixels exhibiting a specific maximum angular deviation. This maximum angular deviation depends on the calculated OR and therefore on the investigated material state. The procedure used in this thesis for the determination of the block boundary angle is further described in chapter 4.1.2.1.

After the determination of the block boundary angle, the block size is calculated with the equivalent circle diameter of the enclosed area. In order to exclude noise of the EBSD measurement, a minimum area for a martensite block is defined. This area is chosen in this thesis to be 4 pixel for EBSD measurements with a step size of 300 nm and 9 pixel for step sizes of 200 nm. Therefore, the minimum detectable martensite block size is 0.677 µm for each conducted EBSD step size and therefore the determined martensite block sizes are comparable. A distribution of the determined martensite block sizes is calculated according to the counts of a specific block size (number fraction) and the area of a specific block size (area fraction) for each material state. Therefore, block sizes are summarized to 30 equal-sized groups (i.e. grid points in the distribution) ranging from the smallest to the largest detected block size for each material state.

For the determination of the mean martensite block size, two different approaches were conducted in this thesis:

- Mean martensite block size according to number fraction:
  The determination of the mean martensite block size according to number fraction ($\bar{d}_{num.fract.}$) is conducted according to Equation (6). Here, d_i represents the equivalent circle diameter of an individual martensite block and N is the total number of all detected martensite blocks.

$$\bar{d}_{num.fract.} = \frac{1}{N}\sum_{i=1}^{N} d_i \qquad (6)$$

However, $\bar{d}_{num.fract.}$ is sensitive to the minimum detectable martensite block size due to a strong weighting of many small martensite blocks. Therefore, only EBSD measurements with the same minimum detectable martensite block size are comparable.

- Mean martensite block size according to area fraction:
  The determination of the mean martensite block size according to area fraction $\bar{d}_{ar.fract.}$ is conducted according to Equation (7). Here, each martensite block is weighted by its area A_i. Again, d_i represents the equivalent circle diameter of an individual martensite block and N is the total number of all detected martensite blocks.

$$\bar{d}_{ar.fract.} = \frac{\sum_{i=1}^{N} A_i * d_i}{\sum_{i=1}^{N} A_i} \quad (7)$$

However, $\bar{d}_{ar.fract.}$ strongly weights a little number of large blocks and therefore material states with only a few very coarse martensite blocks exhibiting a high $\bar{d}_{ar.fract.}$. Additionally, $\bar{d}_{ar.fract.}$ is less sensitive to the minimum detectable block size compared to $\bar{d}_{num.fract.}$.

3.2.1.3 EBSD measurement parameter

TSL Solutions KK is one of the leading companies in the development of *in-situ* EBSD stages and performed the high temperature *in-situ* EBSD measurements. The measurements are conducted with a scanning electron microscope JSM-7001F with field emission gun equipped with an EDAX/OIM system version 7.1 with DigiView detector from TSL Solutions KK. For the measurement, the IAR material state is used. The EBSD sample exhibited dimensions of 5x6x0.5 mm^3 and was prepared by mechanically grinding and polishing with a 0.02 µm acidic alumina suspension in the final step. A schematic representation of the specimen geometry and the EBSD measuring area with respect to the position of the thermocouple is given in Fig. 28.

5 mm

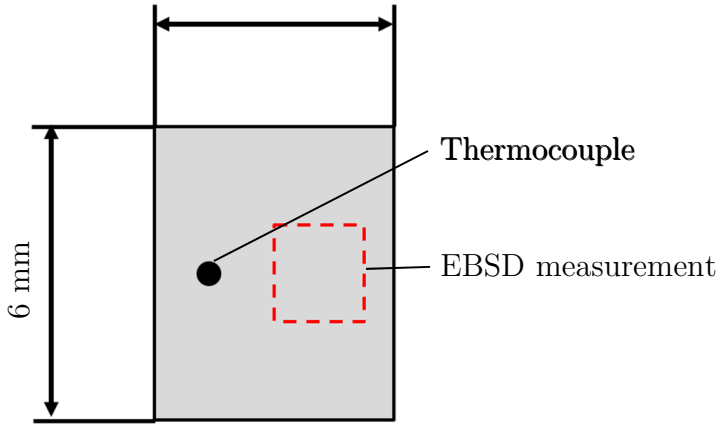

Fig. 28: Schematic representation of the sample geometry for high temperature in-situ EBSD measurements with spot welded thermocouple on the samples surface and highlighted position of the EBSD measurement.

Stepped heating were carried out by a second-generation high temperature heating stage HSEA-100 from TSL solution KK. Temperature as a function of the time of the experiment is illustrated in Fig. 29. For the whole experiment a heating rate of 3.3 °C/s between the isothermal temperature steps was chosen. One heating step with holding times of 25 s at 150 °C was applied in order to evaporate contaminations and ensure good quality of the surface and thus measurement at elevated temperatures. EBSD measurements are carried out during isothermal holding steps at 730 °C, 850 °C and 1030 °C (i.e. industrial solution treatment temperature) and during cooling at 215 °C, 205 °C, 195 °C, 185 °C, 170 °C, 140 °C and 110 °C.

Already at 215 °C martensite was present in these EBSD measurements, which is approximately 100 °C above M_S determined by HT-CLSM or dilatometry. A reason for such uncertainties could be the contact and the position of the spot welded thermocouple, which is illustrated in Fig. 28. Although, the measured temperature of the austenite formation is in good agreement with HT-CLSM and dilatometry. This indicates that the contact of the thermocouple only during the cooling process is weakened. Therefore, the martensite formation during cooling does not correlate well with the measured temperature. However, the martensite phase fraction is determined and correlated with block size and KAM, which is independent from the temperature measurement.

Additionally, EBSD measurements are carried out before and after the heat treatment at room temperature, i.e. for the IAR and AS material state respectively. For room temperature EBSD measurements and during cooling, step sizes of 300 nm are used. For high temperature *in-situ* EBSD measurements, a step size of 1 µm is chosen in order to enhance the scan speed and

reduce thermal drift. For the generated EBSD data illustrated with IPF color coding, a grain dilation cleanup is applied with a grain tolerance angle of 5 ° and a minimum grain size of 4 pixel with the software Orientation Imaging Micrograph (OIM) 7 from EDAX in order to reduce noise of the measurement. For EBSD data used for the illustration of KAM, only data points with a CI above 0.2 are used and no additional cleanup is applied. The KAM is calculated for the next 2 neighbors with misorientations between 0 and 5°.

The reconstruction of prior austenite orientation of the original martensitic crystal orientation was carried out with the reconstruction algorithm of Nyyssönen et al. [46] with an inflation power of 1.4 and the MTEX Toolbox 5.1.1 in the MatLab version R2018a.

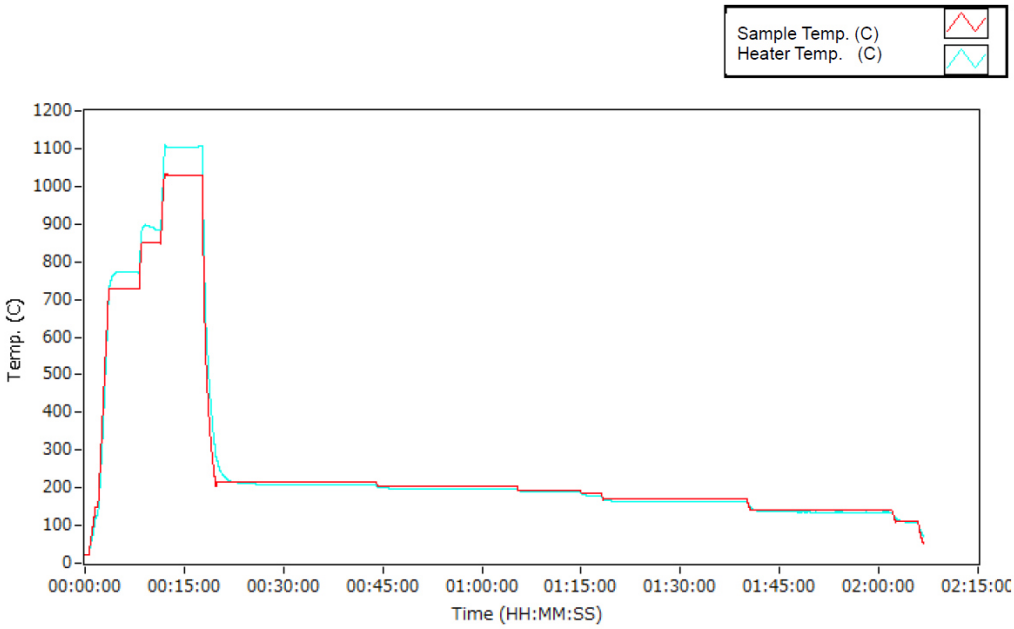

Fig. 29: Measured temperature over time for heating stage (blue) and sample (red) during in-situ high temperature EBSD measurements. The position of the thermocouple with respect to the EBSD measurement position on the sample surface is illustrated in Fig. 28. The temperature was controlled by the sample temperature.

Beside the EBSD measurement of the AS material state from TSL solution KK, two further EBSD measurements of the AS material state and 3 EBSD measurements of the CG material state are conducted by the Materials Center Leoben Forschung GmbH with a scanning electron microscope type Auriga 40 from Zeiss with field emission gun and equipped with a Hikari Super EBSD camera from EDAX. Each EBSD measurement is conducted with a step size of 200 nm and a measuring area of 300x300 µm² except one measurement of the CG material state, which is 360x300 µm². The preparation of the sample is equal to the high temperature *in-situ* EBSD measurements

and the generated data was evaluated with the same software. A quantitative martensite variant distribution is calculated for each EBSD measurement in order to calculate a standard deviation of the number fraction of each martensite variant. This standard deviation is used as error bar for the quantitative martensite variant distribution in chapter 4.3.2. However, for the IAS material state only one EBSD measurement is conducted and therefore no error bars are calculated.

3.2.2 High Temperature Confocal Laser Scanning Microscopy

HT-CLSM measurements were performed in Argon atmosphere heated in an infrared heating stage with a heating rate of 3.3 °C/s to 1030 °C followed by isothermal holding for 10 min and subsequent cooling to room temperature with a mean cooling rate of 0.33 °C/s. A schematic illustration of the experimental setup is given in Fig. 30. For these investigations, specimens were prepared in dimensions of 5x6x0.5 mm^3 by mechanically grinding and finished with a 1 µm diamond suspension polish. For additional information about the used HT-CLSM facility the reader is referred to Bernhard et al. [94].

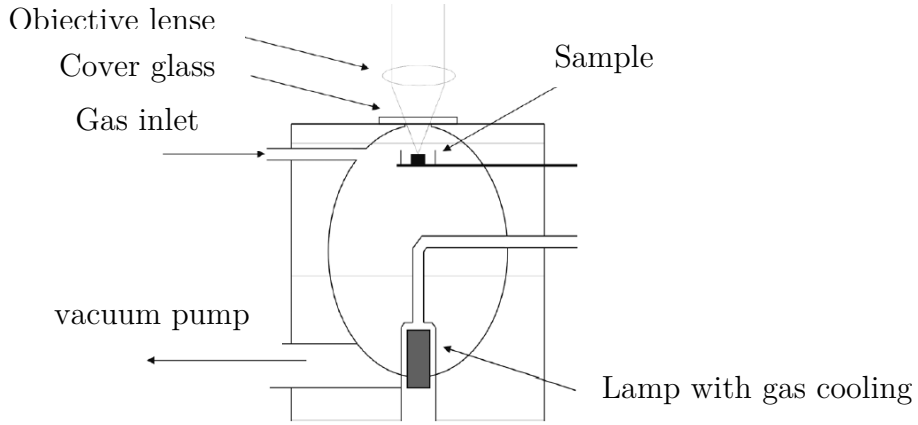

Fig. 30: Experimental setup of the HT-CLSM measurements [94] *indicates the position of the sample with respect to the observation position of the micoscope (i.e. objective lense) and the position of the heater (i.e. lamp with gas cooling)*

3.2.3 Dilatometry

In this thesis, a dilatometer was used in order to conduct the heat treatments with well defined heating or cooling rates. The dilatometer used was a TA instruments dilatometer type 805-l/A. The temperature measurement was carried out using a spot welded thermocouple type S at half length of a cylindrical dilatometer sample with a diameter of 4 mm and a length of 10 mm.

In chapter 4.2.2.2, three different isothermal holding steps were applied with heating rates of 3.3 °C/s between these steps. The parameters for heat treatment (1) to (3) are given in Table 3.

Table 3: Temperature and time of the heat treatments for the ex-situ evidence of the austenite memory effect (1), spontaneous recrystallization (2) and verification of the presence of low angle grain boundaries (LAGB) (3). T1 and T2 are the temperature values for chosen isothermal holding steps and t1 and t2 are the respective holding times.

Heat treatment	T1 [°C]	t1 [h]	T2 [°C]	t2 [h]
(1)	730	1	-	-
(2)	1030	0.5	-	-
(3)	730	1	1030	0.5

3.2.4 Determination of the prior austenite grains

In order to determine the prior austenite grains, respectively their boundaries, based on results on grain boundaries of the martensitic matrix, two different approaches are used in this work, i.e. electrolytic etching and reconstruction of prior austenite.

Electrolytic etching

The first approach is an electrolytic etching routine specially designed for prior austenite grain boundary etching of PH 15-5. Before etching, the samples are mechanically grinded with SiC sandpaper with a final grit size of 1000 and subsequently polished with 1 µm diamond suspension. Electrolytic etching was carried out at room temperature using a LectroPol-5 by Struers with a stainless steel electrode and an electrolyte consisting of water-based nitric acid with an acid concentration of 65 vol.%, available as ready-to-use dilute solution by Carl Roth GmbH & Co KG. The etched surface was 0.5 cm^2 in size and the device's maximum flow rate of 20 was used. The

electrolytic etching consists of two steps. In the first step 1 V is applied for 100 s and in the second step 2.5 V are applied for 18 s. A detailed description of the etching routine and its validation is given in publication A. The electrolytic etching routine only reveals prior austenite grain boundaries but no twin boundaries [95].

Reconstruction of prior austenite

The second approach for the determination of prior austenite grain boundaries is the reconstruction of prior austenite grains from EBSD data of the martensitic matrix with the algorithm of Nyyssönen et al. [46]. Therefore, an inflation power of 1.4 is used. The reconstruction routine also reveals prior austenite twin boundaries.

After the revealing of prior austenite grain boundaries, the prior austenite grain size is determined by the linear intercept method with the software Stream from Olympus. An equidistant grid of 10 by 10 lines is used. The grain size is calculated by the software in an ASTM grain size number (GS_{ASTM}) and then converted into grain size in µm ($GS_{µm}$) by Equation (8)

$$GS_{µm} = \frac{1}{\sqrt{8 * 2^{GS_{ASTM}}}} * 10^3 \tag{8}$$

Error bars ($GS_{µm}^{+/-}$) of the determined ASTM grain sizes are calculated with Equation (9) [96] and then converted into µm by Equation (8). The error bars illustrate the error of the linear intercept method with respect to the number of grains n_G that are intercepted but don't provide information about the variation of grain size on different sample positions.

$$GS_{µm}^{+/-} = \frac{1.49}{\sqrt{n_G}} \tag{9}$$

The determination of austenite grain size after reconstruction method exhibit a smaller austenite grain size in comparison to electrolytic etching routine due to the consideration of austenite twin boundaries. Therefore, austenite grain size determined after reconstruction of prior austenite and with consideration of austenite twin boundaries is referred to austenite twin size and the austenite grain size determined after electrolytically etching is referred to austenite grain size in the following. Results of chapter 4.1 indicate the austenite twin size as effective grain size for the martensitic transformation and therefore is referred from that point to effective grain size.

4 Results and Discussion

In order to describe the microstructural evolution of austenite in PH 15-5 steel during solution annealing and its influence on the evolving martensitic substructure, results of the characterization of the martensitic substructure of the as-received material state, the microstructure development during solution annealing and the influence of austenite state on the resulting martensitic substructure are presented and discussed. The focus is especially laid on the microstructural development of austenite and its interplay with the evolving martensitic substructure that is formed during subsequent cooling, as the martensitic substructure is crucial for the mechanical properties of the final component.

4.1 Initial state of the as-received material

The following chapter presents the characterization of the EAR material state of the investigated PH 15-5 steel concerning prior austenite grain structure and martensitic substructure such as block size and variant distribution. Furthermore, retained austenite is determined for the IAR material state. The as-received material state is the initial material state for solution annealing and therefore subsequent investigations of the microstructural development during solution annealing are based on the results of this chapter.

4.1.1 Prior austenite grain structure

In order to gain new insights in the interplay of between austenite grain structure and the subsequently formed martensitic substructure, the prior austenite grain structure of the EAR material state is investigated and correlated to the evolving martensitic substructure. Therefore, prior austenite grain boundaries are electrolytically etched and supplementary EBSD measurements of the martensitic microstructure are conducted, enabling the investigation of prior austenite by pole figure analysis and reconstruction methods. Results of this chapter complement findings of publication A, attached in the appendix of this thesis.

Prior austenite grain boundaries are clearly indicated by the electrolytic etching illustrated in Fig. 31a. The prior austenite grain structure consists of smaller globular grains and larger grains, stretched in the horizontal direction. During hot deformation with incomplete recrystallization, austenite grains are stretched in the direction of the largest deformation [97]. Therefore, a slight deformation texture of the microstructure is assumed. Fig. 31b

shows the martensitic microstructure obtained by an EBSD measurement of the area highlighted in Fig. 31a illustrated with IPF color coding in overlap with IQ in order to indicate prior austenite grain boundaries.

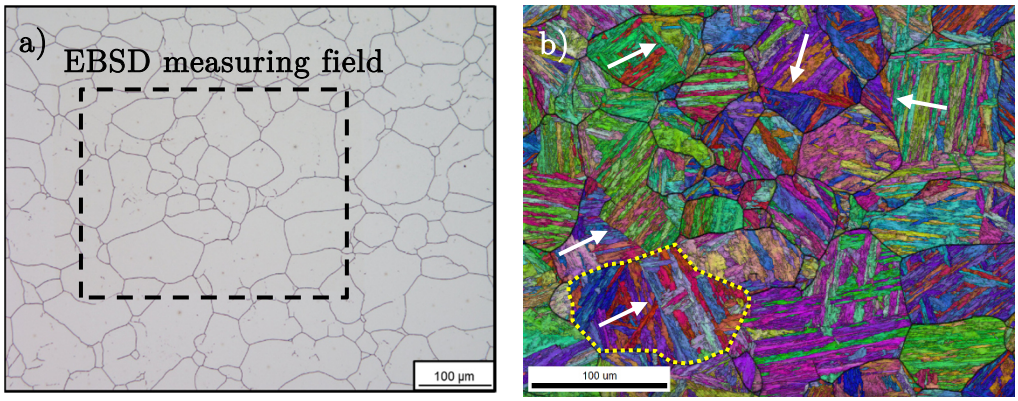

Fig. 31: Prior austenite grain boundaries revealed by electrolytic etching (a) and correlative EBSD measurement of the martensitic microstructure illustrated with an overlay of IPF and IQ (b) of the EAR material state. Unetched boundaries are highlighted by white arrows [95].

In some prior austenite grains, unetched boundaries indicated by the martensitic microstructure are visible and highlighted with white arrows. A (001) pole figure analysis of one prior austenite grain exhibiting such unetched grain boundary, highlighted in Fig. 31b, is given in Fig. 32a. The (001) pole figure shows an overlap of two almost complete near-KS pattern which can be separated by a detailed analysis of part I and part II of the grain (Fig. 32b and c). The symmetry in the overlap of the near-KS pattern (Fig. 32a) gives a hint for a crystallographic relationship between part I and part II of the prior austenite grain. Fig. 32d schematically illustrates the prior austenite crystal orientation for part I (red) and part II (blue). This is done by comparing the experimental pattern of the reflexes in the (001) pole figure with the reflexes of the ideal KS OR (Fig. 1). A similar crystallographic relationship as between part I and II is observed for twins in deformed Cu single crystals by Blewitt et al. [98]. This indicates a twin relationship of part I and II of the prior austenite grain.

Consequently, it can be concluded that twin boundaries are not attacked by the electrolytic etching routine. This is beneficial for a determination of the prior austenite grain size according to ASTM E112 because here, twin boundaries have to be ignored [95]. In order to investigate the role of the parent grain regarding the martensitic transformation, twin boundaries are an important microstructural parameter and therefore have to be considered.

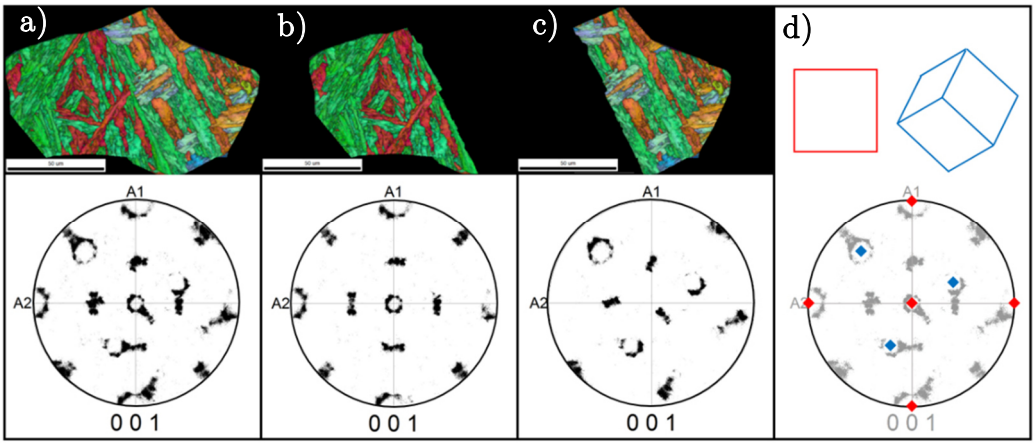

Fig. 32: Analysis of the (001) pole figure of an etched prior austenite grain with overlapping KS pattern (a) consisting of two separate KS pattern indicated by part I (b) und part II (c) of the grain. This symmetric overlap of KS pattern is indicating a twin relationship of prior austenite grains (d) [95].

In order to analyze twin structure of prior austenite in the total EBSD measurement range, the prior austenite crystal orientation is reconstructed by using the method described in chapter 2.1.4.1 from the crystal orientation data of martensite and is illustrated in Fig. 33a with IPF color coding, whereas high angle grain boundaries are drawn black. A comparison of Fig. 33a and Fig. 31a and b indicates more high angle grain boundaries in the reconstruction of prior austenite than revealed by electrolytic etching. Furthermore, every supposed grain boundary, highlighted with white arrows in Fig. 31b, is also visible in the reconstruction of Fig. 33a. Different twin boundary types are calculated from the reconstructed austenite crystal orientation (Fig. 33a) and highlighted in Fig. 33b. Twin boundaries exhibit specific crystallographic relations compared to the random orientation of grain boundaries. According to Humphreys et al. [99], the most common twin types are $\Sigma 3$, $\Sigma 5, \Sigma 7$ and $\Sigma 9$. In order to identify different types of twin boundaries, these specific crystallographic relations between neighboring pixels are examined:

- $\Sigma 3$: 60° between {111} planes
- $\Sigma 5$: 36.87° between {100} planes
- $\Sigma 7$: 38.21° between {111} planes
- $\Sigma 9$: 38.94° between {110} planes

Highlighting the austenite twin boundaries of the reconstruction in Fig. 33 b reveals a good agreement of prior austenite grain boundaries with the electrolytic etching illustrated in Fig. 31b, as every unetched boundary is a

twin boundary. The quantitative twin boundary analysis from the data illustrated in Fig. 33b exhibits a dominant twin boundaries of type Σ3 (highlighted in blue) with an amount of 92.14 % with respect to the total amount of twin boundaries. The other twin boundary types such as Σ5, Σ7 and Σ9 exhibiting significantly lower amounts with 1.17 %, 0.06 % and 6,63 %, respectively. It should be noted that twin boundaries are detected in nearly every prior austenite grain of the experimental as-forged state of PH 15-5. Furthermore, the results validate the findings of the pole figure analysis of Fig. 32 by indicating the investigated boundary inside the austenite grain as Σ3 twin boundary. Relative to the total length of high angle grain boundaries of the completely observed area, the ratio of twin boundaries is 36.5 %. These results evidence a strong twin formation during hot deformation of the EAR material state of PH 15-5.

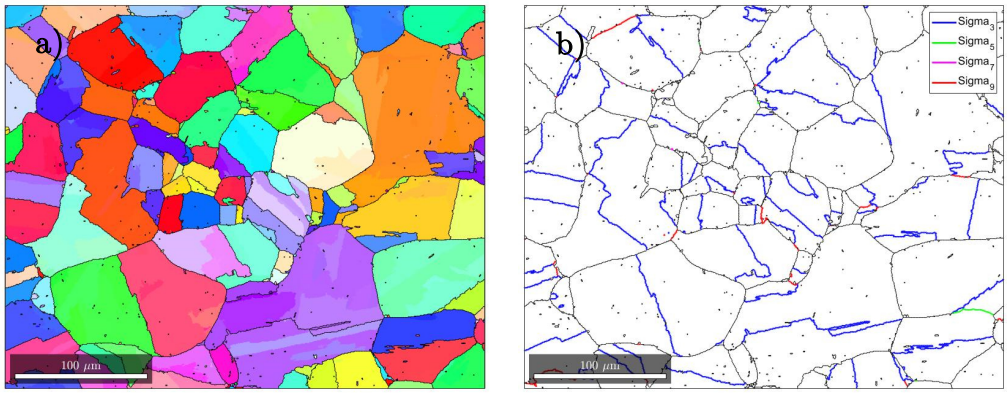

Fig. 33: Reconstruction of the prior austenite grain orientation with IPF color coding and black drawn high angle grain boundaries (>15°) (a) and illustration of different types of twin boundaries (b). The results indicate a high ratio of twin boundaries in the EAR material state.

However, the etching does not attack prior austenite twin boundaries. The formation of two separated near-KS pattern in the two corresponding prior austenite twins in Fig. 32 indicate the austenite twin size as the effective grain size for the martensitic transformation and is therefore in the following referred to effective austenite grain size. However, it is assumed that the strong tendency of twin formation influences the martensitic microstructure.

The effective grain size is 28 µm (austenite twin size), which is significantly lower than 46 µm for the austenite grain size. These results illustrate the importance of differentiating between austenite grain and twin size as it is discussed in chapter 3.2.4 of this work.

It is reported in literature that twin formation plays an important role for the nucleation of dynamic recrystallization in materials with low stacking fault energy [100]. Mirzadeh et al. [100] related the formation of annealing

twins to the dynamic recrystallization of AISI 304 H austenitic stainless steel with the composition: 0.064 m.% C – 18.35 m.% Cr – 8.96 m.% Ni – 1.52 m.% Mn – 0.45 m.% Mo – 0.83 m.% Si. In order to examine the stacking fault energy as possible reason for the strong twin formation in the EAR material state of PH 15-5 steel, the stacking fault energy is estimated and compared to those of AISI 304 H stainless steel. Therefore, the approach of Rhodes et al. [101] for austenitic stainless steel is used represented by Equation (10).

$$\gamma_{\mathrm{SFE}} = 1.2 + 1.4 * \mathrm{Ni} + 0.6 * \mathrm{Cr} + 17.7 * \mathrm{Mn} - 44.7 * \mathrm{Si} \qquad (10)$$

In order to obtain the stacking fault energy γ_{SFE} in mJ/m², the contributing alloying elements Ni, Cr, Mn and Si are in m.%. The estimated stacking fault energies are 13.9 mJ/m² for PH 15-5 and 14.6 mJ/m² for 304 H. The order of magnitude for the calculated stacking fault energies is in good agreement with recent investigations on austenitic stainless steels [102]. The estimation illustrates that PH 15-5 exhibits a comparable low stacking fault energy to austenitic stainless steel. Therefore, the observed twin formation may be contributed to annealing twin formation as previous stage to dynamic recrystallization. This is in good agreement with the slight deformation texture of austenite grains in Fig. 31a. The identification of the strong annealing twin formation during hot deformation of PH 15-5 and the austenite twin size as effective grain size for the martensitic transformation opens new paths for the adjustment of the effective austenite grain size during the production and furthermore, the tailoring of martensite substructure size and mechanical properties.

4.1.2 Martensite in PH 15-5

Based on the prior austenite reconstruction algorithm, the OR for the EAR material state is calculated. This enables the crystallographic definition and determination of martensite block boundaries and the identification of martensitic variants, which both influence the mechanical properties of the final component. The results are presented and discussed in the following chapter.

4.1.2.1 Determination of block boundaries

In order to analyze the martensitic block structure as important parameter for the mechanical properties of the final component, a crystallographic determination of the martensite block boundary angle of a specific material

state is necessary. The later presented calculation of martensite block size is based on the determination of block boundaries. An often used definition of martensite block boundary angle is the minimum angle between two martensitic variants, e.g. 10.5° between variant 1 and 4 for KS OR [53,55]. Instead of choosing the minimum angle between two martensite variants of an existing OR model such as KS or NW, the OR of the EAR material state is calculated with the algorithm of Nyyssönen et al. [46], which is described in chapter 2.1.4.1. Fig. 34 illustrates the difference between KS OR (Fig. 34a) and the calculated OR from experimentally determined data (Fig. 34b) in a (001) pole figure.

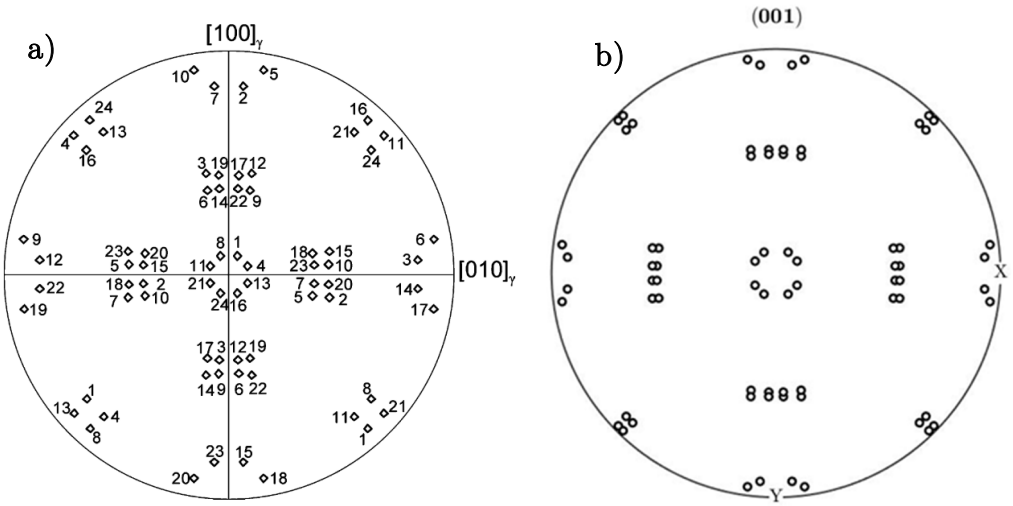

Fig. 34: Comparison between ideal KS OR (a) and calculated OR from experimentally determined data of the EAR material state with the algorithm of Nyyssönen et al. [46] *(b). In order to determine the martensite block boundary angle, the minimum distance between the projection points of two martensite variants is used. Therefore, the calculated OR from experimentally determined data of the EAR material state (b) exhibiting a smaller block boundary angle compared to KS OR (a).*

The difference of the calculated OR to KS OR is quantified by the calculation of the angular deviation between the closed packed planes ($\{111\}_\gamma$ and $\{011\}_{\alpha'}$) and the closed packed directions ($\langle 011\rangle_\gamma$ and $\langle 111\rangle_{\alpha'}$). These angles are zero for ideal KS OR (cf. chapter 2.1.1.1). The angular deviation between $\{111\}_\gamma$ and $\{011\}_{\alpha'}$ is 2.9° and between $\langle 011\rangle_\gamma$ and $\langle 111\rangle_{\alpha'}$ it is 1.5°. Qualitatively, this is also visible in Fig. 34, as the reflexes of the calculated OR are more close together and tend to overlap in some regions of the pole figure. Such deviation from KS OR is caused by a deviation of the ideal $(111)_\gamma$ habit plane for the martensitic transformation according to KS OR [55]. According to Bhadeshia et al. [54], different alloying compositions exhibit different habit planes for the martensitic transformation.

The calculated OR from experimentally determined data of the EAR material state exhibits 5.18° as minimum angle between two martensite variants (i.e. variant 1 and variant 4) and therefore is used as martensite block boundary angle. The smaller block boundary angle of 5.18° compared to the KS OR with 10.5° is consistent with the smaller distance between the projection points in Fig. 34b compared to Fig. 34a.

The determined minimum block boundary angle is used to illustrate block boundaries in Fig. 35 by black lines for angular deviations between two pixels larger than 5.18°. A comparison to the literature cannot be taken because there is no comparable definition of block boundaries in literature to the knowledge of the author. Regions with nearly the same IPF color coding are now visible as different blocks by the drawn block boundary lines.

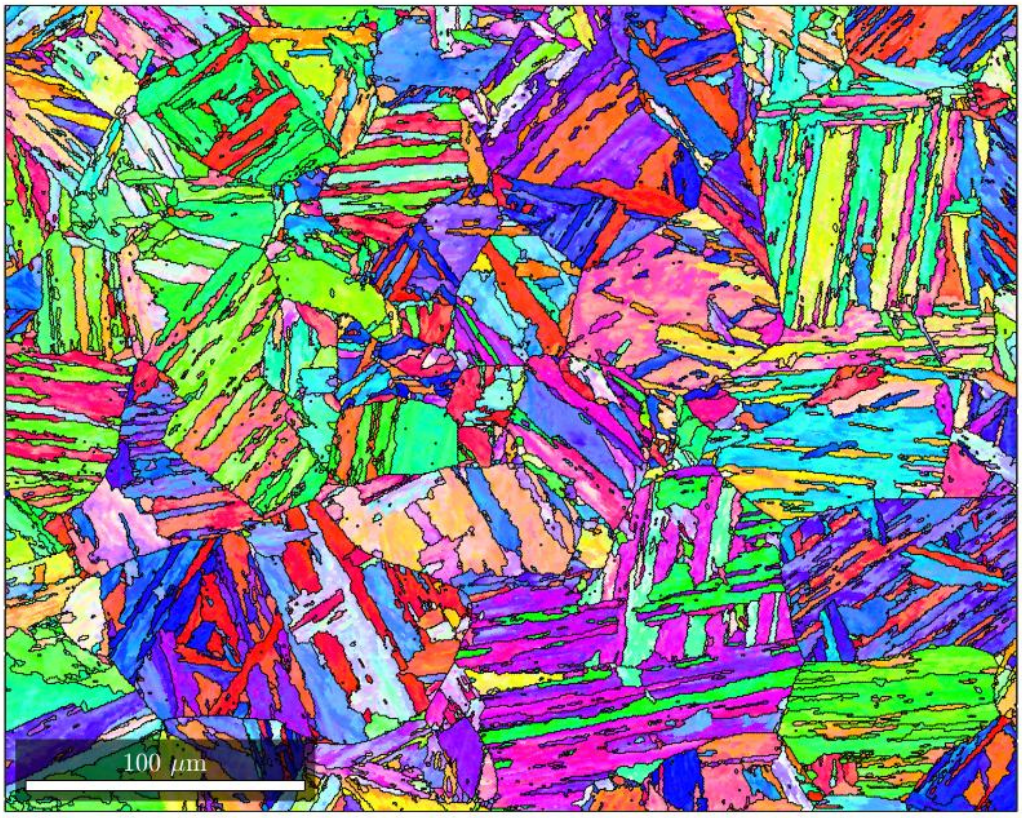

Fig. 35: IPF of martensite with black drawn block boundaries larger than 5.18° based on the minimum angle between two martensitic variants according to the calculated OR. Regions with nearly identical color coding are now identified as different martensite blocks.

The distribution of the martensite block size according to number fraction and area fraction is illustrated in Fig. 36. The number fraction of the block size, in Fig. 36a, indicates that most of the detected blocks are very small, as the maximum of the distribution is the detectable smallest block size.

Therefore, only block sizes determined with number fraction with the same smallest detectable block size are comparable, as it is described in chapter 3.2.1.2. Fig. 36b exhibits a local maximum for higher block sizes and is therefore less sensitive to the smallest detectable block size.

The mean martensite block size of the EAR material state is 3.19 µm calculated as number fraction and 16.49 µm calculated as area fraction. The same approach for the determination of martensite block boundaries and mean martensite block size is used in chapter 4.3.1 of this work.

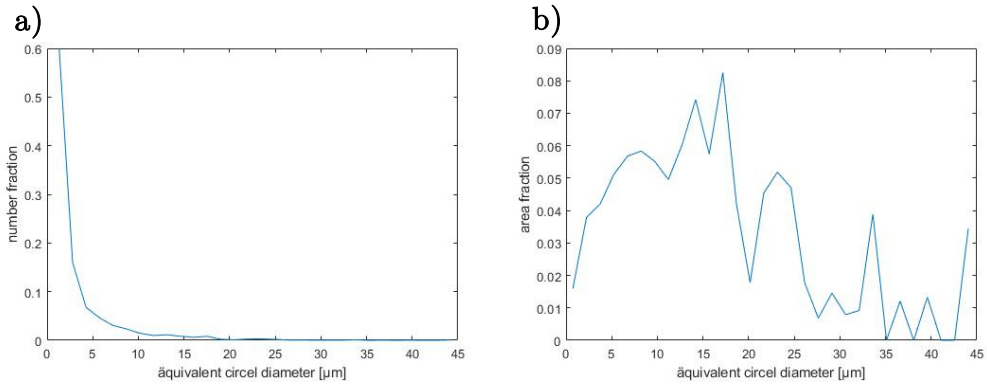

Fig. 36: Calculated number fraction (a) and area fraction (b) of the block size of the EAR material state.

4.1.2.2 Determination of quantitative martensite variant distribution

In order to get information about preferred variants, blocks or packets in the EAR material state, a quantitative variant identification is carried out. With this examination, information about the deformation texture of austenite can be concluded due to the inheritance of inner structure of austenite to martensite, presented in chapter 2.1.3.

The spatial distribution of the martensite variant identification is illustrated in Fig. 37. To this end, the different packets (P1 - P4) are illustrated separately. The three different colors red, green and blue represent the three different blocks inside one packet whereas, lighter and darker shades of the color represent the corresponding subblocks (cf. Table 1). E.g. the color red in packet P1 represents the first block B1 and the lighter and darker shades of red represent variant 1 and variant 4, respectively, which are forming a subblock. The same color code is used in Table 1 for the illustration of the 24 KS variants. Inactive variants inside the illustration of a specific packet are drawn in grey. The spatial variant distribution in Fig. 37 indicates less area fraction of variants in the packets of type P2.

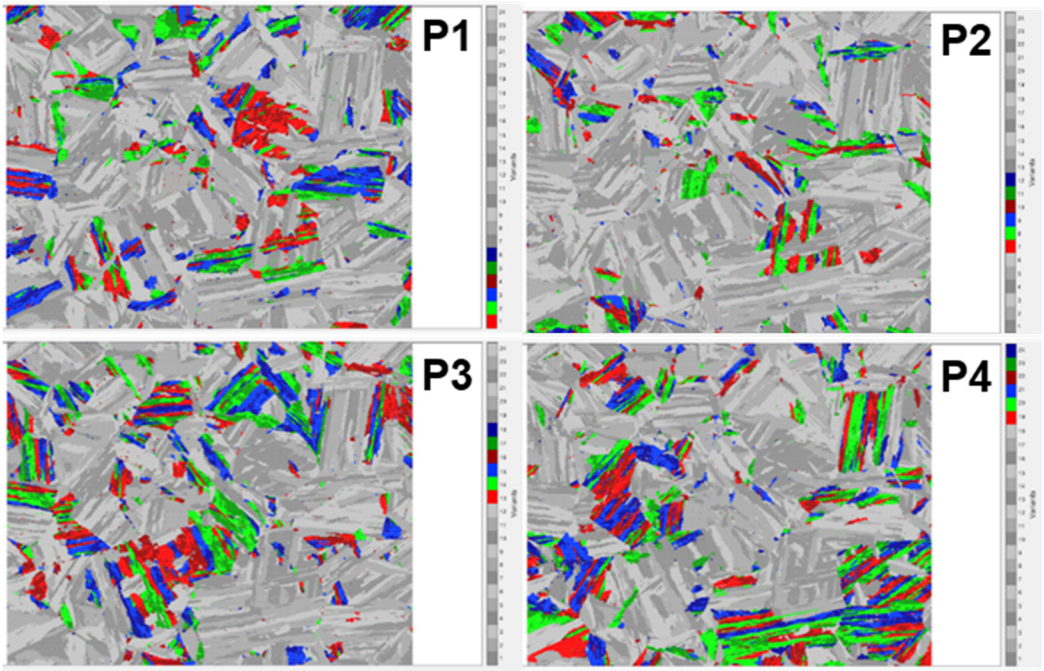

Fig. 37: Spatial distribution of martensite variants of the EAR material state for packet P1, P2, P3 and P4. Originating from this variant identification, the quantitative variant distribution (Fig. 38) is calculated.

Based on the variant identification a quantitative determination of the area fraction of the various martensite variants was done (Fig. 38) by counting the pixels of each variant and calculating the number fraction relative to the total pixel number, which is identical with the area fraction. The horizontal dashed line in Fig. 38 indicates a number fraction of 0.0417 (i.e. 1/24) corresponding to an equal distribution of all martensitic variants. Variants exceeding this line are indicated as preferred. Therefore, the packets P3 and P4 are preferred as every variant exceeds the equal distribution line. According to Miyamoto et al. [35] such so-called variant selection is typical for lath martensite evolving from deformed austenite grains, as it is presented in chapter 2.1.3 (Fig. 10). Thereby, the OR between austenite and martensite inherits the deformation texture from austenite to the martensitic microstructure. This observation is in accordance to the slight deformation texture of prior austenite grains which is assumed to be visible in Fig. 31a.

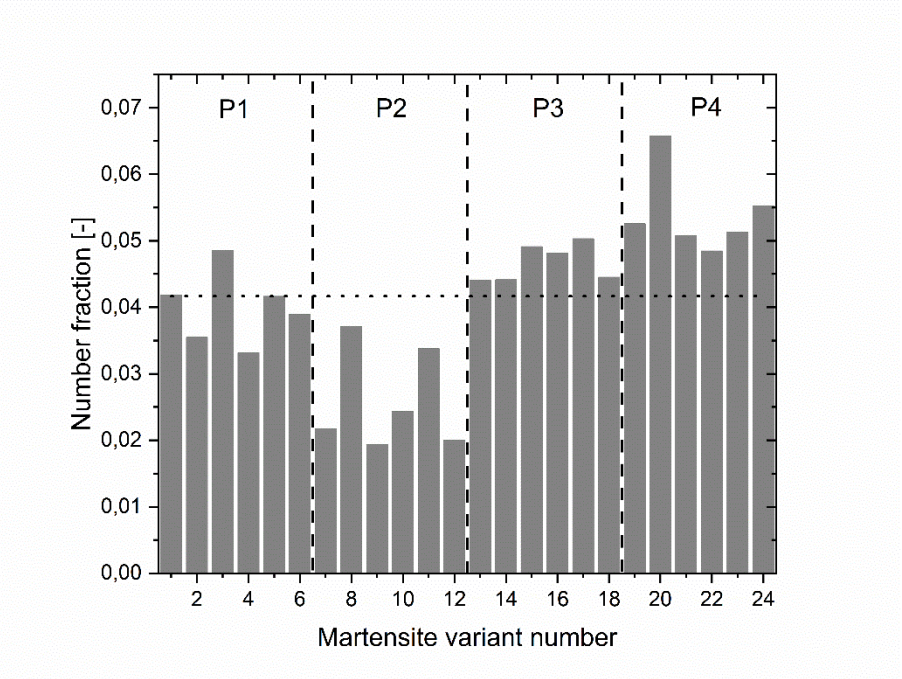

Fig. 38: Histogram of martensitic variant distribution for all 24 martensite variants. The grey dashed line represents the number fraction of an equal distribution of all variants (i.e. 1/24). The packets P3 and P4 are preferentially formed in the EAR material state.

4.1.3 Retained austenite

The retained austenite amount of the IAR material state was determined by XRD measurement. Fig. 39 shows the XRD pattern indicating that no austenite reflexes are present, as it is also shown in publication B. Additional reflexes ($(002)_{Mo}$, $(112)_{Mo}$) in the XRD pattern originate from the molybdenum heating band used in the XRD chamber and are, thus, not further considered.

Please note, that due to the detection limit of about 1 m.% the presence of inter-lath retained austenite cannot be excluded despite the fact, that no retained austenite is detected with XRD. Liu et al. [81] reports the presence of inter-lath retained austenite in soft martensitic steel. This type of retained austenite is located at martensite lath boundaries and exhibits a film-like shape with only a few nm in thickness [1].

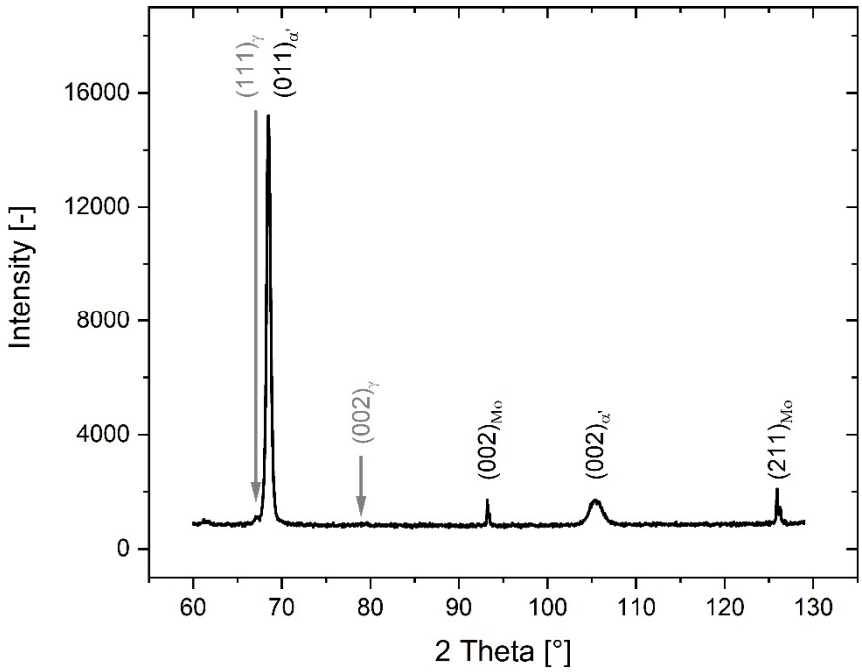

Fig. 39: XRD pattern of the IAR material state of PH 15-5 exhibiting no reflexes of austenite (i.e. no retained austenite can be detected). The presence of little amounts of inter-lath retained austenite cannot be excluded due to the detection limit of austenite of approximately 1 m.% [73].

4.2 Microstructure development during solution annealing

The following chapter describes the microstructure development during solution annealing of the IAR material state of PH 15-5 concerning austenitization phenomena such as austenite memory effect and spontaneous recrystallization. Furthermore, the martensitic transformation of the final austenite microstructure is investigated. The solution annealing is the last austenitization step of the PH 15-5 in the industrial manufacturing process and therefore the development of the austenite microstructure and its influence on the evolving martensite substructure during subsequent cooling is crucial for the mechanical properties of the final component.

4.2.1 Austenite memory effect in PH15-5

This chapter is a summary of findings from previous publication: “Evidence of austenite memory in PH 15-5 and assessment of its formation mechanism” which is attached to this thesis as publication B. It describes the evidence and mechanism of austenite memory effect in PH 15-5. In this

chapter, high temperature *in-situ* EBSD measurements are presented up to an austenitization temperature of 850 °C.

4.2.1.1 Evidence of austenite memory effect

In order to analyze the development of reversed austenite as a function of grain size and crystal orientation EBSD measurements are carried out at room temperature and at 730 °C and 850 °C.

Fig. 40a - c show the microstructure development from martensite at room temperature (Fig. 40a) to austenite at 730 °C (Fig. 40b) in IPF color coding and 850 °C (Fig. 40c) in IPF and overlapped IQ color coding. Additionally, high angle grain boundaries (i.e. >15°) in Fig. 40b and c are drawn in black. At 850 °C a phase fraction of 0.98 for austenite is observed, indicating a nearly complete austenitization. Reversed austenite, highlighted in Fig. 40c, exhibits a sub-structure that is appears to be parallel to the former martensite block boundaries, which is shown in Fig. 40a.

In order to compare the reversed austenite crystal orientation and grain size to those of prior austenite, a reconstruction is carried out. Fig. 40d illustrates the reconstruction of prior austenite grain structure in IPF color coding out of the martensite crystal orientation of Fig. 40a. A comparison of Fig. 40d and Fig. 40b and c exhibits the same grain size, grain shape and crystal orientation of reconstructed prior austenite and reversed austenite and therefore evidences the austenite memory effect in PH 15-5. Additionally, the (001) pole figure of the highlighted prior austenite grain (solid line) in Fig. 40a is compared to those of reversed austenite highlighted in Fig. 40c (solid line) and illustrated in Fig. 40e. The pole figure of martensite exhibits a typical near-KS OR (black) with reflexes from reversed austenite (red) at the position as it is expected for prior austenite (cf. Fig. 1). This fact indicates that reversed austenite rebuilds the crystal orientation of prior austenite. Therefore, the results of the pole figure analysis validate the findings of prior austenite reconstruction and directly evidence the austenite memory effect in PH 15-5 for temperatures up to 850 °C. Consequently, the austenite memory effect is evidenced for the first time in the commercial alloy PH 15-5.

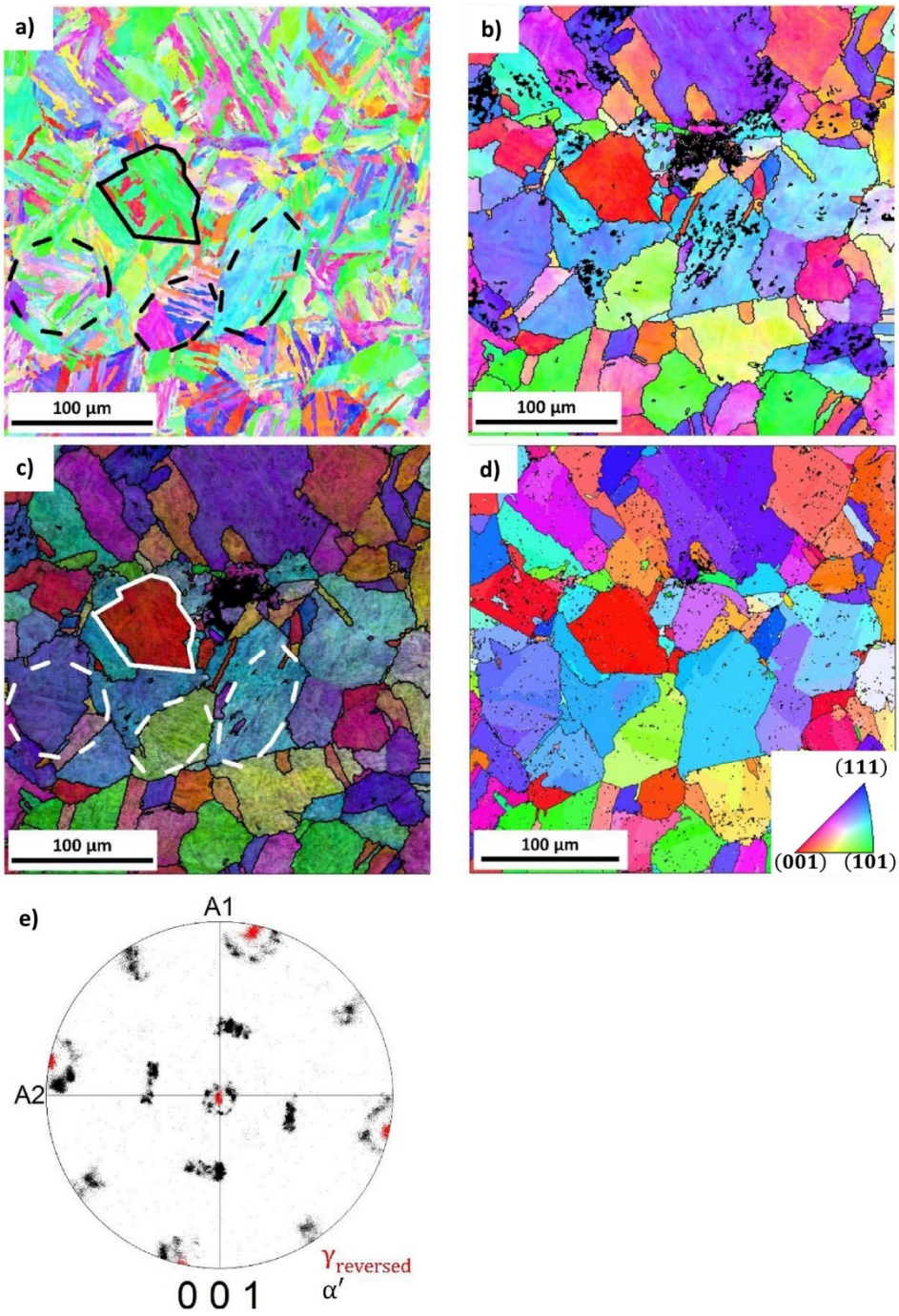

Fig. 40: IPF color coding of martensite at room temperature (a), austenite at 730 °C (b) and austenite at 850 °C (c) on the same sample position. A comparison of the reconstructed prior austenite grain structure (d) evidences the austenite memory effect. Black drawn lines in (b) - (d) represent high angle grain boundaries with a misorientation larger 15 °. Additionally, the (001) pole figure of one prior austenite grain highlighted in (a) and (c) validates the same crystal orientation of reversed austenite as for prior austenite. Dashed lines highlight a similar structure of fresh formed austenite exhibiting austenite memory effect (c) and the martensitic block structure (a).

4.2.1.2 Mechanism of the austenite memory effect

Based on the findings presented in publication B, formation mechanism (IV) is assumed to be dominant for the formation of reverted austenite in PH 15-5 and is described in detail in chapter 2.2.1. Mechanism (IV) describes a variant restriction between martensite laths and reversed austenite influenced by an internal stress field, thus, the crystal orientation of reversed austenite is limited to the prior austenite crystal orientation. For mechanism (IV) Nakada et al. [19] reports that austenite planes close to $\{111\}_{\gamma}$ are parallel to the martensite lath boundary plane $\{011\}_{\alpha'}$ and directions close to $\langle 011\rangle_{\gamma}$ are parallel to the $\langle 111\rangle_{\alpha'}$ longitudinal direction of the martensite lath. Hence, freshly formed austenite has a lath-like morphology (i.e. acicular austenite) which is nearly parallel to the longitudinal direction of the martensitic block structure. This acicular shape of austenite is clearly visible for early stages of austenitization (e.g. after inter-critical annealing) [75].

In the present work, the lath-like morphology of reversed austenite parallel to martensitic block-structure observed with high temperature *in-situ* EBSD (Fig. 40) gives an indication for the existence of acicular shaped austenite in the early stages of austenitization. However, acicular austenite cannot be directly observed in separated regions as it is reported for inter-critical annealing experiments because of the proceeded stage of austenitization and thus high fraction of austenite as well as the limited lateral resolution of the EBSD measurements as it is described in the following.

According to the findings of Zhang et al. [84], reversed austenite formed by mechanism (IV) requires a coherent interface to the surrounding martensite laths. Martensite laths inside one block exhibit low angle grain boundaries (LAGB) with a misorientation up to 5° [63]. Therefore, coalescence of reversed austenite, nucleated and grown on neighboring martensitic laths with only a small orientation deviation, can lead to the generation of LAGB (i.e. GND) in reversed austenite. Alternations of IQ inside reversed austenite grains found in Fig. 40c (surrounded by dashed lines) indicate discontinuities of crystal orientations and give a hint for the presence of LAGB. It is assumed that the width of acicular austenite regions is in the same magnitude as the martensitic lath width of approximately 200 nm and therefore cannot be resolved with an EBSD step size of 1 µm. Based on the presented comparison of literature with results of publication B, a basic model is postulated in Fig. 41 [73]. It illustrates the nucleation and growth of reverted austenite based on mechanism (IV) and furthermore describes the heritage of LAGB during austenitization due to coalescence of neighboring acicular austenite regions with coherent interface to the martensitic matrix.

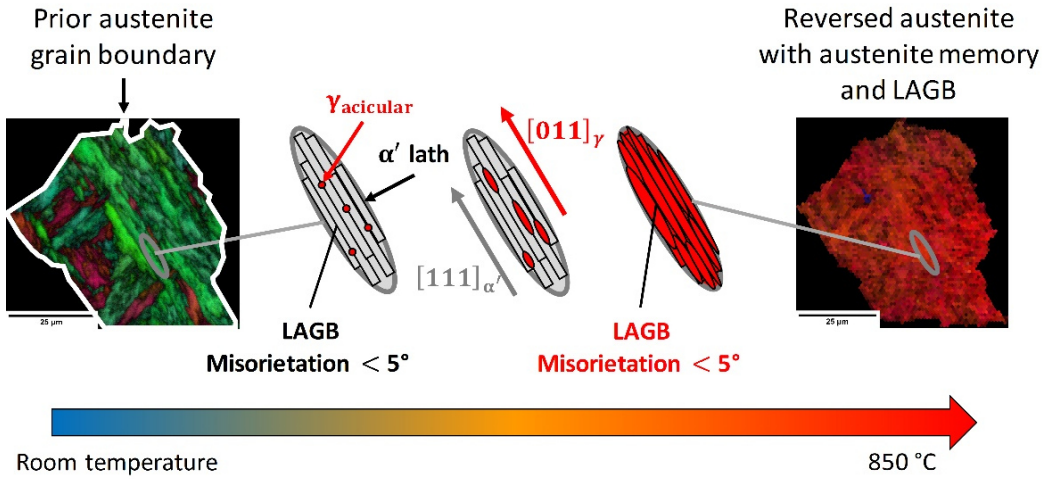

Fig. 41: Inheritance of LAGB from martensitic microstructure to reversed austenite due to the austenite memory effect formed by mechanism (IV). This mechanism produces an austenitic microstructure with enhanced dislocation density compared to classical austenitization (i.e. the nucleation of austenite on prior austenite grain boundaries and subsequent migration of incoherent high angle grain boundaries) [73].

These considerations are consistent to the work of Shinozaki et al. [49,72] which also discuss the potential misorientation enhancement inside austenite grains formed by mechanism (IV). However, the chemical composition of the investigated low alloy steel distinguishes strongly from PH 15-5 and additionally contains an amount of approximately 4 % cementite, which makes it difficult to isolate mechanism (IV) as the only present formation mechanism for the austenite memory effect in this investigated alloy.

Shirazi et al. [50] reports about a higher dislocation density of reversed austenite compared to prior austenite formed by a shear mechanism (cf. Fig. 9) but not for diffusion controlled reversion. The actual work, however, suggests that the proposed diffusion controlled austenitization mechanism can also lead to an enhanced dislocation density, which is distinctly higher than austenite formed by the classical diffusion-controlled transformation (i.e. the migration of incoherent high angle grain boundaries).

4.2.2 Spontaneous recrystallization in PH 15-5

The so-called spontaneous recrystallization phenomenon is an important part of the development of the austenitic microstructure in PH 15-5, as it takes influence on the grain size and dislocation density of austenite. In order to investigate spontaneous recrystallization subsequent to the austenite memory effect, additional high temperature *in-situ* EBSD measurements during solution annealing are carried out. Furthermore, the influence of heating rate and number of successive solution annealing cycles is investigated.

4.2.2.1 *In-situ* evidence of spontaneous recrystallization

According to findings of publication B and the implementation of high temperature *in-situ* EBSD the investigated PH 15-5 exhibits a so-called spontaneous recrystallization as a reduction of the austenite grain size is evidenced for further heating at 1030 °C, which is illustrated in Fig. 42a, c and e.

Fig. 42a, c and e shows the development of microstructure with IPF and overlapped IQ color coding at the same sample position originating from martensite at room temperature (Fig. 42a) over austenite exhibiting the austenite memory effect at 850 °C (Fig. 42c) to austenite exhibiting a completely changed microstructure at 1030 °C (Fig. 42e). A comparison of Fig. 42c and e indicates a change in austenite grain size, crystal orientation and a more homogeneous IQ. The effective austenite grain size reduces from 27 µm to 19 µm. This *in-situ* observation evidences spontaneous recrystallization for the first time in PH 15-5. Furthermore, the KAM from the corresponding regions is calculated (Fig. 42b, d, f) indicating a high misorientation in martensite (Fig. 42b) and austenite with the austenite memory effect (Fig. 42d). This underpins the postulation of an inheritance of LAGB and GND from martensite by mechanism (IV). Furthermore, a decrease in KAM for austenite after spontaneous recrystallization at 1030 °C within the whole observed area (Fig. 42d and f).

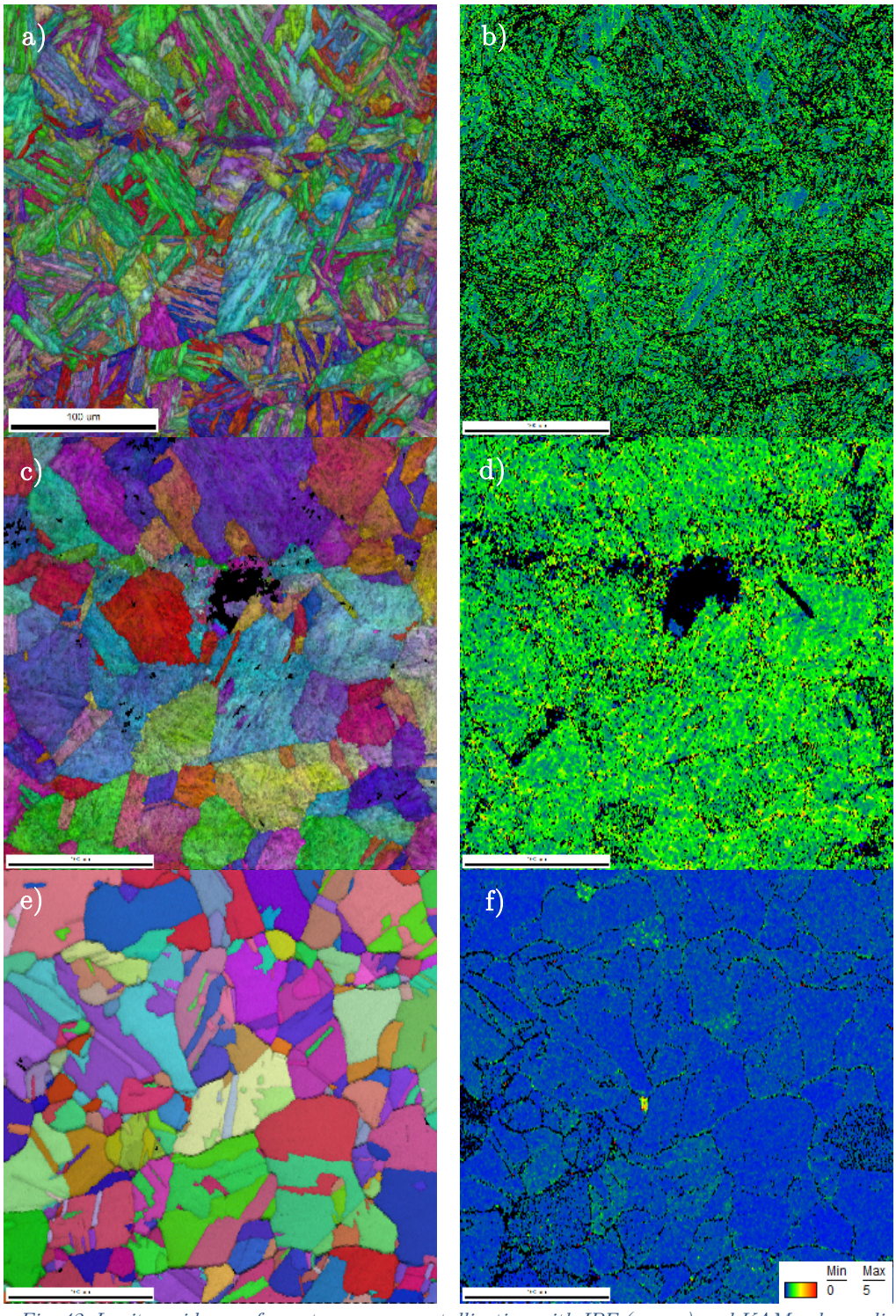

Fig. 42: In-situ evidence of spontaneous recrystallization with IPF (a, c, e) and KAM color coding (b, d, f) during solution annealing. Martensitic microstructure of the IAR material state at room temperature (a, b) transforms to austenite exhibiting austenite memory effect at 850 °C (c, d) with accompanying reduction of austenite grain size (e) and KAM (f) for further heating at 1030 °C (i.e. spontaneous recrystallization). An inheritance of GND from martensite (b) to austenite exhibiting the austenite memory effect (d) is additionally evidenced by the KAM.

A histogram of the observed KAM corresponding to Fig. 42d and f is given in Fig. 43 illustrating a decrease of misorientations inside austenite after spontaneous recrystallization. The mean KAM value reduces from 1.14° before spontaneous recrystallization to 0.36° after spontaneous recrystallization. A comparison with the mean KAM value of martensite at room temperature would be suitable but is not accurate because of different EBSD step sizes.

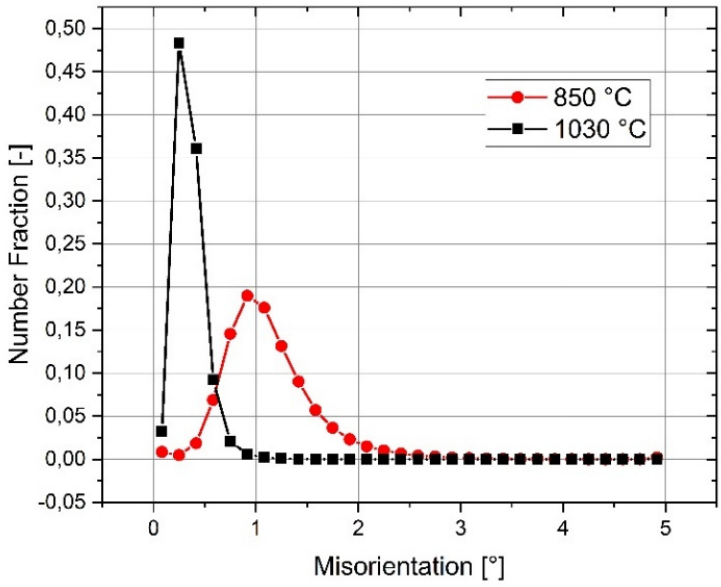

Fig. 43: Histogram of KAM before spontaneous recrystallization at 850 °C and after spontaneous recrystallization at 1030 °C corresponding to Fig. 42d and f respectively. The reduction of KAM indicates a reduction of GND during spontaneous recrystallization.

The results indicate an inheritance of KAM from martensite to austenite exhibiting the austenite memory effect and a homogenous decrease of KAM after spontaneous recrystallization. According to Equation (4), the KAM value is correlated to the GND density and therefore the results underpin the postulated inheritance of GND in chapter 4.2.1.2 of the work and publication B. As described in chapter 3.2.1.2, the calculation of GND out of the KAM value is sensitive to the EBSD step size [91]. The used EBSD step size of 1 µm leads to a calculated ρ_{GND} of $1.6 * 10^{14}\ \frac{1}{m^2}$ for austenite at 850 °C and $4.9 * 10^{13}\ \frac{1}{m^2}$ for austenite at 1030 °C according to Equation (4), which is assumed to be a conservative approximation of the actually existing GND density (cf. Fig. 27). However, a qualitative trend for the decrease in

ρ_{GND} between austenite exhibiting the austenite memory effect at 850 °C and recrystallized austenite at 1030 °C is evident.

Shirazi et al. [50] indicated spontaneous recrystallization subsequent to the austenite memory effect in binary Fe-23Ni alloy by *ex-situ* observations. He postulated an inheritance of dislocations by a diffusionless transformation from martensite to austenite and a degradation of dislocation density in austenite exhibiting the austenite memory effect by spontaneous recrystallization. A closer related observation of spontaneous recrystallization subsequent to the austenite memory effect is reported from Shinozaki et al. [49]. Here, mechanism (IV) is claimed for the austenite memory effect and additionally spontaneous recrystallization is observed *in-situ*. Hence, a decrease of KAM inside austenite is observed during spontaneous recrystallization as it is illustrated in Fig. 21.

Results of the recent work in comparison with presented literature indicate the enhanced dislocation density of austenite exhibiting the austenite memory effect as decisive for spontaneous recrystallization.

4.2.2.2 *Ex-situ* evidence of spontaneous recrystallization

In order to validate the *in-situ* evidence of the austenite memory effect and spontaneous recrystallization on the sample surface also for bulk material and validate LAGB in austenite formed by means of the austenite memory effect, three different heat treatments are designed and conducted in a dilatometer. Subsequent to the heat treatments, the prior austenite grain size is determined and compared to the prior austenite grain size of the IAR material state. The parameter of the heat treatments are given in Table 3 in chapter 3.2.3.

Fig. 44 illustrates the prior austenite grain size before and after the different heat treatments. The comparison of the prior austenite grain size of the IAR material state with austenite grain size after heat treatment (1) at 730°C for 1h exhibits the same austenite grain size of approximately 50 µm and therefore evidences the presence of the austenite memory effect.

Heat treatment (2) at 1030 °C for 0.5 h is carried out at the same austenitization temperature (i.e. solution annealing temperature) in which the *in-situ* experiments have shown the evidence of spontaneous recrystallization (Fig. 42e and f). Here, austenite grain refinement from 50 µm to 34 µm is observed. Therefore, the results indicate spontaneous recrystallization subsequent to the austenite memory effect for solution annealing at 1030 °C also for bulk material.

In heat treatment (3), the sample is annealed in a first step at 730 °C for 1 h followed by further heating to 1030 °C followed by holding for 0.5h. After heat treatment (3) also austenite grain refinement from 50 µm to 24 µm is observed. The results indicate that the additional annealing step (730 °C for 1 h) of heat treatment (3) does not reduce the grain refinement due to spontaneous recrystallization. Therefore, it is assumed that no significant degeneration of dislocation density occurs during annealing at 730 °C, which indicates that LAGB are stable until recrystallization occurs. This observation underpins the presence of LAGB inside reversed austenite exhibiting the austenite memory effect presented in chapter 4.2.1.2.

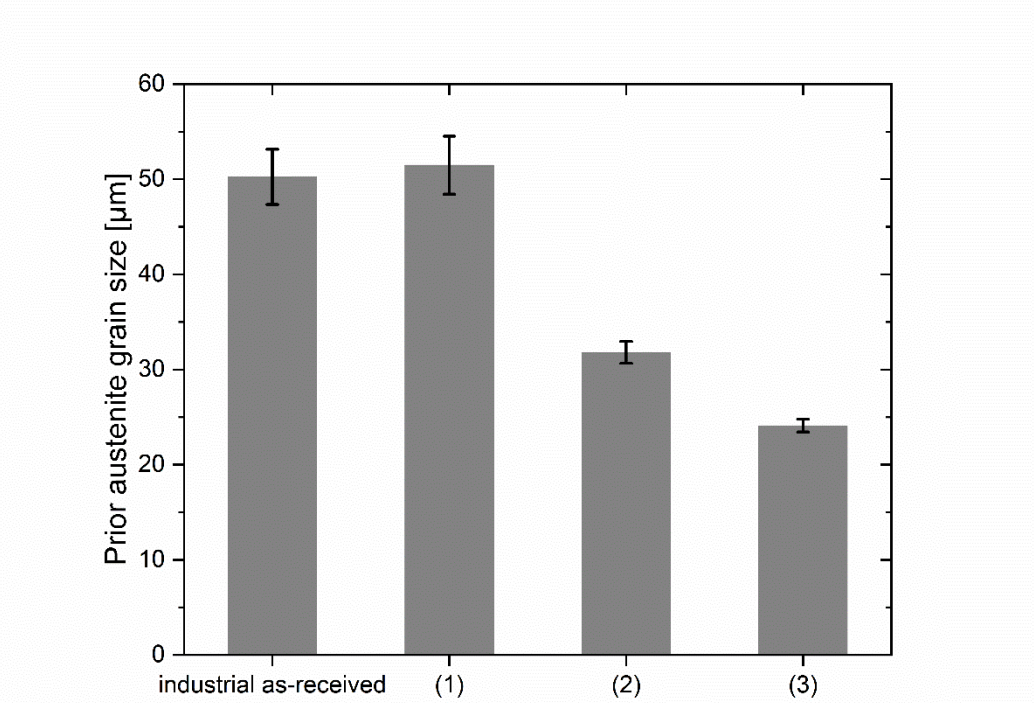

Fig. 44: Prior austenite grain size after heat treatments: 730 °C for 1 h (1), 1030 °C for 0.5 h, (2) and 730 °C for 1 h, followed by further heating to 1030 °C for 0.5 h (3) in comparison with the initial prior austenite grain size of the IAR material state. The results indicate austenite memory effect after heat treatment (1) and spontaneous recrystallization after heat treatment (2). Additionally, spontaneous recrystallization is evidenced for heat treatment (3) indicating that the dislocation density of austenite exhibiting austenite memory effect during isothermal holding at 730 °C for 1 h is approximately constant.

Differences of the prior austenite grain size after heat treatment (2) and (3) are assumed to be caused by a slight inhomogeneous initial grain size of prior austenite before the heat treatments.

The results validate the evidence of the austenite memory effect and spontaneous recrystallization for surface observations also for the bulk material.

4.2.2.3 Effect of the heating rate on austenite grain size

Heating rate variations for heating specimens up to solution annealing temperature of 1030°C are carried out in order to investigate the influence of the heating rate on spontaneous recrystallization. To this end, the prior austenite grain size was determined after the heat treatments and compared to the initial prior austenite grain size of the IAR material state.

The results of the prior austenite grain size determination, presented in Fig. 45, indicate the trend that higher heating rates lead to smaller austenite grains, i.e. stronger spontaneous recrystallization. Additionally, Fig. 46 exhibits the prior austenite grain structure after solution annealing with a heating rate of 0.033 °C/s, 3.3 °C/s and 100 °C/s. A shift from elongated austenite grains for lower heating rates to globular grains for higher heating rates can be identified.

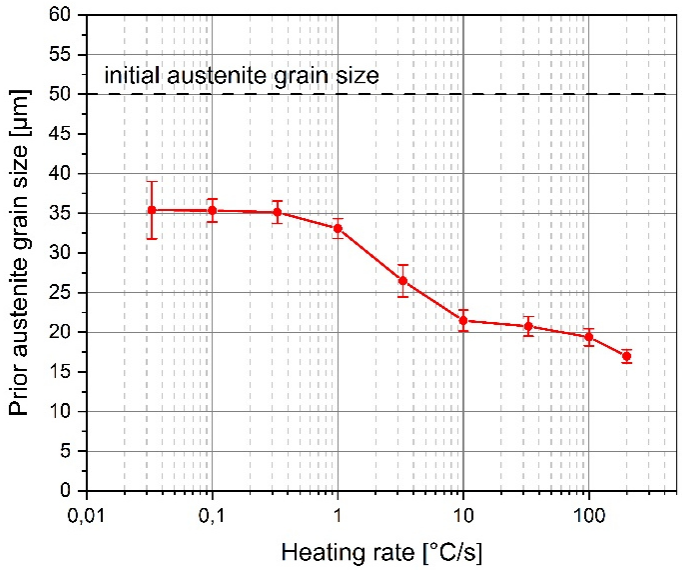

Fig. 45: Prior austenite grain size determined after solution annealing at 1030 °C for 0.5 h as function of the heating rate of the IAR material state. A stronger austenite grain refinement due to spontaneous recrystallization is observed for higher heating rates.

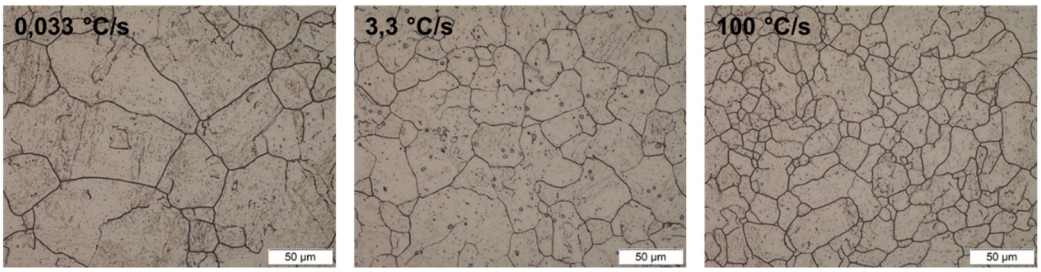

Fig. 46: Electrolytically etched prior austenite grain boundaries after solution annealing treatment at 1030 °C for 0.5 h with heating rates of 0.033 °C/s, 3.3 °C/s and 100 °C/s up to the solution annealing temperature. A shift from elongated grains to globular grains for increasing heating rate is observed.

In order to explain the effect of the heating rate up to the solution annealing temperature on the grain refinement due to spontaneous recrystallization, two approaches, both related to nucleation and growth of austenite, are discussed in the following.

In the chapters 4.2.1, 4.2.2.1 and 4.2.2.2, it is postulated that GND, inherited from martensite to austenite by the austenite memory effect, is decisive for spontaneous recrystallization. Therefore, a higher heating rate may lead to a higher nucleation rate for acicular austenite in the stage of austenite formation, by means of the austenite memory effect, thus more LAGB are inherited from martensite to austenite, i.e. higher GND in austenite. According to Equation (11) from Rios et al. [103], a higher driving force F_N for recrystallization is present for a higher dislocation density ρ. Therefore, the heating rate take influence on the driving force and may cause a stronger recrystallization, i.e. a smaller grain size. In Equation (11), G represents the shear modulus and b represents the Burgers vector.

$$F_N = G * b^2 * \rho \tag{11}$$

However, another approach suggests that nucleation of spontaneous recrystallization itself is affected by the heating rate. For this approach, a constant ρ of austenite due to the austenite memory effect is assumed for all heating rates. In this case, a higher heating rate would lead to a higher nucleation rate for spontaneous recrystallization and therefore to a smaller austenite grain size. However, the role of the heating rate on classical recrystallization is discussed controversially in literature [99]. For low heating rates, it is reported that recovery takes place previous to recrystallization and lowers the driving force for recrystallization. Although, according to Humphreys et al. [99], there is no experimental evidence for this assumption in single-phase alloys.

For other alloying compositions such as binary Fe-Ni alloys [50] and low alloyed steel [49,72], the inheritance of LAGB and its influence on spontaneous recrystallization was not investigated. Therefore, further investigations are necessary in order to confirm that higher heating rates cause a higher amount of LAGB in austenite and therefore a higher driving force for spontaneous recrystallization.

A possibility to explain the shift from elongated grains to globular grains in Fig. 46 is the assumption that the preferred nucleation sites of spontaneous recrystallization change from inside of an austenite grain for low heating rates (<0.3 °C/s) to austenite grain boundaries for higher heating rates

(>10 °C/s). Potential nucleation sites inside of an austenite grain are LAGB in austenite exhibiting austenite memory effect [1,104]. In these regions an enrichment of austenite stabilizing elements is reported especially for low heating rates [73,104]. Therefore, it is assumed that also the temperature for the start of recrystallization is lowered in these regions. An enrichment of austenite stabilizing elements on former martensite block boundaries would therefore also explain the relatively straight grain boundaries of austenite in Fig. 46 for a heating rate of 0.03 °C/s, as recrystallization would start along these regions. However, such enrichment of austenite stabilizing elements on martensite block boundaries is not investigated in literature up to now. For higher heating rates, additionally austenite grain boundaries are assumed to act as nucleation site for spontaneous recrystallization. Consequently, a higher number in nucleation sites would cause an earlier impingement of neighboring grains and a more globular austenite grain structure.

This assumption is in accordance to the *in-situ* observation of spontaneous recrystallization by Shinozaki et al. [49] illustrated in Fig. 21. Here, spontaneous recrystallization is not finished and austenite grain boundaries seem to act as nucleation sites for spontaneous recrystallization. According to Shinozaki et al. [49], pre-existing globular austenite on austenite grain boundaries grows during spontaneous recrystallization. It is assumed that an akin mechanism acts also in the PH 15-5 alloy investigated in this work. However, no globular austenite is detected in the high temperature *in-situ* EBSD measurements (Fig. 42) and therefore no differentiation between globular austenite and spontaneous recrystallization can be carried out.

However, in order to identify the nucleation sites of spontaneous recrystallization, further *in-situ* high temperature EBSD measurements have to be conducted in which the recrystallization is incomplete.

4.2.2.4 Effect of repeated solution annealing on grain size

In order to identify a threshold for grain refinement due to spontaneous recrystallization during solution annealing, a variation of the number of solution annealing cycles is carried out and the prior austenite grain size is determined.

Fig. 47 illustrates, that the austenite grain size decreases in the first two cycles and stay constant when the number of cycles is further increased with a heating rate of 2 °C/s. After every solution annealing cycle the sample is cooled to room temperature. The threshold of the prior austenite grain size is approximately 20 µm, which is in the same range as the observed plateau for the heating rate variation (Fig. 45). This fact indicates an equilibrium

between austenite grain refinement due to spontaneous recrystallization and austenite grain growth for solution annealing at 1030 °C for 0.5 h.

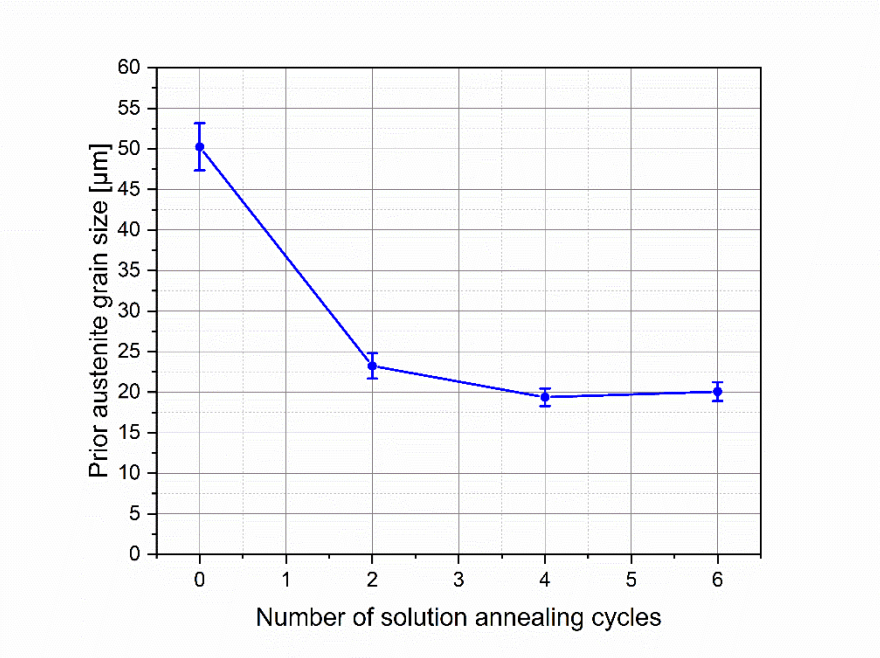

Fig. 47: Prior austenite grain size as function of the number of solution annealing cycles at 1030 °C for 0.5 h with a heating rate of 2 °C/s. The same plateau for austenite grain refinement is observed as for the heating rate variation (Fig. 45) indicating an equilibrium between grain refinement and grain growth for the applied solution annealing.

The austenite grain morphology after 2, 4 and 6 solution annealing cycles is illustrated in Fig. 48, whereby no significant difference is observable. In comparison with the austenite grain morphology after solution annealing with 3.3 °C/s heating rate up to austenitization temperature in Fig. 46, the austenite grains appear more globular. This may be attributed to the austenite grain refinement after the first solution annealing cycle. Thus, a finer austenite grain size is the initial grain size for the second solution annealing cycle and so forth. This observation is an indication that austenite grain boundaries are acting as nucleation sites for spontaneous recrystallization as more austenite grain boundaries are present as nucleation sites for spontaneous recrystallization and a more globular grain is observed.

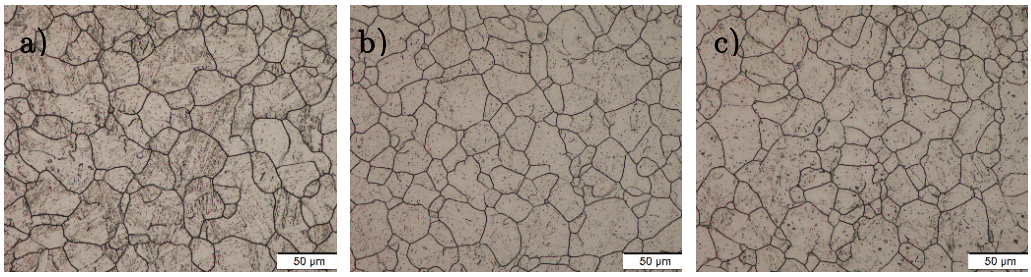

Fig. 48: Electrolytic etching of prior austenite grain boundaries after 2 (a), 4 (b) and 6 (c) solution annealing cycles at 1030 °C for 0.5 h with a heating rate of 2 °C/s. A globular structure of prior austenite grains is visible for all states.

4.2.3 Martensitic transformation

The following chapter is dedicated to the martensitic transformation during cooling from solution annealing temperature to room temperature. Therefore, this is an essential process step for the development of the martensitic substructure of the final component. The martensitic transformation is investigated in terms of spatially resolved transformation progress, martensite block size development and accompanying increase of austenite / martensite strength.

4.2.3.1 *In-situ* observation of martensite formation

In order to correlate the spatially resolved progress of martensite formation with prior austenite grain size, an *in-situ* observation by HT-CLSM is conducted during cooling from solution annealing temperature of the IAR material state.

Single frames of the transformation sequence are illustrated in Fig. 49 corresponding to different temperatures and exhibiting a thermal etching of austenite grain boundaries. The martensite start temperature is determined at 121.0 °C by the first observation of a surface relief induced by the martensitic transformation. This is in good agreement for M_S determined by dilatometry of the IAR material state after solution annealing at 1030 °C for 30 min. Here, M_S is determined at 110 °C. In literature it is reported that M_S measured by HT-CLSM at a free surface is higher than M_S measured by dilatometry of the bulk material [105]. Therefore, the temperature measurement of HT-CLSM and consequently the determined M_S is plausible.

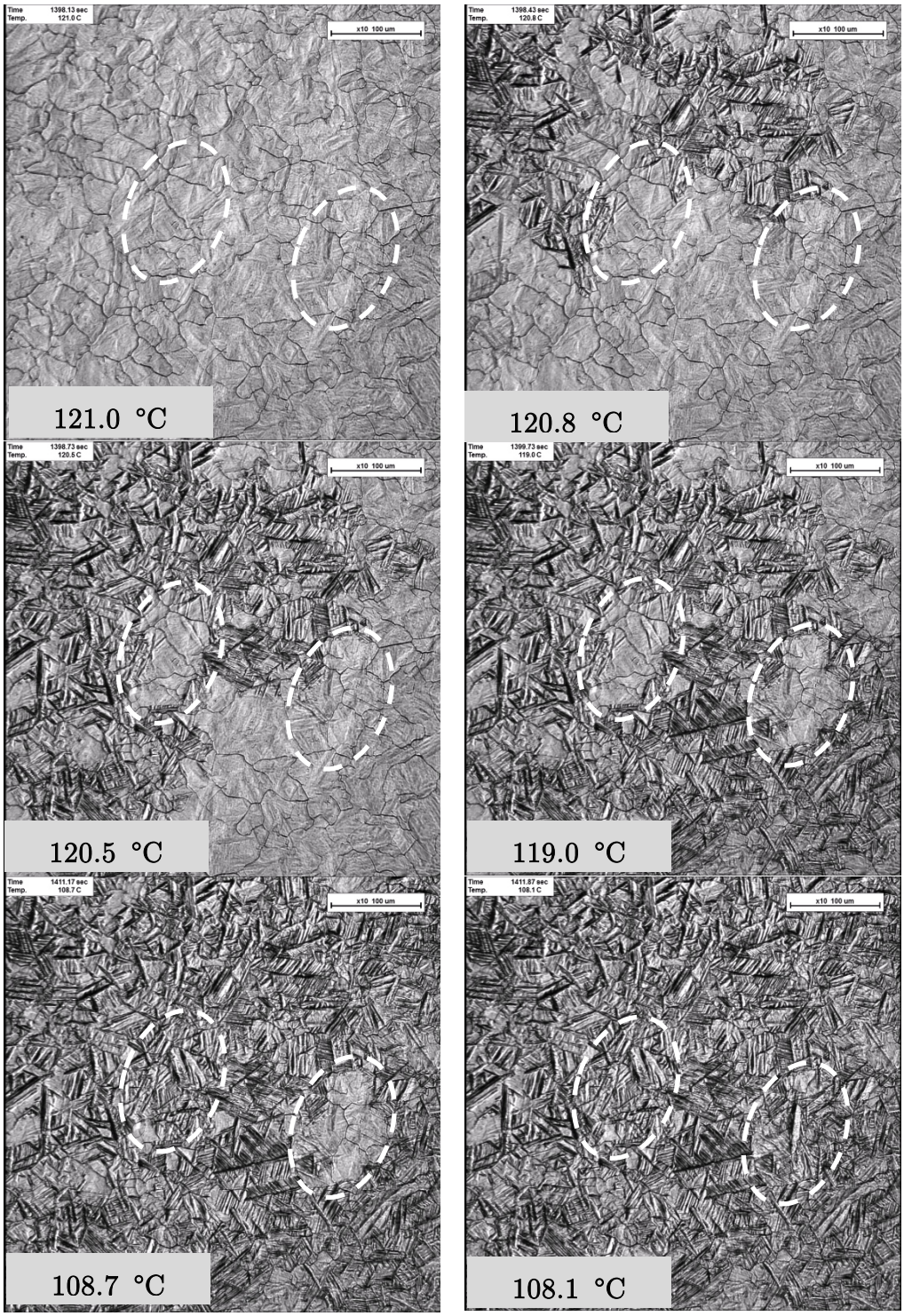

Fig. 49: In-situ HT-CLSM observation of martensite transformation after solution annealing at 1030 °C for 10 min. The figure illustrates the first transformation sequence between 121.0 °C and 108.1 °C. However, the martensite transformation is not completed at 108.1 °C. Regions with retarded transformation are highlighted with white dashed lines, exhibiting no differences in austenite grain size. Therefore, segregation is assumed to cause more stable regions of austenite and retard the martensitic transformation.

A cascade-like transformation sequence is observed beginning at the upper left region of the sample surface and propagates to the lower right region whereat isolated areas remaining untransformed (highlighted with white dashed lines). This global transformation progress is indicating a temperature gradient within the observed area and impedes a correlation with austenite grain size. However, the untransformed regions exhibiting a similar austenite grain size as the surrounding area. Therefore, locally different composition due to segregation is assumed to retard the transformation locally and is in this observation more decisive for martensitic transformation than the differences in austenite grain sizes.

According to literature, the austenite strength significantly affects the martensitic substructure such as block size, which is presented in chapter 2.1.2. The isolated untransformed regions, highlighted in Fig. 49, undergo a compression due to the transformation induced volume increase of surrounding martensite and therefore the strength of austenite tend to increase and further retard the transformation additional to chemical differences due to segregation. According to literature, this strengthening of austenite leads also to a finer martensite substructure as it is discussed in chapter 2.1.2. This cannot be observed by the conducted HT-CLSM measurement. Therefore, high temperature *in-situ* EBSD in carried out in order to quantify the development of martensite block size. The results are presented in the following chapter.

4.2.3.2 Development of martensite block size

In order to quantify the development of martensite block size during the progress of the martensitic transformation, *in-situ* EBSD measurements subsequent to solution annealing are carried out on the same sample position where austenite formed by the austenite memory effect and subsequent spontaneous recrystallization were observed.

The progress of martensite transformation is illustrated in Fig. 50 by phase information (red = martensite, green = austenite) with an overlap of IQ in order to visualize the martensitic microstructure.

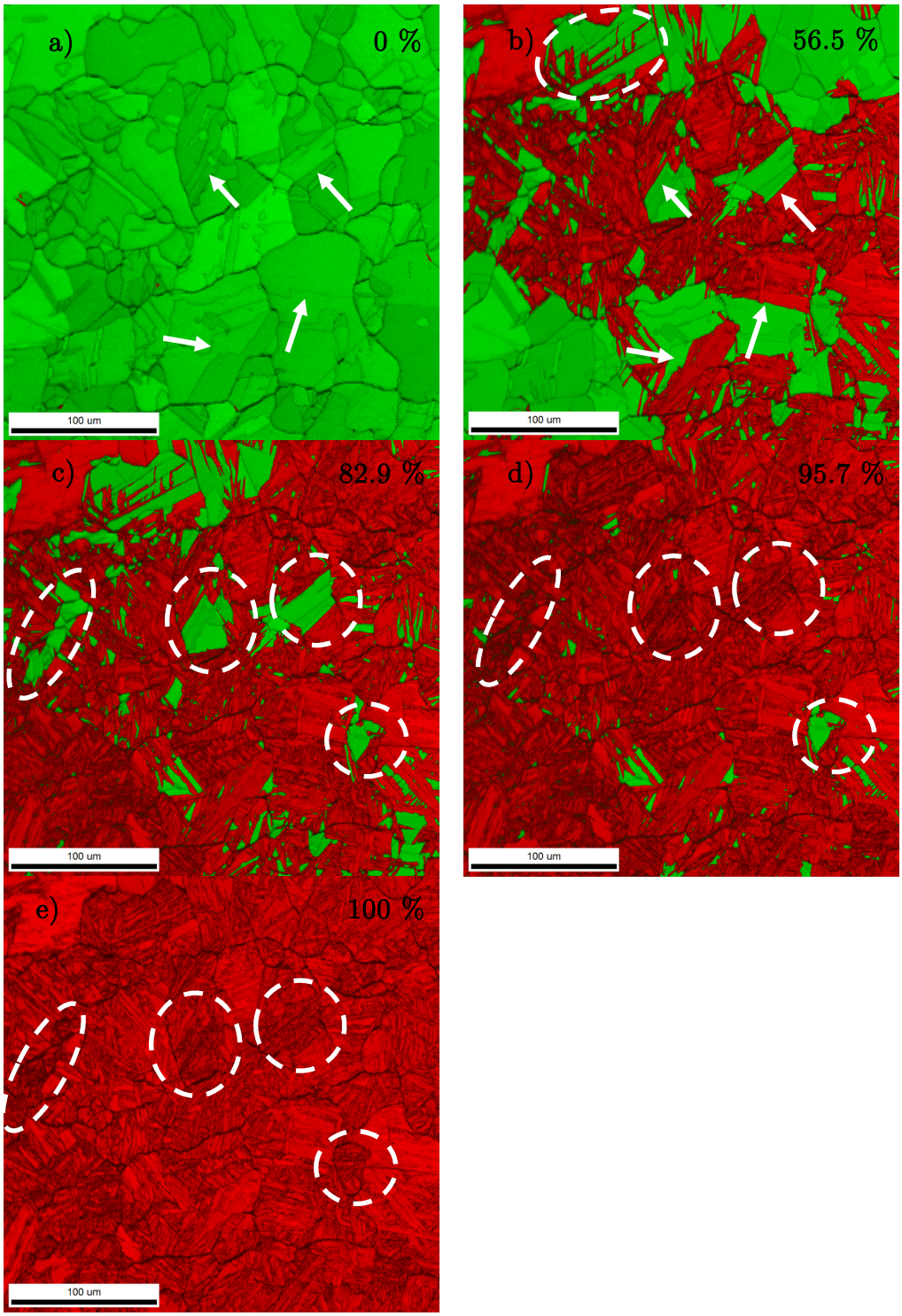

Fig. 50: High temperature in-situ EBSD observation of martensite transformation during cooling after solution annealing at 1030 °C for 10 min with phase information and overlapped IQ color coding. Initial austenite microstructure at 1030 °C is illustrated in a) and then the increasing martensite phase fraction is given in b) to e). Austenite twin boundaries, highlighted in a) and b) by white arrows, act as borders between transformed and non-transformed regions and therefore validate the austenite twin size as effective grain size for martensitic transformation. Isolated untransformed areas, surrounded by martensite are highlighted by dashed white lines (c - e) and transforming retarded with finer martensite substructure.

Fig. 50a and b illustrate the first transformation sequence from austenite to martensite with white arrows highlighting austenite twin boundaries. These twin boundaries act, in addition to austenite grain boundaries, as borders between transformed and non-transformed regions. This observation validates the findings of chapter 4.1.1 that the austenite twin size is acting as effective grain size for the martensitic transformation. Furthermore, this is in accordance with observations of Nambu et al. [56], identifying coherent twin boundaries as potential nucleation site for the first forming martensite variants. He further postulated that the first forming variants are chosen in a way to minimize the total shear component of the transformation and partitioning the austenite grain. In Fig. 50b, the first forming variants in an austenite grain are nucleating at coherent twin boundaries (highlighted with dashed lines) indicated by the straight morphology [99]. Therefore, the high temperature *in-situ* EBSD measurement indicates coherent twin boundaries in PH 15-5 as potential nucleation site for the first forming martensite variants.

First forming martensite variants are influencing the subsequent forming variants by plastic deformation at the martensite / austenite interface, which further induce elastic strain in austenite [13,14,39]. This influences the martensite variants that are formed subsequently and additionally can cause compressive stresses inside isolated areas such as highlighted in Fig. 50c - e. These isolated untransformed regions are similar to those observed by HT-CLSM (Fig. 49). A finer martensite microstructure is present in isolated regions indicated by the IQ information and highlighted in Fig. 50c - e with dashes lines.

Out of the data of Fig. 50, a quantitative evaluation of the mean martensite block size as a function of martensite phase fraction is shown in Fig. 51. Therefore, the mean martensite block size of the martensitic phase of Fig. 50b - e is calculated. Both evaluation methods, number fraction and area fraction, exhibit the same trend; the higher the martensite phase fraction becomes the smaller the becomes also the martensite block size. It can be stated that the first formed martensite blocks are coarser than the following ones, which is in accordance to *in-situ* observations of lath martensite formation of Nambu et al. [56]. Taking findings from literature as summarized in chapter 2.1.2 into account, the decreasing martensite block size indicates a strengthening of austenite with propagating martensite formation which is also indicating plastic straining of the austenite. However, also Hall-Petch strengthening of austenite due to partitioning of the austenite grain by the

forming martensite variants can contribute to the total austenite strength [14].

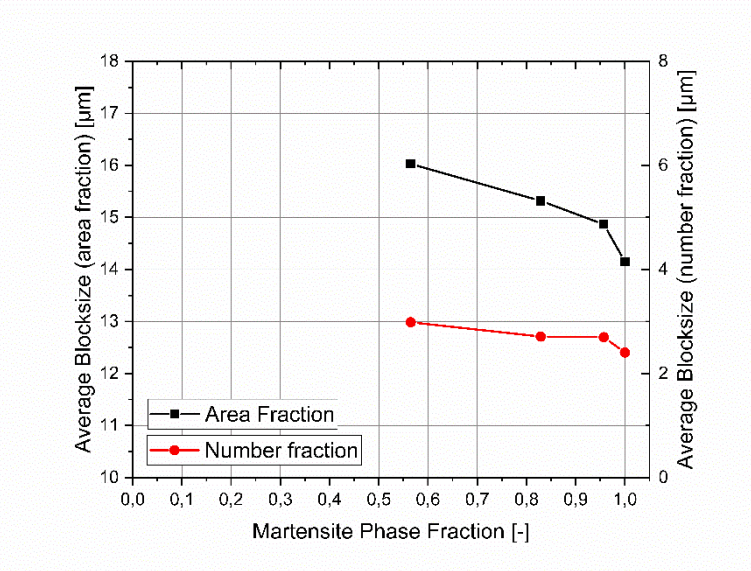

Fig. 51: Average martensite block size visualized as area fraction (black) and as number fraction (red) as function of the phase fraction of martensite calculated from EBSD data of Fig. 50. With increasing martensite phase fraction, a decrease of the mean block size is observable.

In order to verify the increase of defect density, as indicated by GND, with propagating martensite formation, the KAM is calculated and the spatial distribution over the sample surface is shown in Fig. 52 for martensite (left: a, c, e, g) and austenite (right: b, d, f).

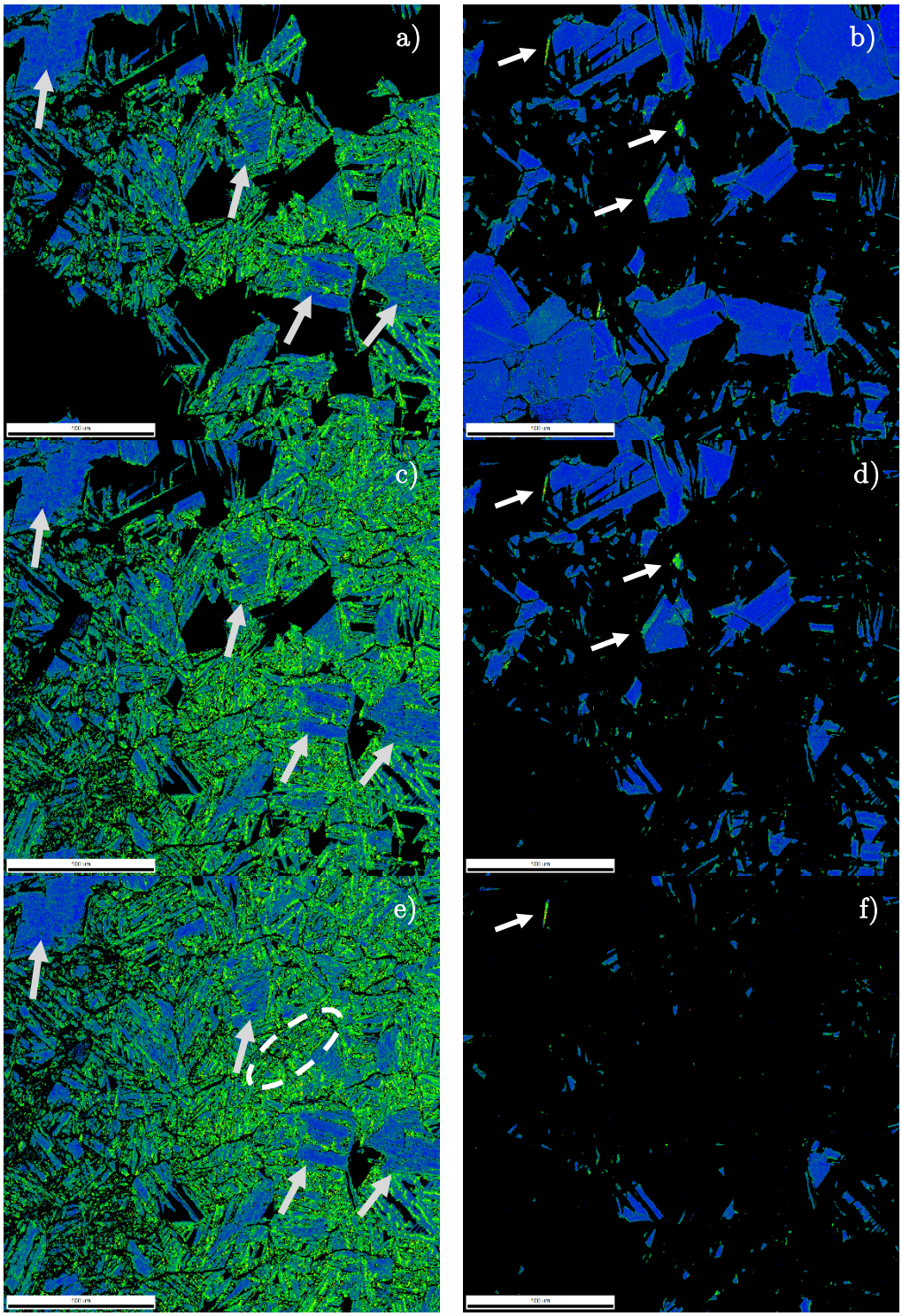
a)
b)
c)
d)
e)
f)

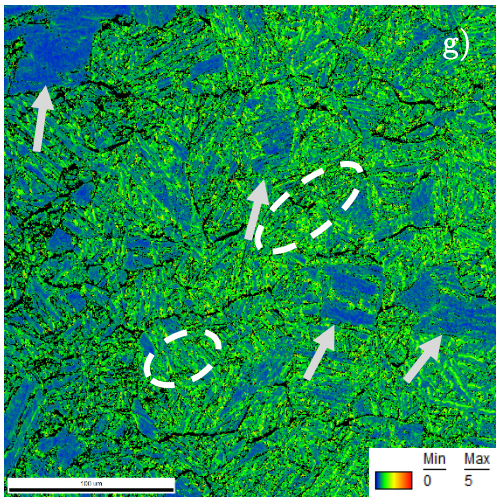

Fig. 52: In-situ measurement of spatial distribution of KAM for martensite (a, c, e, g) and austenite (b, d, f) calculated from the EBSD data shown in Fig. 50. The color code ranges from blue for 0° KAM to red for 5° KAM. The black color represents regions with CI < 0.2 and are therefore excluded. In martensite, the first forming blocks (indicated by grey arrows) exhibit a lower and more homogeneous KAM than the blocks formed in the later stages (indicated by white dashed lines). In austenite, only very small, isolated regions show an increase in KAM indicated by white arrows.

The first forming martensite blocks, indicated in Fig. 52a with grey arrows, exhibit areas with a lower and more homogeneous KAM than the later forming blocks as indicated by the blue color (Fig. 52c, e, g). The lower KAM in these areas may be attributed to the lower amount of block boundaries of the relatively large martensite blocks forming first. The relative homogeneous IQ of these regions in Fig. 50 confirms the large block size. Therefore, it can be stated that the first forming blocks exhibiting not only a larger block size but also a lower KAM and thus a lower amount of GND. The enhanced KAM values of martensite / austenite phase boundary regions indicate a local plastic deformation, see [106], which is caused by the martensitic transformation and is in accordance with literature [13]. However, the step size of the EBSD measurement of 1 µm for Fig. 52a - f was relatively large and therefore it is assumed that the real KAM of these regions tend to be larger than the measured values. Plastic deformation is also observable in the austenite phase. Fig. 52b, d, f exhibit an enhanced KAM value in the austenite near the martensite/austenite phase boundary regions. In small isolated regions, highlighted by white arrows, the highest KAM values are observable. The rest of the austenitic phase exhibits a low and homogenous KAM. This suggests that especially boundary regions of the adjacent austenite undergo a plastic deformation due to the martensitic transformation whereby the inner region of untransformed austenite exhibiting elastic stress fields that cannot be resolved by KAM but may contribute to the self-accommodation process described in chapter 2.1.2.

A calculation of the mean KAM value for each transformation step of Fig. 52 is given in Fig. 53 indicating an increase with propagating transformation for martensite and austenite. Especially, the last transformation step of the martensitic phase causes a strong increase in the mean KAM value. The results show an increase in GND with propagating transformation and therefore validate the assumption of increasing austenite strength with propagating transformation leading to a smaller martensite block size.

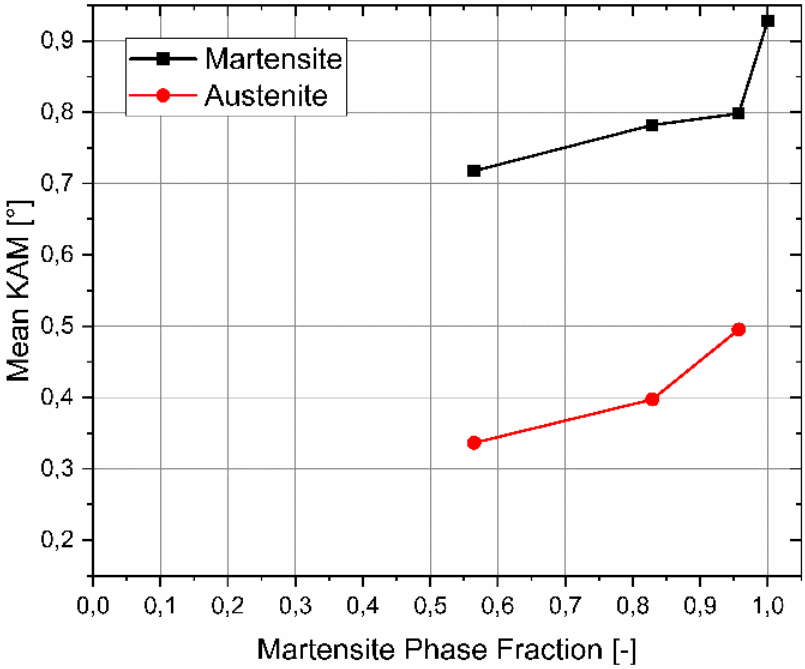

Fig. 53: Mean KAM of martensite (black) and austenite (red) calculated from Fig. 52 as function of the phase fraction of martensite. The mean KAM increases for propagating martensite formation in martensite and austenite indicating an increase in the mean GND value of a block or isolated austenite regions.

4.2.4 Summary of microstructure development during solution annealing

This thesis reveals that the austenitization during solution annealing of PH 15-5 is divided into two stages: stage 1 is the formation of austenite based on the austenite memory effect, followed by stage 2 which is the spontaneous recrystallization.

It is postulated that austenite memory effect is based on the variant restriction between martensite laths and reversed austenite influenced by an internal stress field (mechanism IV in chapter 2.2.1). This effect is connected

with the inheritance of LAGB from martensite to austenite and therefore increases the GND in austenite exhibiting austenite memory effect. During further heating after the formation of austenite based on the austenite memory effect, the increased ρ_{GND} might be reduced by spontaneous recrystallization and a new austenite grain structure is formed, comparable to classical recrystallization but without external deformation. Austenite grain boundaries are assumed to be the most probable nucleation site for spontaneous recrystallization. Furthermore, a heating rate dependence of the austenite grain size due to spontaneous recrystallization underpin the assumption of a nucleation and growth process for spontaneous recrystallization. A plateau value for austenite grain size of 20 µm due to spontaneous recrystallization during the standard solution annealing at 1030 °C for 0.5 h and high heating rates (>10 °C/s) is determined. A variation of the solution annealing cycle number also lead to the same plateau indicating an equilibrium between grain refinement and grain coarsening during the standard solution annealing.

From freshly recrystallized austenite grain structure, martensite forms subsequently during cooling to room temperature. A direct influence of the austenite grain size concerning the first formed martensite variants cannot be observed but it can be stated that austenite twin boundaries act as nucleation sites for martensite. The developing martensite encloses isolated areas of austenite in which the transformation to martensite is somehow retarded. It is assumed that such structures are caused by a segregation pattern in the PH 15-5 steel. High temperature *in-situ* EBSD measurements indicate that larger martensite blocks with a lower amount of GND are formed first, the subsequently formed martensite blocks become smaller with increasing martensite fraction. Investigations of the KAM and consequently GND in the austenitic phase reveal enhanced ρ_{GND} and therefore plastification mainly at the phase boundaries to martensite. Statements about the elastic stress field in austenite induced by the martensitic transformation therefore cannot be proposed because of the dominance of the plasticization but have to be considered in further investigations.

4.3 Influence of the austenite state on martensitic microstructure

In the following chapter, the influence of the austenite state, such as grain size and deformation texture, on the evolving martensitic microstructure is investigated. Therefore, block size and martensite variant distribution of the material states IAR, AS and CG are compared. In the IAR material state, a slight microstructural deformation texture similar to the EAR material state can be found. After solution annealing the austenite grain structure is refined due to spontaneous recrystallization and therefore AS is assumed to exhibit a smaller austenite grain size compared to IAR. The CG material state is assumed to exhibit a larger prior austenite grain size because of controlled grain growth and therefore is compared to the IAR and AS material states.

4.3.1 Martensite block size

In order to investigate the influence of the austenite state on the evolving martensite block size, EBSD measurements of the 3 different material states IAR, AS and CG are conducted. The EBSD data is presented in Fig. 54 with IPF color-coding.

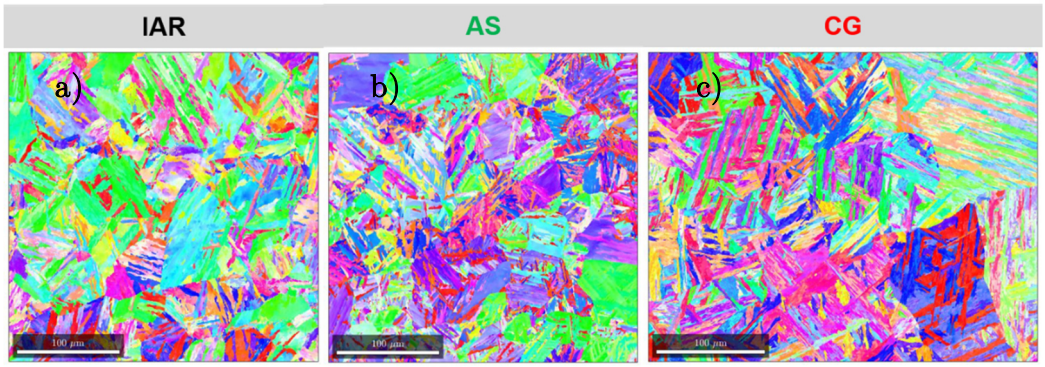

Fig. 54: IPF of the martensitic microstructure of the material states IAR (a), AS (b) and CG (c). According to the martensitic microstructure, a difference of the prior austenite grain size can be assumed.

With the generated EBSD data, the OR of each material state is evaluated and the prior austenite grains are reconstructed with the algorithm of Nyyssönen et al. [46]. The angular deviation of the calculated OR from KS OR is illustrated in Table 4. Therefore, the angular deviations between the closed packed planes ($\{111\}_{\gamma}$ and $\{011\}_{\alpha'}$) and closed packed directions ($\langle 011\rangle_{\gamma}$ and $\langle 111\rangle_{\alpha'}$) of austenite and martensite are given. These angles are zero for an ideal KS OR (cf. chapter 2.1.1.1).

Table 4: Deviation of the calculated OR from KS OR by indicating the angles between the closed packed planes and closed packed directions in austenite (γ) and martensite (α′) for the material states IAR, AS and CG. These angles validate a deviation of the calculated OR from idedal KS OR.

Deviation	IAR	AS	CG
$\{111\}_{\gamma}$ from $\{011\}_{\alpha'}$	2.7°	1.8°	2.8°
$\langle 011\rangle_{\gamma}$ from $\langle 111\rangle_{\alpha'}$	1.7°	1.2°	1.7°

All calculated OR of the presented material states exhibit an angular deviation from KS OR. Although, the IAR and CG material state exhibit a similar OR, the AS material state is closer to KS OR. Further investigations are necessary in order to understand such behavior and the influence of the austenitic microstructure on the present OR of martensite and austenite.

Furthermore, the effective prior austenite grain size is determined. Fig. 55 illustrates the result of the reconstruction in IPF color coding and prior austenite grain and twin boundaries drawn in black.

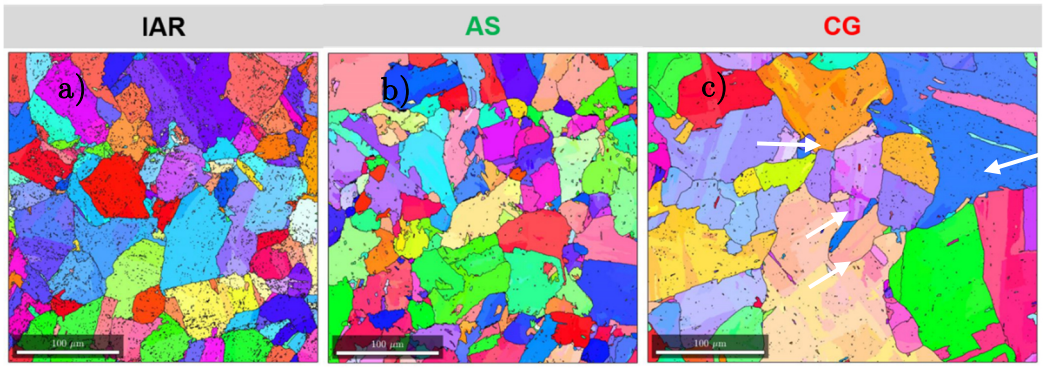

Fig. 55: IPF color coding of the prior austenite reconstruction with prior austenite grain boundaries drawn in black for the material states: IAR (a), AS (b) and CG (c). A clear difference of the prior austenite grain size is observable.

Different effective prior austenite grain sizes are determined with 27 µm for IAR, 19 µm for AS and 39 µm for CG material state. The effective prior austenite grain size of the IAR material state is in good agreement with the effective prior austenite grain size determined for the EAR material state with 28 µm. In addition, a strong twin formation is found in the IAR material state similar to the EAR material state. These factors verify that the forging parameter of the EAR material state are similar to those of IAR.

In the reconstruction of the CG material state in Fig. 55, not only coarse grains but alsofine grains are present (highlighted with white arrows). The finer grain population show a more globular structure and is located at prior

austenite grain boundaries of the larger grain population. This may be attributed to the spontaneous recrystallization during solution annealing subsequently to the coarse grain annealing. Therefore, this observation again points towards prior austenite grain boundaries as nucleation sites for spontaneous recrystallization as it is postulated in chapter 4.2.2.3. However, a larger prior austenite grain size may therefore impede spontaneous recrystallization but such behavior is not experimentally verified in this work and is mentioned in the outlook on further research in chapter 0.

Based on the calculation of the OR of the specific material states, a martensite block boundary angle is determined in the same way as it is presented in chapter 4.1.2.1 of the work. The block boundary angles are 5.68° for IAR, 7.24° for AS and 5.51° for CG material state. These block boundaries are drawn with black lines in IPF color coding of the different material states in Fig. 56.

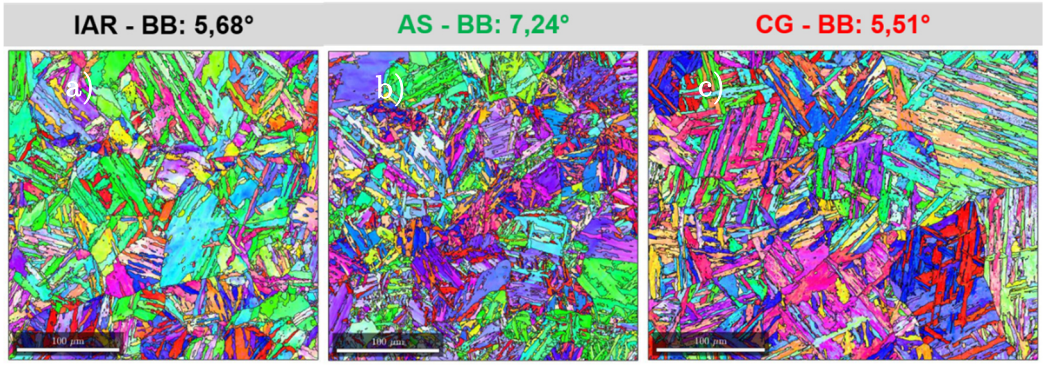

Fig. 56: IPF color coding with martensite block boundaries drawn in black for the material states: IAR (a), AS (b) and CG (c). BB is here meant as the block boundary angle. Despite a larger block boundary angle of the AS material state, the martensite block structure appears finer compared to the other material states.

Based on these results, the distribution of the martensite block size according to number fraction and area fraction can be calculated and is illustrated in Fig. 57. All material states exhibit similar distributions of the number fraction, as each maximum is at the smallest detectable block size, and similar distributions of area fractions, as each distribution exhibits a local maximum that is larger than the smallest detectable block size. However, the material states are comparable due to the same smallest detectable block size, described in chapter 3.2.1.2. Additionally, the mean martensite block size can be determined for each material state according to number and area fraction and is illustrated in Fig. 58.

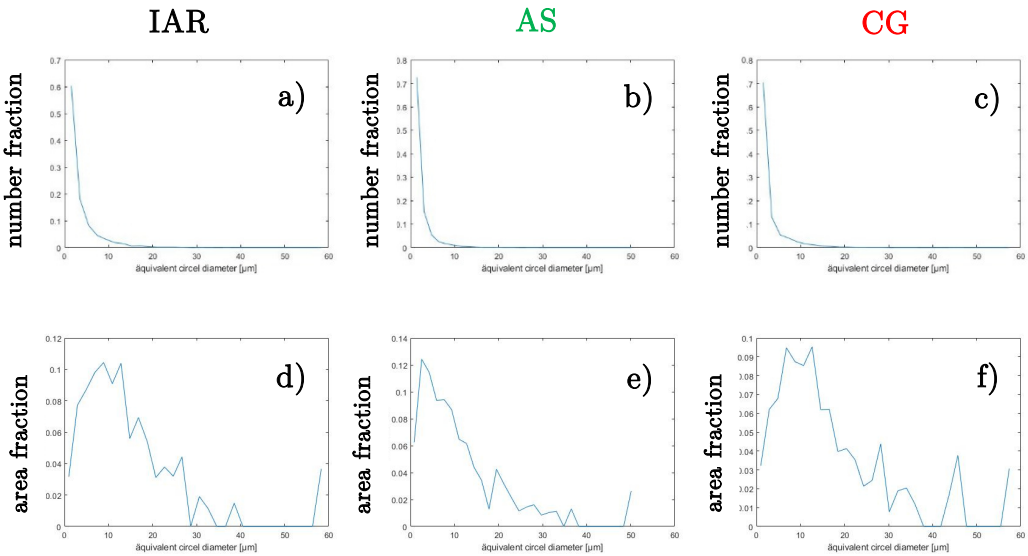

Fig. 57: Distribution of the martensite block size (äquivalent circle diameter) according to number fraction and area fraction of the material states IAR (a,d), AS (b,e) and CG (c,f). The evaluation of number fraction is sensitive to the smallest detectable block size as the maximum of each distribution is at the minimum.

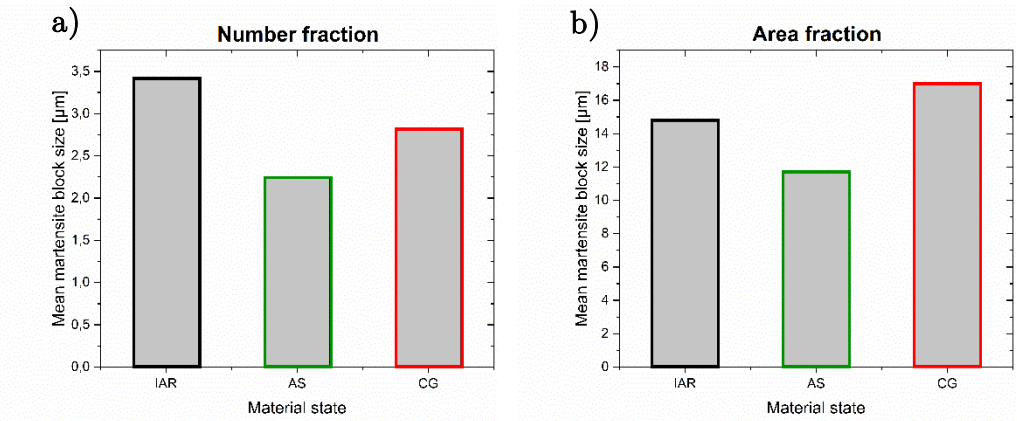

Fig. 58: Mean martensite block size of the investigated material states IAR, AS and CG evaluated with number fraction (a) and area fraction (b). The AS material state exhibit the smallest martensite block size underpinning the influence of effective prior austenite grain size. CG exhibits a finer block size according to number fraction as the IAR material state. Therefore, some other influences on the block size additionally to the effective prior austenite grain size have to be present.

A comparison between IAR and AS exhibit a smaller martensite block size for a smaller effective austenite grain size according to number fraction and area fraction. This is in accordance with many other observations of martensite block size and the classical interpretation of the influence of the prior austenite strength on the martensitic substructure presented in chapter 2.1.2. Comparing the IAR with the CG material states, a larger effective prior austenite grain size leads to a larger martensite block size according to area fraction. For the determination of the mean block size with area fraction,

large blocks are stronger valued compared to a determination with number fraction.

In combination with results of the previous chapter 4.2.3.2, where it is shown that first forming martensite blocks are larger, the present results indicate that first formed martensite blocks forming in coarse prior austenite twins are larger compared to those forming in finer austenite twins. However, a controversial observation is the lower martensite block size according to number fraction of the CG material state in comparison to IAR. This result indicates that a larger effective prior austenite grain size can lead to a smaller martensite block size, accounted to the total number of martensite blocks. Therefore, after the formation of large first martensite blocks, the subsequent forming blocks are smaller in CG material state than in the IAR. This behavior is not explainable by the prior austenite strength as only influencing parameter for the martensite block size. Therefore, the martensite variant distribution is investigated as possible influencing parameter in the following chapter.

4.3.2 Martensite variant distribution

Additionally to the determination of the martensite block size, a variant distribution was calculated for the presented material states in order to investigate possible reasons for the smaller martensite block size of the CG material state in comparison the IAR material state according to number fraction.

The martensite variant distributions for the different material states are illustrated in Fig. 59. The horizontal dashed line inside each histogram represents an ideal number fraction of 1/24 for an equal distribution of all variants. Variants, blocks or packets exceeding this line are indicated as preferred.

The variants 13 to 18 of the IAR material state exceed the equal distribution line and therefore exhibit a preferred packet P3. This is consistent with the variant distribution of the EAR material state, presented in chapter 4.1.2.2. However, in the EAR variant distribution additionally packet P4 is formed preferred. According to Miyamoto et al. [35], the amount of deformation of austenite previous to martensite transformation determines the preference of packets, as it is illustrated in Fig. 10. He observed that two packets are preferentially formed for deformation higher than 30 %. Therefore, the results of variant distribution indicate a higher amount of deformation in austenite of the EAR material state (chapter 4.1.2.2) in comparison with the IAR material state. However, a quantitative approximation

about the difference in the amount of deformation cannot be given because of the different alloy composition used by Miyamoto et al. [35].

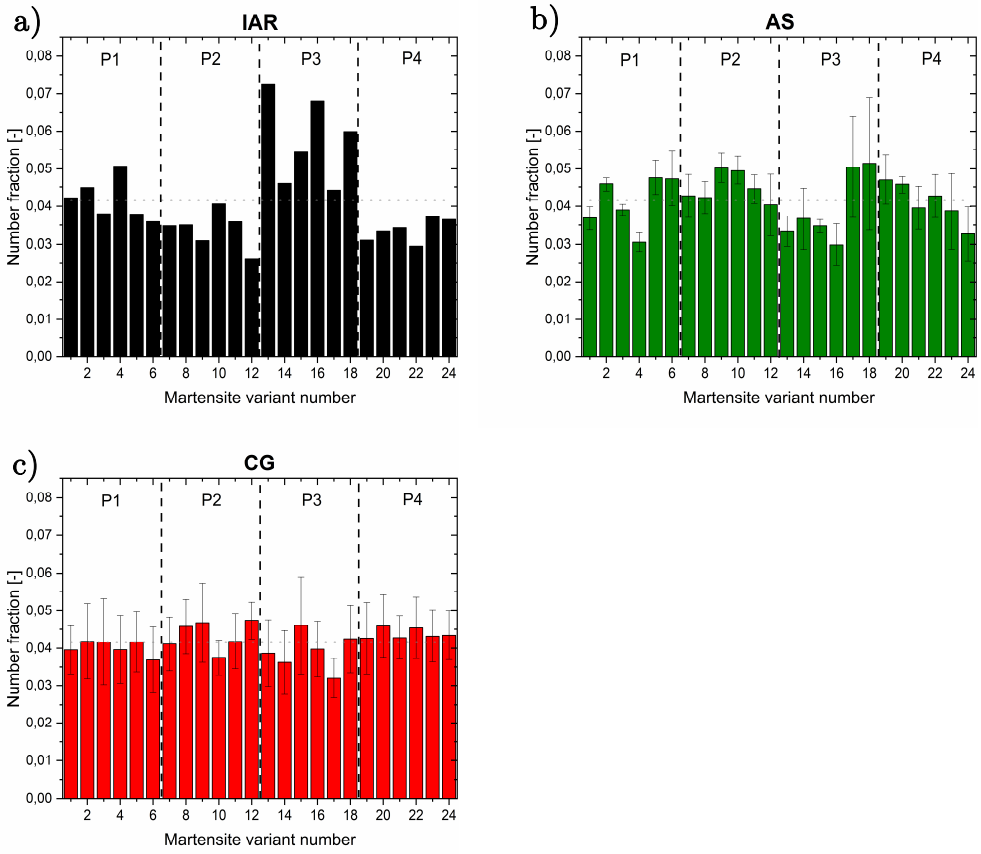

Fig. 59: Comparison of martensite variant distribution of the investigated material states IAR (a), AS (b) and CG (c). Each material state exhibiting a different distribution of martensite variants. IAR reveals a preferred packet P3, which is similar to observations of the EAR material state. The variant distribution of the AS material state is exhibiting a more random distribution whereas the CG material state exhibits the most homogeneous variant distribution. The error bars in (b) and (c) represent the standard deviation of 3 quantitative martensite variant distributions out of 3 EBSD measurements.

The AS material state (Fig. 59b) exhibits a completely different appearance of the variant distribution compared to IAR (Fig. 59a), in which no whole packet is preferred. Additionally, not the same blocks (i.e. variants that sharing the same Bain axis) are preferred inside the packets P1 to P4. Therefore, the histogram of the AS material state in Fig. 59b gives the impression of a random distribution. According to Furuhara et al. [13,14,65], the austenite grain size takes influence on the number of formed blocks and packets. In literature it is assumed, that shear stress compensation cannot proceed within a single austenite grain when the austenite grain size gets too small and therefore the surrounding austenite grains and grain boundaries are involved in compensating the transformation induced shear stress

[14,107]. Hence, the surrounding austenite grains cause martensite variants that compensate the total shear stress and therefore not every variant inside one grain is produced. This is in accordance to the observation of the more homogeneous variant distribution of the CG material state. In order to quantify the deviation of the variant distribution, the mean deviation of each martensitic variant from the equal distribution line $\bar{f}$ is calculated using Equation (12) with f_i for the number fraction of each variant ranging from 1 to 24. For the CG and AS material state, f_i represents the mean values out of 3 quantitative martensite variant distributions per material state.

$$\bar{f} = \frac{\sum_{i=1}^{24} \left| f_i - \frac{1}{24} \right|}{24} \tag{12}$$

The CG material state exhibits the smallest $\bar{f}$ with 0.0028 compared to 0.0090 for IAR and 0.0055 for AS material state. Therefore, $\bar{f}$ of the CG material state is only 51 % from $\bar{f}$ of the AS material state. This supports the impression of the homogeneous martensite variant distribution of the CG material state and it is also in accordance with literature which states that the austenite grain size influences the martensite variant distribution [13,14].

It is assumed that only a little temperature gradient was present during the formation of martensite in the AS material state because of the stepped cooling during martensite formation (cf. Fig. 29) and the small sample size of about 5x6x0.5 mm³. Therefore, an influence of thermal residual stresses on the martensite variant distribution is excluded.

However, to the knowledge of the author, no quantitative correlation between effective austenite grain size, martensite block size and martensite variant distribution was investigated before. It is assumed that the range of the elastic stress field produced by the first forming variants determines whether the shear compensation takes place within one grain or over a group of neighboring grains. Therefore, the range of the elastic stress field would be a characteristic length for a specific material state and in comparison with the effective prior austenite grain size, predictions about the martensite variant distribution should be possible.

The effective austenite grain size of the AS material state is approximately the half of the CG material state. Therefore, approximately 4 times more austenite grains are observed inside the whole EBSD measurement area of 0.27 mm² (i.e. 3x300x300 µm²). Despite the higher number of austenite grains in the EBSD measurement, the martensite variant distribution is not

homogeneous in the AS material state as it can be seen in Fig. 59b. Therefore, it is assumed that the range of the elastic stress field induced by the first forming martensite variants exceeds the neighboring austenite grains and a larger measurement area is necessary in order to obtain a homogenous distribution of martensitic variants for the AS material state.

However, the actual work indicates an interrelation of the effective prior austenite grain size, the martensite variant distribution and the martensite block size that has not been postulated up to now. The determination of a characteristic length of the elastic stress field has not been investigated in the present work and is part of further research.

5 Short summary of the main results

In the present work, the microstructural development of austenite and martensite during solution annealing is investigated for the as-received material state of the commercial alloy PH 15-5. Additionally, the influence of the austenite state (i.e. effective grain size and dislocation density of austenite) on the subsequently developing martensite substructure is investigated on the example of three different materials states: Industrial as-received (IAR), after solution annealing (AS) and coarse grain CG. IAR material state exhibits an effective austenite grain size of 27 µm and a slightly enhanced dislocation density of austenite is expected because of previous hot deformation. The material states AS and CG exhibit an effective austenite grain size of 19 µm and 39 µm, respectively, and no hot deformation during the last solution annealing is applied.

The reconstruction of the prior austenite grain structure from martensite of the EAR material state evidences a strong annealing twin formation of austenite during forging, which may be attributed to the low stacking fault energy of PH 15-5. Furthermore, these annealing twins in austenite act as parent grain for the martensitic transformation. Therefore, the austenite twin size (i.e. the austenite grain with consideration of twin boundaries) is used as effective grain size for the martensitic transformation that correlates with the martensite substructure size such as block size.

During the heating-up to solution annealing temperature of 1030 °C, two austenitization phenomena such as (1) the austenite memory effect, and for further heating (2) spontaneous recrystallization (i.e. recrystallization without previous deformation) are directly evidenced by high temperature *in-situ* EBSD for the first time in the commercial PH 15-5 steel. The austenite memory effect describes the formation of reversed austenite, out of a martensitic matrix, during an austenitization treatment with the same crystal orientation, grain size and grain shape as prior austenite. The Austenite memory effect is observed up to an austenitization temperature of 850 °C, at higher temperatures spontaneous recrystallization seem to be kinetically preferred. It is assumed that the transformation mechanism postulated by Nakada et al. [70] is responsible for austenite the austenite memory effect in PH 15-5 steel. This transformation mechanism describes the nucleation and subsequent growth of acicular austenite on martensite lath boundaries with strict crystallographic limitations. Additional internal stress fields of the martensitic microstructure restricting the evolving crystal orientation of reversed austenite to the crystal orientation of prior austenite, i.e. austenite

memory effect. Furthermore, the inheritance of crystal defects, such as misorientations between the various martensitic laths, from martensite to austenite by the present formation mechanism of the austenite memory effect is postulated. High temperature *in-situ* EBSD investigations of austenite exhibiting austenite memory effect reveal a high KAM indicating a high amount of GND and therefore underpin this postulation.

After spontaneous recrystallization, observed at 1030 °C, the GND density decreases immediately. Although, only qualitative conclusions concerning the GND density can be drawn because of the relatively large EBSD step size of 1 µm. However, the presence of spontaneous recrystallization during solution annealing is additionally evidenced for the bulk material by *ex-situ* investigations of the prior austenite grain size. Furthermore, the influence of the heating rate and subsequent solution annealing cycles on the austenite grain refinement due to spontaneous recrystallization was investigated. An increase of the heating rate results in a stronger austenite grain refinement. However, it is assumed that the nucleation site of spontaneous recrystallization shifts from LAGB inside the austenite grain, exhibiting austenite memory effect, for low heating rates (<0.3 °C/s) to austenite grain boundaries for high heating rates (>10 °C/s). A possible explanation for such behavior is the strong partitioning of austenite stabilizing elements on martensite lath and block boundaries during heating with low heating rates. However, it remains unclear whether the stronger spontaneous recrystallization is caused by an enhanced GND density of austenite, exhibiting the austenite memory effect, or a higher number of nucleation sites for spontaneous recrystallization. The application of subsequent solution annealing cycles with a heating rate of 2 °C/s results in a plateau of approximately 20 µm for austenite grain size after 2 cycles, indicating an equilibrium of austenite grain refinement due to spontaneous recrystallization and grain growth for solution annealing at 1030 °C for 30 min.

High temperature *in-situ* EBSD measurements during martensite formation indicate that the first formed martensite blocks are larger than the subsequently formed ones. This is contributed to the increasing austenite strength due to the lower transformation temperature of martensite blocks formed later and a strengthening of austenite due to the induced straining caused by the growing martensitic phase compared to the austenitic phase.

Furthermore, the influence of effective austenite grain size on the martensite block size was investigated by the comparison of the three material states IAS, AS and CG. The results indicate an increase of the size of the first formed martensite blocks with increasing effective austenite grain size.

However, a controversial trend for the martensite block size according to number fraction is observed. Here, a coarser effective austenite grain size results in a finer martensite block size according to number fraction. This observation is attributed to a more homogeneous martensite variant distribution. It is postulated, that the range of the elastic strain field induced by the first forming martensite variant determines the martensite variant distribution. For strain fields exceeding the effective austenite grain size, it is assumed that the martensite variants are activated over several surrounding austenite twins in order to minimize the total shear of the martensitic transformation. For larger austenite twins, it is assumed that the range of the strain field of the first forming variant do not exceed the austenite twin boundary. Therefore, the minimization of the total shear takes place inside one twin. This difference of the total shear compensation may lead to a difference of the strengthening of austenite during martensite transformation thus, despite a larger effective austenite grain size, a smaller martensite blocks size can be observed. It is assumed that the chemical composition of the austenitic matrix and therefore its strength is comparable for the investigated material states (IAR, AS and CG) because of a comparable solution state (i.e. the same final solution annealing for AS and CG material state and a comparable cooling rate after hot deformation for the IAR material state). However, the verification and quantification of this theoretical approach is still part of ongoing research.

The findings of this work concerning the inheritance of GND by the austenite memory effect, the heating rate dependence of spontaneous recrystallization or the formation of martensite block size and variant distribution are also applicable for other low carbon lath martensitic steels. They contribute to a deeper understanding of the interplay between the austenitic and martensitic microstructure and enable the optimization of the martensitic substructure in order to optimize the resulting mechanical properties of the final component.

6 Conclusions on microstructural findings

In the following, the main conclusions on microstructural findings of the present work are summarized concerning the development of austenite substructure during forging, solution annealing and subsequent martensitic transformation during cooling to room temperature:

- Strong formation of annealing twins in austenite during and after hot deformation of the EAR and IAR material state is evidenced, indicating a relatively low stacking fault energy PH 15-5, which was estimated to be 13.9 mJ/m^2 according to existing prediction formulas [101].
- The austenite twin size (i.e. the austenite grain size taking the austenite twin boundaries into consideration) is determined as effective parent grain size for the martensitic transformation.
- Austenite memory effect and so-called spontaneous recrystallization is directly evidenced in PH 15-5 by high temperature *in-situ* EBSD measurements in the temperature range of about 730 °C to 1030 °C.
- As nucleation site for spontaneous recrystallization, LAGB inside austenite, exhibiting austenite memory effect were found in case of low heating rates (<0.3 °C/s), and additionally austenite grain boundaries were found as nucleation sites for spontaneous recrystallization in case of high heating rates (>10 °C/s).
- The decrease of dislocation density inherited from martensite to austenite by the austenite memory effect is indicated as decisive for spontaneous recrystallization.
- First forming martensite blocks are larger than the subsequent blocks formed at lower temperatures. Additionally, a coarse austenite grain is the reason for coarser martensite blocks forming in the beginning of martensite transformation.
- All investigated material states exhibit an angular deviation of the existing OR (i.e. the calculated OR) from ideal KS OR between 1.8° and 2.9° for closed packed planes and 1.2° and 1.7° for closed packed directions of austenite and martensite.

- It is assumed that the martensite variant distribution may appear more irregular if the elastic strain field of the first forming martensite variants exceeds the effective austenite grain size.
- A coarser martensite block structure according to number fraction is observed for smaller effective austenite grain size exhibiting an irregular martensite variant distribution.

7 Outlook

The results, presented in this thesis, provide new insights in the development of the austenitic microstructure during solution annealing of PH 15-5 and the interrelation between austenitic and martensitic substructure. However, new challenges arises in order to clarify open points, which exceed the scope of this thesis.

One of the open questions is the influence of the initial microstructure on austenite formation based on the austenite memory effect and on spontaneous recrystallization. In the present work, *in-situ* high temperature EBSD investigations concerning the austenite memory effect and spontaneous recrystallization are conducted on the same initial microstructure, i.e. industrial as-received material state. Especially, the influence of the prior austenite grain size on spontaneous recrystallization is interesting as prior austenite grain boundaries are assumed as nucleation sites for spontaneous recrystallization. Therefore, prior austenite grain refinement is expected to accelerate the occurrence of spontaneous recrystallization. However, in order to evidence this hypothesis, *in-situ* high temperature EBSD measurements of a material state with smaller prior austenite grain size are planned. Additionally, more EBSD measurements between the finish temperature of the austenitic phase transformation (~850 °C) and solution annealing temperature (1030 °C) have to be conducted in order to investigate potential nucleation sites for spontaneous recrystallization.

Additionally, the influence of the heating rate on the GND in austenite exhibiting austenite memory effect is still part of ongoing research in order to clarify the heating rate dependence of austenite grain refinement due to spontaneous recrystallization.

A promising approach for the explanation of the differences in martensite variant distribution between coarse and fine twin structure is the definition of a characteristic length of the strain field induced by the first forming martensite variant inside an austenite twin. It is postulated that this specific range may affect the distribution of martensite variants by the activation of supplementary austenite grains if the strain field exceeds the austenite twin boundary in order to compensate the transformation induced shear stress of the martensitic microstructure. A simulation of this strain field, which considers the composition and temperature dependent austenite strength may predict the differences in the martensite variant distribution between differ-

ent steel types and may contribute to a deeper understanding of the development of the martensite substructure, such as block size, in various steel types.

8 References

[1] F. Niessen, Austenite reversion in low-carbon martensitic stainless steels – a CALPHAD-assisted review, Mater. Sci. Technol. 0836 (2018) 1–14. doi:10.1080/02670836.2018.1449179.

[2] K.J. Irvine, D.J. Crowe, F.B. Pickering, The physical metallurgy of 12% chromium steels.pdf, J. Iron Steel Inst. 193 (1960) 386–405.

[3] J.W. Morris, Z. Guo, C.R. Krenn, Y. Kim, The Limits of Strength and Toughness in Steel, ISIJ Int. 41 (2001) 599–611. doi:10.2355/isijinternational.41.599.

[4] M. Abdelshehid, K. Mahmodieh, K. Mori, L. Chen, P. Stoyanov, D. Davlantes, J. Foyos, J. Ogren, R. Clark, O.S. Es-Said, On the correlation between fracture toughness and precipitation hardening heat treatments in 15-5PH Stainless Steel, Eng. Fail. Anal. 14 (2007) 626–631. doi:10.1016/j.engfailanal.2006.03.001.

[5] X. Peng, X. Zhou, X. Hua, Z. Wei, H. Liu, Effect of Aging on Hardening Behavior of 15-5 PH Stainless Steel, J. Iron Steel Res. Int. 22 (2015) 607–614. doi:10.1016/S1006-706X(15)30047-9.

[6] M. Raefsky, Fatigue Properties of 17-4 PH and 15-5 PH steel in the H-900 and H-1050 Condition, Boeing Vertol Co. Philadelphia PA. (1968).

[7] E. Herny, P. Lours, E. Andrieu, J.M. Cloué, P. Lagain, Evolution of microstructure and impact-strength energy in thermally and thermomechanically aged 15-5 PH, J. Mater. Des. Appl. 222 (2008) 299–304. doi:10.1243/14644207JMDA190.

[8] H.R. Habibi Bajguirani, The effect of ageing upon the microstructure and mechanical properties of type 15-5 PH stainless steel, Mater. Sci. Eng. A. 338 (2002) 142–159. doi:10.1016/S0921-5093(02)00062-X.

[9] L. Couturier, F. De Geuser, M. Descoins, A. Deschamps, Evolution of the microstructure of a 15-5PH martensitic stainless steel during precipitation hardening heat treatment, Mater. Des. 107 (2016) 416–425. doi:10.1016/j.matdes.2016.06.068.

[10] T. Zhou, R.P. Babu, J. Odqvist, H. Yu, P. Hedström, Quantitative electron microscopy and physically based modelling of Cu precipitation in precipitation-hardening martensitic stainless steel 15-5 PH, Mater. Des. 143 (2018) 141–149. doi:10.1016/j.matdes.2018.01.049.

[11] A. Kumar, Y. Balaji, N.E. Prasad, Indigenous development and airworthiness certification of 15 – 5 PH precipitation hardenable

stainless steel for, 38 (2013) 3–23.

[12] E. Herny, E. Andrieu, J. Lacaze, F. Danoix, N. Lecoq, Study by Differential Thermal Analysis of Reverse Spinodal Transformation in 15-5 PH Alloy., Solid State Phenom. 172–174 (2011) 338–343. doi:10.4028/www.scientific.net/SSP.172-174.338.

[13] S. MORITO, H. SAITO, T. OGAWA, T. FURUHARA, T. MAKI, Effect of Austenite Grain Size on the Morphology and Crystallography of Lath Martensite in Low Carbon Steels, ISIJ Int. 45 (2005) 91–94. doi:10.2355/isijinternational.45.91.

[14] T. Furuhara, K. Kikumoto, H. Saito, T. Sekine, T. Ogawa, S. Morito, T. Maki, Phase Transformation from Fine-grained Austenite, ISIJ Int. 48 (2008) 1038–1045. doi:10.2355/isijinternational.48.1038.

[15] C. Wang, M. Wang, J. Shi, W. Hui, H. Dong, Effect of microstructural refinement on the toughness of low carbon martensitic steel, Scr. Mater. 58 (2008) 492–495. doi:10.1016/j.scriptamat.2007.10.053.

[16] Y. Liang, S. Long, P. Xu, Y. Lu, Y. Jiang, Y. Liang, The important role of martensite laths to fracture toughness for the ductile fracture controlled by the strain in EA4T axle steel, Mater. Sci. Eng. A. 695 (2017) 154–164. doi:10.1016/j.msea.2017.03.110.

[17] J. Hidalgo, M.J. Santofimia, Effect of Prior Austenite Grain Size Refinement by Thermal Cycling on the Microstructural Features of As-Quenched Lath Martensite, Metall. Mater. Trans. A. 47 (2016) 5288–5301. doi:10.1007/s11661-016-3525-4.

[18] C. Celada-casero, J. Sietsma, M. Jesus, The role of the austenite grain size in the martensitic transformation in low carbon steels, Mater. Des. 167 (2019). doi:10.1016/j.matdes.2019.107625.

[19] N. Tsuji, T. Maki, Enhanced structural refinement by combining phase transformation and plastic deformation in steels, Scr. Mater. 60 (2009) 1044–1049. doi:10.1016/j.scriptamat.2009.02.028.

[20] V. Anil Kumar, M.K. Karthikeyan, R.K. Gupta, F. Gino Prakash, P. Ram Kumar, Aging Behavior in 15-5 PH Precipitation Hardening Martensitic Stainless Steel, Mater. Sci. Forum. 710 (2012) 483–488. doi:10.4028/www.scientific.net/MSF.710.483.

[21] T. Zhou, J. Faleskog, R.P. Babu, J. Odqvist, H. Yu, P. Hedström, Exploring the relationship between the microstructure and strength of fresh and tempered martensite in a maraging stainless steel Fe – 15Cr – 5Ni, Mater. Sci. Eng. A. 745 (2019) 420–428. doi:10.1016/j.msea.2018.12.126.

[22] P. Song, W. Liu, C. Zhang, L. Liu, Z. Yang, Reversed Austenite

Growth Behavior of a 13%Cr-5%Ni Stainless Steel during Intercritical Annealing, ISIJ Int. 56 (2016) 148–153. doi:10.2355/isijinternational.ISIJINT-2015-280.

[23] L. Morsdorf, C.C. Tasan, D. Ponge, D. Raabe, Acta Materialia 3D structural and atomic-scale analysis of lath martensite : Effect of the transformation sequence, ACTA Mater. 95 (2015) 366–377. doi:10.1016/j.actamat.2015.05.023.

[24] A. Chatterjee, A. Ghosh, A. Moitra, A.K. Bhaduri, R. Mitra, D. Chakrabarti, The role of crystallographic orientation of martensitic variants on cleavage crack propagation, Philos. Mag. Lett. Under revi (2016) 1–18.

[25] K. Tomimura, S. Takaki, Y. Tokunaga, Reversion Mechanism from Deformation Induced Martensite to Austenite in Metastable Austenitic Stainless Steels., ISIJ Int. 31 (1991) 1431–1437. doi:10.2355/isijinternational.31.1431.

[26] G.J. Krauss, Fine structure of austenite produced by the reverse martensitic transformation, Acta Metall. 11 (1963) 499–509.

[27] C.A. Apple, G. Krauss, The effect of heating rate on the martensite to austenite transformation in Fe-Ni-C alloys, Acta Metall. 20 (1972) 849–856. doi:10.1016/0001-6160(72)90077-6.

[28] J. Singh, C.M. Wayman, Formation of secondary austenite during the α'-γ transformation in an Fe-Ni-Mn alloy.pdf, Mater. Sci. Eng. 93 (1987) 227–233.

[29] P.M. Kelly, A. Jostsons, R.G. Blake, The orientation relationship between lath martensite and austenite in low carbon, low alloy steels, Acta Met. Mater. 38 (1990) 1075–1081.

[30] B. Fultz, J.I. Kim, Y.H. Kim, H.J. Kim, J.W. Morris Jr., The stability of precipitated austenite and the toughness of 9Ni steel, Met. Trans. A. 16 (1985) 2237–2249.

[31] A.F. Gourgues, Application of electron backscatter diffraction to the study of phase transformations, Int. Mater. Rev. 52 (2007) 65–128. doi:10.1179/174328007X160254.

[32] A.J. Schwartz, M. Kumar, B.L. Adams, Electron Backscatter Diffraction in Materials Science, Springer Science+Business Media, New York, 2000. doi:10.1007/978-1-4757-3205-4.

[33] V. Randle, Applications of electron backscatter diffraction to materials science : status in 2009, J Mater Sci. 42 (2009) 4211–4218. doi:10.1007/s10853-009-3570-0.

[34] S. Kundu, H.K.D.H. Bhadeshia, Transformation texture in deformed

stainless steel, Scr. Mater. 55 (2006) 779–781. doi:10.1016/j.scriptamat.2006.07.021.

[35] G. Miyamoto, N. Iwata, N. Takayama, T. Furuhara, Quantitative analysis of variant selection in ausformed lath martensite, Acta Mater. 60 (2012) 1139–1148. doi:10.1016/j.actamat.2011.11.018.

[36] S. Morito, X. Huang, T. Furuhara, T. Maki, N. Hansen, The morphology and crystallography of lath martensite in alloy steels, Acta Mater. 54 (2006) 5323–5331. doi:10.1016/j.actamat.2006.07.009.

[37] S. Morito, A.H. Pham, T. Ohba, T. Hayashi, T. Furuhara, G. Miyamoto, Three-dimensional observations of morphology of low-angle boundaries in ultra-low carbon lath martensite, Microscopy. (2017) 380–387. doi:10.1093/jmicro/dfx027.

[38] S. Morito, Y. Edamatsu, K. Ichinotani, T. Ohba, T. Hayashi, T. Furuhara, G. Miyamoto, N. Takayama, Quantitative analysis of three-dimensional morphology of martensite packets and blocks in iron-carbon-manganese steels, J. Alloys Compd. 577 (2013) S587–S592. doi:10.1016/j.jallcom.2012.02.004.

[39] S. Zhang, S. Morito, Y. Komizo, Variant Selection of Low Carbon High Alloy Steel in an Austenite Grain during Martensite Transformation, ISIJ Int. 52 (2012) 510–515.

[40] T. Chiba, G. Miyamoto, T. Furuhara, Variant selection of lenticular martensite by ausforming, Scr. Mater. 67 (2012) 324–327. doi:10.1016/j.scriptamat.2012.05.007.

[41] L. Malet, M.R. Barnett, P.J. Jacques, S. Godet, Variant selection during the c -to- a b phase transformation in hot-rolled bainitic TRIP-aided steels, Scr. Mater. 61 (2009) 520–523. doi:10.1016/j.scriptamat.2009.05.015.

[42] N. Takayama, G. Miyamoto, T. Furuhara, Effects of transformation temperature on variant pairing of bainitic ferrite in low carbon steel, Acta Mater. 60 (2012) 2387–2396. doi:10.1016/j.actamat.2011.12.018.

[43] C.C. Kinney, K.R. Pytlewski, A.G. Khachaturyan, J.W. Morris, The microstructure of lath martensite in quenched 9Ni steel, Acta Mater. 69 (2014) 372–385. doi:10.1016/j.actamat.2014.01.058.

[44] J.W. Morris, C. Kinney, K. Pytlewski, Y. Adachi, Microstructure and cleavage in lath martensitic steels, Sci. Technol. Adv. Mater. 14 (2013) 014208. doi:10.1088/1468-6996/14/1/014208.

[45] S. Li, G. Zhu, Y. Kang, Effect of substructure on mechanical properties and fracture behavior, J. Alloys Compd. 675 (2016) 104–115. doi:10.1016/j.jallcom.2016.03.100.

[46] T. Nyyssönen, M. Isakov, P. Peura, V.T. Kuokkala, Iterative Determination of the Orientation Relationship Between Austenite and Martensite from a Large Amount of Grain Pair Misorientations, Metall. Mater. Trans. A Phys. Metall. Mater. Sci. 47 (2016) 2587–2590. doi:10.1007/s11661-016-3462-2.

[47] C. Cayron, B. Artaud, L. Briottet, Reconstruction of parent grains from EBSD data, Mater. Charact. 57 (2006) 386–401. doi:10.1016/j.matchar.2006.03.008.

[48] L. Germain, N. Gey, R. Mercier, P. Blaineau, M. Humbert, An advanced approach to reconstructing parent orientation maps in the case of approximate orientation relations: Application to steels, Acta Mater. 60 (2012) 4551–4562. doi:10.1016/j.actamat.2012.04.034.

[49] T. Shinozaki, Y. Tomota, T. Fukino, T. Suzuki, Microstructure Evolution during Reverse Transformation of Austenite from Tempered Martensite in Low Alloy Steel, ISIJ Int. 57 (2017) 533–539.

[50] H. Shirazi, G. Miyamoto, S. Hossein Nedjad, T. Chiba, M. Nili Ahmadabadi, T. Furuhara, Microstructure evolution during austenite reversion in Fe-Ni martensitic alloys, Acta Mater. 144 (2018) 269–280. doi:10.1016/j.actamat.2017.10.068.

[51] G.G.E. Seward, D.J. Prior, J. Wheeler, S. Celotto, D.J.M. Halliday, R.S. Paden, M.R. Tye, High-Temperature Electron Backscatter Diffraction and Scanning Electron Microscopy Imaging Techniques : In-situ Investigations of Dynamic Processes, Scanning. 24 (2002) 232–240.

[52] Z. Nishiyama, M.E. Fine, M. Meshii, C.M. Wayman, Martensitic transformation, (1978). https://books.google.com.au/books?id=tqVTAAAAMAAJ.

[53] H. Kitahara, R. Ueji, N. Tsuji, Y. Minamino, Crystallographic features of lath martensite in low-carbon steel, Acta Mater. 54 (2006) 1279–1288. doi:10.1016/j.actamat.2005.11.001.

[54] H. K. D. H. Bhadeshia, Worked Examples in the Geometry of Crystals, 2006. doi:10.1524/zkri.1991.195.1-2.155.

[55] G. Kurdjumov, G. Sachs, Üeber den Mechanismus der Stahlhärtung.pdf, Z. Phys. 64 (1930) 325–343.

[56] S. Nambu, N. Shibuta, M. Ojima, J. Inoue, T. Koseki, H.K.D.H. Bhadeshia, In situ observations and crystallographic analysis of martensitic transformation in steel, Acta Mater. 61 (2013) 4831–4839. doi:10.1016/j.actamat.2013.04.065.

[57] Z. Nishiyama, X-Ray investigation of the mechanism of

transformation from face-centerd cubic lattice to body-centered cubic, Sci Rep Res Inst, Tohoku Univ. 23 (1934) 638.

[58] S. Morito, X. Huang, T. Furuhara, T. Maki, N. Hansen, The morphology and crystallography of lath martensite in Fe-C alloys, Acta Mater. 54 (2003) 5323–5331. doi:10.1016/j.actamat.2006.07.009.

[59] A.B. Greninger, A.R. Troiano, The mechanism of martensite formation.pdf, J. Met Trans. 185 (1949) 590–598.

[60] K.D. Zilnyk, D.R. Almeida Junior, H.R.Z. Sandim, P.R. Rios, D. Raabe, Misorientation distribution between martensite and austenite in Fe-31 wt%Ni-0.01 wt%C, Acta Mater. 143 (2018) 227–236. doi:10.1016/j.actamat.2017.10.026.

[61] H.K.D.H. Bhadeshia, Bainite in steels.Theory and Practice, 2015. doi:10.1017/CBO9781107415324.004.

[62] L. Qi, A.G. Khachaturyan, J.W.M. Jr, The microstructure of dislocated martensitic steel : Theory, ACTA Mater. 76 (2014) 23–39. doi:10.1016/j.actamat.2014.04.038.

[63] J.G. Back, G. Engberg, Investigation of parent austenite grains from Martensite Structure Using EBSD in a Wear Resistant steel, Materials (Basel). 10 (2017). doi:10.3390/ma10050453.

[64] F. Maresca, V.G. Kouznetsova, M.G.D. Geers, Subgrain lath martensite mechanics: A numerical-experimental analysis, J. Mech. Phys. Solids. 73 (2014) 69–83. doi:10.1016/j.jmps.2014.09.002.

[65] T. Furuhara, N. Takayama, G. Miyamoto, Key Factors in Grain Refinement of Martensite and Bainite, Mater. Sci. Forum. 638 (2010) 3044–3049. doi:10.4028/www.scientific.net/MSF.638-642.3044.

[66] H.K.D.H. Bhadeshia, Problems in the Calculation of Transformation Texture in Steels, 50 (2010) 1517–1522.

[67] S. Kundu, K. Hase, H.K.D.H. Bhadeshia, Crystallographic texture of stress-affected bainite, Proc. R. Soc. A Math. Phys. Eng. Sci. 463 (2007) 2309–2328. doi:10.1098/rspa.2007.1881.

[68] G. Miyamoto, N. Iwata, N. Takayama, T. Furuhara, Mapping the parent austenite orientation reconstructed from the orientation of martensite by EBSD and its application to ausformed martensite, Acta Mater. 58 (2010) 6393–6403. doi:10.1016/j.actamat.2010.08.001.

[69] Oxford Instruments NanoAnalysis, Generating Orientation Maps to Present EBSD Data, AZoM <https//Www.Azom.Com/Article.Aspx?ArticleID=11775. (2019).

[70] N. Nakada, T. Tsuchiyama, S. Takaki, S. Hashizume, Variant Selection of Reversed Austenite in Lath Martensite, ISIJ Int. 47 (2007)

1527–1532. doi:10.2355/isijinternational.47.1527.

[71] V.D. Sadovski, G.N. Bogacheva, V.M. Umova, Recrystallization of maraging alloys, Phys. Met. Inst. 4 (1969) 10–12.

[72] Y. Tomota, W. Gong, S. Harjo, T. Shinozaki, Reverse austenite transformation behavior in a tempered martensite low-alloy steel studied using in situ neutron diffraction, Scr. Mater. 133 (2017) 79–82. doi:10.1016/j.scriptamat.2017.02.017.

[73] D. Brandl, M. Lukas, M. Stockinger, S. Ploberger, G. Ressel, Evidence of austenite memory in PH 15-5 and assessment of its formation mechanism, Mater. Des. 176 (2019) 107841. doi:10.1016/j.matdes.2019.107841.

[74] S. Watanabe, T. Kunitake, On the Formation of Austenite Grains from Prior Martensitic Structure, Tetsu-Do-Hagane. 61 (1975) 96–106.

[75] X. Zhang, G. Miyamoto, Y. Toji, S. Nambu, T. Koseki, T. Furuhara, Orientation of austenite reverted from martensite in Fe-2Mn-1.5Si-0.3C alloy, Acta Mater. 144 (2018) 601–612. doi:10.1016/j.actamat.2017.11.003.

[76] L. Liu, Z.G. Yang, C. Zhang, Effect of retained austenite on austenite memory of a 13% Cr-5% Ni martensitic steel, J. Alloys Compd. 577 (2013) S654–S660. doi:10.1016/j.jallcom.2012.04.021.

[77] S.T. Kimmins, D.J. Gooch, Austenite memory effect in 1Cr-1 Mo-O-75V (Ti , B) steel, Met. Sci. 17 (1983) 519–532.

[78] S.J. Lee, Y.M. Park, Y.K. Lee, Reverse transformation mechanism of martensite to austenite in a metastable austenitic alloy, Mater. Sci. Eng. A. 515 (2009) 32–37. doi:10.1016/j.msea.2009.02.010.

[79] N. Nakada, T. Tschiyama, S. Takaki;, D. Ponge;, D. Raabe, Transition from diffusive to displacive austenite reversion in low-alloy steel, ISIJ Int. 53 (2013) 2275–2277.

[80] N. Nakada, R. Fukagawa, T. Tsuchiyama, S. Takaki, D. Ponge, D. Raabe, Inheritance of dislocations and crystallographic texture during martensitic reversion into austenite, ISIJ Int. 53 (2013) 1286–1288. doi:10.2355/isijinternational.53.1286.

[81] L. Liu, Z.G. Yang, C. Zhang, W.B. Liu, An in situ study on austenite memory and austenitic spontaneous recrystallization of a martensitic steel, Mater. Sci. Eng. A. 527 (2010) 7204–7209. doi:10.1016/j.msea.2010.07.083.

[82] L.P. Kubin, A. Mortensen, Geometrically necessary dislocations and strain-gradient plasticity: A few critical issues, Scr. Mater. 48 (2003) 119–125. doi:10.1016/S1359-6462(02)00335-4.

[83] A. Ramazani, K. Mukherjee, A. Schwedt, P. Goravanchi, U. Prahl, W. Bleck, Quantification of the effect of transformation-induced geometrically necessary dislocations on the flow-curve modelling of dual-phase steels, Int. J. Plast. 43 (2013) 128–152. doi:10.1016/j.ijplas.2012.11.003.

[84] X. Zhang, G. Miyamoto, T. Kaneshita, Y. Yoshida, Y. Toji, T. Furuhara, Growth mode of austenite during reversion from martensite in Fe-2Mn-1.5Si-0.3C alloy: A transition in kinetics and morphology, Acta Mater. 154 (2018) 1–13. doi:10.1016/j.actamat.2018.05.035.

[85] K.Z. Baba-Kishi, Electron backscatter Kikuchi diffraction in the scanning electron microscope, J. Mater. Sci. 37 (2002) 1715–1746.

[86] S. I. Wright, M. M. Nowell, D. P. Field, A_Review_of_Strain_Analysis_Using_EBSD_HR.pdf, (2011).

[87] S. Villert, C. Maurice, C. Wyon, R. Fortunier, Accuracy assessment of elastic strain measurement by EBSD, J. Microsc. 233 (2009) 290–301.

[88] Oxford Instruments, Basics of Automated Indexing, Www.Ebsd.Com/Ebsd-Explained/Basics-of-Automated-Indexing. (2019).

[89] T.B. Britton, J. Jiang, Y. Guo, A. Vilalta-clemente, D. Wallis, L.N. Hansen, A. Winkelmann, A.J. Wilkinson, Materials Characterization Tutorial : Crystal orientations and EBSD — Or which way is up ?, Mater. Charact. 117 (2016) 113–126. doi:10.1016/j.matchar.2016.04.008.

[90] R. de Kloe, Do You Want to Be Average(d)?, (2019). edaxblog.com/2015/09/22/do-you-want-to-be-averaged/.

[91] J. Jiang, T.B. Britton, A.J. Wilkinson, Measurement of geometrically necessary dislocation density with high resolution electron backscatter diffraction: Effects of detector binning and step size, Ultramicroscopy. 125 (2013) 1–9. doi:10.1016/j.ultramic.2012.11.003.

[92] D.P. Field, Recent advances in the application of orientation imaging, Ultramicroscopy. 67 (1997) 1–9.

[93] S.I. Wright, M.M. Nowell, EBSD Image Quality Mapping, Microsc. Microanal. 12 (2006) 72–84. doi:10.1017/S1431927606060090.

[94] C. Bernhard, S. Schider, A. Sormann, G. Xia, S. Ilie, Erste Ergebnisse des neuen Hochtemperatur-Konfokalmikroskops am Lehrstuhl fuer Metallurgie, Berg- Und Huettenmaennische Mont. 156 (2011) 161–167. doi:10.1007/ s00501-011-0645-4.

[95] D. Brandl, L. Höfler, M. Stockinger, S. Ploberger, S. Marsoner, G.

Ressel, Presentation and Verification of an Electrolytic Etching Technique for the Determination of prior Austenite Grain Boundaries in the Steel PH15-5, Pract. Metallogr. 55 (2018) 800–812. doi:10.3139/147.110497.

[96] and C.S. Higginson, R., Worked examples in quantitative metallography, 2003.

[97] A. DEHGHAN-MANSHADI, M.R. Barnett, P.D. Hodgson, Hot Deformation and Recrystallization of Austenitic Stainless Steel : Part I . Dynamic Recrystallization, Metall. Mater. Trans. A. 39 (2008). doi:10.1007/s11661-008-9512-7.

[98] T.H. Blewitt, R.R. Coltman, J.K. Redman, Low-temperature deformation of copper single crystals, J. Appl. Phys. 28 (1957) 651–660. doi:10.1063/1.1722824.

[99] F.J. Humphreys;, M. Hatherly, Recrystallization and related annealing phenomena, Second Edi, Elsevier Ltd, Kidlington, Oxford, 2004.

[100] H. Mirzadeh, J.M. Cabrera, A. Najafizadeh, P.R. Calvillo, EBSD study of a hot deformed austenitic stainless steel, Mater. Sci. Eng. A. 538 (2012) 236–245. doi:10.1016/j.msea.2012.01.037.

[101] C.G. Rhodes, A.W. Thompson, The Composition Dependence of Stacking Fault Energy in Austenitic Stainless Steels, Metall. Trans. A. 8A (1977) 1901–1906.

[102] J. Lu, L. Hultman, E. Holmström, K.H. Antonsson, M. Grehk, W. Li, L. Vitos, A. Golpayegani, Stacking fault energies in austenitic stainless steels, Acta Mater. 111 (2016) 39–46. doi:10.1016/j.actamat.2016.03.042.

[103] P.R. Rios, F. Siciliano, R.Z. Sandim, R.L. Plaut, A.F. Padilha, Nucleation and Growth During Recrystallization, Mater. Res. 8 (2005) 225–238.

[104] F. Niessen, M. Villa, J. Hald, M.A.J. Somers, Kinetics analysis of two-stage austenitization in supermartensitic stainless steel, Mater. Des. 116 (2017) 8–15. doi:10.1016/j.matdes.2016.11.076.

[105] J. Pak, D. Woo, H.K.D.H. Bhadeshia, Displacive Phase Transformation and Surface E ff ects associated with Confocal Laser Scanning Microscopy, Metall. Mater. Trans. A. 43 (2012) 4520–4525.

[106] D.N. Githinji, S.M. Northover, P.J. Bouchard, M.A. Rist, An EBSD Study of the Deformation of Service-Aged 316 Austenitic Steel, Metall. Mater. Trans. A. 44A (2013) 4150–4167. doi:10.1007/s11661-013-1787-7.

[107] M. Umemoto, W.S. Owen, Effects of austenitizing temperature and austenite grain size on the formation of athermal martensite in an iron-nickel and an iron-nickel-carbon alloy, Metall. Trans. 5 (1974) 2041–2046.

9 List of figures

10 List of tables

11 Publications

11.1 Overview

Two publications are appended to the present work in order to deliver additional information to the presented results.

Publication A describes the electrolytic etching method in order to reveal prior austenite grain boundaries in PH 15-5. Grain boundary etching in high purity steel with enhanced amount of Cr is challenging but essential for the investigation of the prior austenite microstructure. Therefore, publication A presents the etching routine and additional concussions concerning the prior austenite twin structure.

Publication B deals with the evidence and postulated transformation mechanism of the austenite memory effect in PH 15-5. Supplementary to the presented results of the austenite memory effect in the thesis, the experimental evidence for the chosen transformation mechanism is described.

11.2 List of appended publications

Paper A

D. Brandl, L. Höfler, M. Stockinger, S. Ploberger, S. Marsoner, G. Ressel
Presentation and Verification of an Electrolytic Etching Technique for the Determination of prior Austenite Grain Boundaries in the Steel PH15-5
Practical Metallography 55 (2018) 800 - 812

Paper B

D. Brandl, M. Lukas, M. Stockinger, S. Ploberger, G. Ressel
Evidence of austenite memory in PH 15-5 and assessment of its formation mechanism
Materials & Design 176 (2019), 176 (2019) 107841

Publication A

Presentation and Verification of an Electrolytic Etching Technique for the Determination of prior Austenite Grain Boundaries in the Steel PH15-5

D. Brandl, L. Höfler, M. Stockinger, S. Ploberger,
S. Marsoner, G. Ressel

D. Brandl, L. Höfler, M. Stockinger, S. Ploberger, S. Marsoner, G. Ressel

Presentation and Verification of an Electrolytic Etching Technique for the Determination of prior Austenite Grain Boundaries in the Steel PH15-5

Darstellung und Verifizierung einer elektrolytischen Ätzmethode zur Bestimmung ehemaliger Austenitkorngrenzen eines PH15-5 Stahls

Received: December 13, 2017
Accepted: July 03, 2018

Eingegangen: 13. Dezember 2017
Angenommen: 03. Juli 2018
Übersetzung: V. Müller

Abstract

In the field of hot working, modelling of austenite grain size makes a significant contribution to the prediction of future material properties. One of the difficulties when it comes to modelling is the detection of grain sizes at different recrystallization stages by means of etching methods. Especially with high-purity steels with a martensitic structure, imaging of prior austenite grain boundaries without simultaneous highlighting

Kurzfassung

Im Bereich der Warmumformung bildet die Modellierung der Austenitkorngröße einen wesentlichen Beitrag zur Vorhersage der späteren Materialeigenschaften. Eine Schwierigkeit dieser Modellierung besteht darin, die Korngrößen durch ätztechnische Methoden bei unterschiedlichen Stadien der Rekristallisation zu erfassen. Besonders bei hochreinen Stählen mit martensitischer Struktur ist die Darstellung der ehemaligen Austenitkorn-

Authors:

Dominik Brandl, Lukas Höfler, Stefan Marsoner, Gerald Ressel Materials Center Leoben Forschung GmbH (MCL), 8700 Leoben, Austria; e-mail: Dominik.Brandl@mcl.at, Lukas.Hoefler@mcl.at, Stefan.Marsoner@mcl.at, Gerald.Ressel@mcl.at
Martin Stockinger voestalpine Böhler Aerospace GmbH & Co KG, A-8605 Kapfenberg, Austria; e-mail: Martin.Stockinger@bohler-forging.com
Sarah Plobergerc voestalpine Böhler Edelstahl GmbH & Co KG, A-8605 Kapfenberg, Austria; e-mail: Sarah.Ploberger@bohler-edelstahl.at

of lath martensite boundaries, is, in many cases, only possible to some extent when using etching technology. Due to small electrochemical potential differences, increased purity of the alloy causes a more uniform etching attack on grain and lath boundaries and thus leads to a poorer discrimination. An alternative technique for grain size determination is Electron Backscatter Diffraction (EBSD). However, this technique maps only a relatively small area of the sample and is also significantly more expensive than the combination of electrolytic etching and light microscopic analysis.

Therefore, this work will present a novel electrolytic etching technique for light microscopic imaging of prior austenite grain boundaries in high-purity and corrosion-resistant grades of precipitation hardening steels. For this purpose, a series of tests was carried out on the alloy PH15-5 and the results were verified by correlative EBSD measurements.

1. Introduction

The material PH15-5 is a corrosion-resistant and precipitation hardening steel grade with a martensitic matrix. It is for example used in structural components in the aviation industry as it combines properties such as high strength and fracture toughness together with a good corrosion resistance [1, 2]. In order to control and model the production process of these components by means of hot working, it is essential to characterize recrystallization and grain growth as precisely as possible. One important parameter in this respect is austenite grain size, which will be determined after defined hot working processes which use different degrees of deformation, forming rates und temperatures.

One option for the reconstruction of prior austenite grain boundaries in steels with a

grenzen, ohne gleichzeitiges Hervorheben der Martensitlattengrenzen, durch ätztechnische Methoden oft nur bedingt möglich. Eine erhöhte Reinheit der Legierung führt aufgrund geringer elektrochemischer Potentialunterschiede zu einem gleichmäßigeren Ätzangriff von Korn- und Lattengrenzen und dadurch zu einer schlechteren Unterscheidbarkeit. Eine alternative Methode zur Korngrößenbestimmung stellt die Elektronenrückstreubeugung (EBSD) dar, welche jedoch eine verhältnismäßig kleine Probenfläche abbildet und zudem deutlich teurer als die Kombination aus elektrolytischer Ätzung und lichtmikroskopischer Analyse ist.

Diese Arbeit präsentiert daher eine neue elektrolytische Ätzmethode zur lichtmikroskopischen Darstellung von ehemaligen Austenitkorngrenzen in hochreinen und korrosionsbeständigen Stahlgüten ausscheidungshärtbarer Stähle. Dafür wurde eine Versuchsreihe an der Legierung PH15-5 durchgeführt und das Ergebnis durch korrelative EBSD-Messungen verifiziert.

1. Einleitung

Bei dem Werkstoff PH15-5 handelt es sich um eine korrosionsbeständige und ausscheidungshärtbare Stahllegierung mit martensitischer Matrix. Sie wird aufgrund ihrer Eigenschaftskombination aus hoher Festigkeit und Bruchzähigkeit gepaart mit guter Korrosionsbeständigkeit unter anderem für Strukturbauteile in der Luftfahrtindustrie verwendet [1, 2]. Um den Herstellungsprozess dieser Bauteile durch Warmumformung zu kontrollieren und zu modellieren, ist es notwendig Rekristallisation und Kornwachstum möglichst genau zu beschreiben. Ein wichtiger Parameter ist hierfür die Korngröße des Austenits, die nach definierten Warmumformungen mit verschiedenen Umformgraden, Umformraten und Temperaturen ermittelt wird.

Eine Möglichkeit zur Darstellung von ehemaligen Austenitkorngrenzen in Stählen mit

martensitic structure is offered by specific reconstruction methods which calculate the crystal orientations of prior austenite grain boundaries based on the strict orientation relationships between martensite and austenite [3–5]. For this method, however, EBSD data and the respective reconstruction algorithm are required, both of which are not always available. Etching with subsequent light microscopic analysis is a traditional method for the imaging of prior austenite grain boundaries. A differentiation is made between thermal and chemical etching techniques. Thermal etching techniques cause austenite grain boundaries to be rounded off at temperatures higher than 900 °C so that they remain visible even after cooling to room temperature and martensitic phase transition [6]. However, one disadvantage of this technique is that the area to be analyzed has to be already metallographically prepared before the last austenitizing cycle, thus only permitting an analysis of the sample surface. With chemical etching techniques, on the other hand, prior austenite grain size is determinable in nearly every location of the sample by additional metallographic target preparation. For numerous steel grades, good results may be yielded using colour etching according to Lichtenegger and Blöch [7] or picric acid-based etching solutions, which, according to Vander Voort et al., rely on phosphorus segregations at interfaces [8–10]. However, this etching technique may remove both prior austenite grain boundaries and interfaces of the martensitic structure in stainless and corrosion-resistant alloys, as pointed out by Mirzadeh [11] in his work on the material PH17–4. This fact hampers most notably the detection of smaller prior austenite grains as they cannot be differentiated from the martensitic matrix. Beckert et al. [12] stated in his work that one important parameter for revealing one specific microstructural component during etching is its

martensitischen Gefüge stellen spezielle Rekonstruktions-Methoden dar, welche die Kristallorientierungen der ehemaligen Austenitkörner mit Hilfe der strikten Orientierungsbeziehung zwischen Martensit und Austenit berechnen [3–5]. Für diese Methode werden jedoch EBSD-Daten und der jeweilige Rekonstruktions-Algorithmus benötigt, welche nicht immer zu Verfügung stehen. Eine klassische Methode zur Darstellung der ehemaligen Austenitkorngrenzen ist die Ätzung und anschließende lichtmikroskopische Auswertung. Dabei kann zwischen thermischen und chemischen Ätzmethoden unterschieden werden. Bei thermischen Ätzmethoden werden Austenitkorngrenzen bei Temperaturen über 900 °C abgerundet und bleiben somit auch nach Abkühlung auf Raumtemperatur und martensitischer Phasenumwandlung sichtbar [6]. Ein Nachteil dieser Methode ist allerdings, dass die auszuwertende Position bereits vor dem letzten Austenitisierungszyklus metallographisch präpariert werden muss und somit nur Analysen an der Probenoberfläche zulässt. Bei chemischen Ätzungen ist die ehemalige Austenitkorngröße dagegen durch nachträgliche metallographische Zielpräparation an nahezu jeder Probenposition bestimmbar. Bei zahlreichen Stahlgüten können gute Ergebnisse mit Niederschlagsätzungen nach Lichtenegger und Blöch [7] oder Ätzlösungen auf Pikrinsäurebasis erzielt werden, welche nach Vander Voort et al. auf Phosphorseigerungen an Grenzflächen zurückzuführen sind [8–10]. Bei hochreinen und korrosionsbeständigen Legierungen kann es bei dieser Ätzung allerdings zum gemeinsamen Abtrag von ehemaligen Austenitkorngrenzen und Grenzflächen der Martensitstruktur kommen, wie aus der Arbeit von Mirzadeh [11] über den Werkstoff PH17–4 hervorgeht. Dieser Umstand erschwert vor allem die Detektion von kleineren ehemaligen Austenitkörnern, da diese nicht von der martensitischen Matrix unterschieden werden können. Beckert et al. [12] beschrieb in seiner Arbeit, dass ein wichtiger Parameter für die Darstellung eines

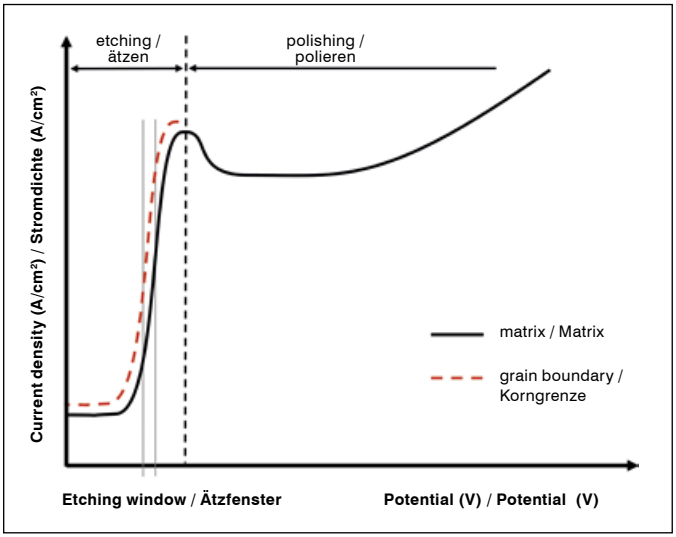

Fig. 1: *Schematic representation of the current density vs. potential curves of the matrix and grain boundary with indication of the etching range for grain boundary etching in which significantly different current densities are yielded [9, 14].*

Bild 1: *Schematische Darstellung der Stromdichte-Potential-Kurven von Matrix und Korngrenze mit Kennzeichnung des Ätzfensters für Korngrenzenätzungen, in dem stark unterschiedliche Stromdichten erzielt werden [9, 14].*

electrochemical potential. It may vary due to local differences in alloy composition or crystal orientation, for example, and thus causes areas with a lower electrochemical potential to be removed before those with a slightly higher electrochemical potential [7]. Therefore, electrolytic etching is a promising alternative to picric acid etching due to the possibility of precisely tuning a certain potential. For this etching technique, an external voltage is applied to the sample and connected – via an electrolyte – to a stainless steel or platinum electrode, acting as the cathode. The dissolution of the metal occurs at the anode, thus on the sample side, and may be controlled by the level of applied voltage. Fig. 1 shows the schematic current density vs. voltage curve and defines the areas of electrolytic etching and polishing [9]. According to the model of Bell and Sonon [14], Fig. 1 also indicates the electrolytic etching range for austenite grain boundaries. Based on two current density-potential curves, the authors characterize the behavior of the grain boundary which, compared to the matrix, is more similar to that of a base metal. The

gewissen Mikrostrukturbestandteils während einer Ätzung dessen elektrochemisches Potential ist. Dieses kann unter anderem durch lokale Unterschiede in der Legierungszusammensetzung oder Kristallorientierung variieren und somit bewirken, dass Bereiche mit geringerem elektrochemischen Potential vor jenen mit etwas höheren abgetragen werden [7]. Die elektrolytische Ätzung stellt somit aufgrund der gezielten Einstellmöglichkeit eines gewissen Potentials eine vielversprechende Alternative zur Pikrinsäureätzung dar. Bei dieser Ätzmethode wird an die Probe eine externe Spannung angelegt und durch einen Elektrolyt mit einer Edelstahl oder Platin Elektrode verbunden, die als Kathode geschaltet ist. Die Auflösung des Metalls findet an der Anode, also probenseitig, statt und lässt sich durch die Höhe der angelegten Spannung steuern. Bild 1 zeigt den schematischen Verlauf der Stromdichte bei steigender Spannung und grenzt die Bereiche des elektrolytischen Ätzens und Polierens voneinander ab [9]. Nach dem Modell von Bell und Sonon [14] ist in diesem Bild auch der elektrolytische Ätzbereich für Austenitkorngrenzen dargestellt. Die Autoren beschreiben das unedlere Ver-

graph of the grain boundary (dashed red line) shifts to lower voltages and higher current densities compared to the graph of the matrix (black continuous line), while their shape remains the same. From this theory follows that there is an etching range in which the current density of the grain boundary at a given voltage is significantly higher than that of the matrix so that dissolution rates of maximum difference are set. A voltage setting within this etching range thus yields a clearer mapping of the grain boundaries according to the model concept.

This fact was used by Couturier et al. [15], enabling them to image prior austenite grain boundaries in the material PH15-5 by electrolytic etching using an electrolyte consisting of water-based hydrofluoric acid 15 %. However, this technique also highlighted the lath martensite structure, which complicated the evaluation of the prior austenite grain size. A clearly improved result was yielded by Mirzadeh et al.'s [11] electrolytic etching using water-based nitric acid 60 % on the material PH17–4. In this case, the martensitic structure clearly recedes into the background; however, dark deposits remain on the surface of the polish.

This work will therefore present an optimized electrolytic etching technique for revealing prior austenite grain boundaries in the material PH15-5 which uses water-based nitric acid 65 % and neither reveals the martensitic structure nor causes any dark deposits. For the verification of this etching technique correlative analyses using Electron Backscatter Diffraction (EBSD) will be carried out. The pattern in the Pole Figures (PF) of martensite reflections within prior austenite grains will be compared with an ideal pattern for martensitic transformations [16].

halten der Korngrenze im Vergleich zur Matrix anhand zweier Stromdichte-Potentialkurven. Dabei ist die Kurve der Korngrenze (unterbrochene rote Linie) im Vergleich zur Matrixkurve (schwarze durchgehende Linie) zu geringeren Spannungen und höheren Stromdichten verschoben, während ihre Form gleich bleibt. Nach dieser Theorie ergibt sich ein Ätzfenster, in dem die Stromdichte der Korngrenze bei gegebener Spannung wesentlich höher als jene der Matrix ist und sich somit maximal unterschiedliche Auflösungsraten einstellen. Eine Spannungseinstellung innerhalb dieses Ätzfensters liefert daher nach der Modellvorstellung eine deutliche Darstellung der Korngrenzen.

Dies wurde auch von Couturier et al. [15] ausgenutzt, die durch elektrolytisches Ätzen mit einem Elektrolyten aus 15 %iger Flussäure auf Wasserbasis bei dem Werkstoff PH15-5 ehemalige Austenitkorngrenzen darstellten. Allerdings wurde dabei auch die Martensitlattenstruktur hervorgehoben, weshalb die Auswertung der ehemaligen Austenitkorngröße erschwert durchführbar war. Eine deutliche Verbesserung brachte die von Mirzadeh et al. [11] für den Werkstoff PH17–4 verwendete elektrolytische Ätzung mit 60 %-iger Salpetersäure auf Wasserbasis. Hier tritt die martensitische Struktur deutlich in den Hintergrund, es bleibt allerdings ein dunkler Niederschlag auf den Schliffflächen zurück.

Die vorliegende Arbeit präsentiert daher eine optimierte elektrolytische Ätzung der ehemaligen Austenitkorngrenzen des Werkstoffs PH15-5 mittels einer 65 %-igen Salpetersäure auf Wasserbasis, welche die martensitische Struktur nicht darstellt und keinen dunklen Niederschlag aufweist. Zur Verifizierung dieser Ätzung werden korrelative Analysen mit Elektronenrückstreubeugung (EBSD) durchgeführt. Dabei werden die Muster in Polfiguren (PF) von Martensit Reflexen innerhalb ehemaliger Austenitkörner mit einem Idealmuster für martensitische Umwandlungen verglichen [16].

2. Experimental

For PH15-5 , a rod material with a diameter of 150 mm, manufactured by *Böhler Edelstahl GmbH& Co KG*, the forming process took place above the recrystallization temperature and after that the material was air-cooled. The metallographic polishes were removed from the material in this state, conductively mounted, ground with a final grit size of 1000 and polished using a 1 µm diamond suspension. The chemical composition of the used sample material is given in Tab. 1.

Electrolytic etching was carried out at room temperature using a LectroPol-5 by *Struers* with a stainless steel electrode and an electrolyte consisting of water-based nitric acid 65 vol%, available as ready-to-use dilute solution by *Carl Roth GmbH & Co KG*, article number X898. The etched surface was 0.5 cm^2 in size and the device's maximum flow rate of 20 was used. With these parameters, a series of tests was started to determine the ideal etching range.

The optimum results of imaging prior austenite grain boundaries were achieved at a voltage of 1 V over 100 s. However, dark deposits frequently formed and could not be eliminated by polishing the sample, which complicated grain size evaluation. In order to remove this deposit a second etching step was thus carried out at 2.5 V over 18 s. Due to different material conditions, the voltage range in which the deposit forms may vary, but can be removed by variation of the second voltage level in most cases. After electrolytic etching, the sample again un-

2. Experimentelle Durchführung

Der Werkstoff PH15-5 wurde von der Firma Böhler Edelstahl GmbH & Co KG als Stabmaterial mit einem Durchmesser von 150 mm hergestellt, oberhalb der Rekristallisationstemperatur umgeformt und an Luft abgelegt. Die metallographischen Schliffe wurden aus diesem Zustand entnommen, leitend eingebettet, bis zu einer Körnung von 1000 geschliffen und mit einer 1 µm Diamantsuspension poliert. Die chemische Zusammensetzung des verwendeten Probenwerkstoffes wird in Tab. 1 angegeben.

Die elektrolytischen Ätzungen wurden bei Raumtemperatur an einem LectroPol-5 der Firma Struers mit einer Edelstahlkathode und einem Elektrolyt aus fertig verdünnter 65 vol.%-iger Salpetersäure auf Wasserbasis der Firma Carl Roth GmbH & Co KG mit der Artikelnummer X898 durchgeführt. Die geätzte Fläche betrug 0,5 cm^2 und es wurde die maximale am Gerät einstellbare Flussrate von 20 verwendet. Mit diesen Parametern wurde eine Versuchsserie gestartet, in der das ideale Ätzfenster bestimmt wurde.

Eine bestmögliche Darstellung der ehemaligen Austenitkorngrenzen wurde bei einer Spannung von 1 V für eine Dauer von 100 s erzielt. Es bildete sich jedoch häufig ein dunkler Niederschlag, der durch Polieren der Probe nicht zu entfernen war und die Auswertung der Korngröße erschwerte. Zur Auflösung dieses Belags wurde daher eine zweite Ätzstufe, bei 2,5 V für 18 s durchgeführt. Aufgrund unterschiedlicher Materialzustände kann der Spannungsbereich, in dem sich der Niederschlag bildet, schwanken aber in den meisten Fällen durch eine Variation des zweiten Spannungs-

C	Si	Mn	Cr	Ni	Cu	Nb	Mo	P	S
0.04	0.30	0.60	14.90	5.10	3.30	0.30	0.25	< 0.03	< 0.001

Tab. 1: *Chemical composition of the material PH15-5 in wt%.*

Tab. 1: *Chemische Zusammensetzung des Werkstoffes PH15-5 in Gew.-%.*

derwent further light polishing using 1 µm diamond suspension.

For reference and comparison, etchings using picric acid were carried out as a complement to electrolytic etching. The samples of the comparison group underwent the same metallographic preparation process and were etched at room temperature for about 45 s. The etchant is composed of 100 ml cold-saturated water-based picric acid, 20 ml WAC wetting active agent by *Compard KG* used as a wetting agent and 20 ml HCl (37 vol%).

EBSD measurements were carried out on the Auriga 40 scanning electron microscope by *Zeiss* using a Hikari Super EBSD camera by *EDAX*. An acceleration voltage of 20 keV and a step size of 300 nm for lateral resolution were used. Evaluation of the data was achieved using the program EDAX Orientation Imaging Micrograph (OIM) Analysis 8.

3. Discussion of the Results

In order to present the results of the previously described etchings, light microscopic images of the etched samples and EBSD images were obtained and contrasted for this work.

Fig. 2a shows the result of electrolytic etching on the material PH15-5 in an un-aged state, clearly revealing prior austenite grain boundaries with no visible indicators of an attack on twin boundaries or the martensitic substructure. The samples of the comparison group for which picric acid was used, however, exhibit a distinct martensitic structure which significantly hampers the identification of prior austenite grains, see Fig. 2b. Particularly smaller grains, which may often serve as important indicators of the recrystallization stage of the material, are clearly defined by the electrolytic etching technique

niveaus aufgelöst werden. Im Anschluss an die elektrolytische Ätzung wurde die Probe zusätzlich mit 1 µm Diamantsuspension erneut leicht überpoliert.

Als Referenz zum Vergleich wurden ergänzend zu den elektrolytischen Ätzungen Pikrinsäureätzungen durchgeführt. Die Proben der Vergleichsätzungen wurden metallographisch gleich aufbereitet und bei Raumtemperatur für ca. 45 s geätzt. Die Ätzlösung besteht dabei aus 100 ml kaltgesättigter Pikrinsäure auf Wasserbasis, 20 ml WAC Netzmittel der Firma Compard KG als Benetzungsmittel und 20 ml HCl (37 vol.%).

Die EBSD Untersuchungen wurden an einem Rasterelektronenmikroskop vom Typ Auriga 40 der Firma Zeiss, mit einer Hikari Super EBSD Kamera von EDAX durchgeführt. Es wurde eine Beschleunigungsspannung von 20 keV und eine Schrittweite von 300 nm zur lateralen Auflösung verwendet. Die Auswertung der Daten erfolgte mit dem Programm EDAX Orientation Imaging Micrograph (OIM) Analysis 8.

3. Ergebnisdiskussion

Um das Ergebnis der zuvor beschriebenen Ätzungen darzustellen, wurden in dieser Arbeit lichtmikroskopische Bilder von den geätzten Proben aufgenommen und EBSD-Aufnahmen gegenübergestellt.

Bild 2a zeigt das Ergebnis der elektrolytischen Ätzung für den unausgelagerten Zustand des Werkstoffs PH15-5 . Es ist eine deutliche Darstellung von ehemaligen Austenitkorngrenzen ohne Anzeichen auf einen Angriff von Zwillingsgrenzen oder der martensitischen Substruktur erkennbar. Die Vergleichsätzung auf Pikrinsäurebasis zeigt dagegen in Bild 2b eine ausgeprägte, martensitische Struktur, welche die Identifizierung von ehemaligen Austenitkörnern deutlich erschwert. Gerade kleinere Körner, die oft wichtige Hinweise auf das Rekristallisationsstadium des Werkstoffes liefern können, sind durch die präsentierte, elektro-

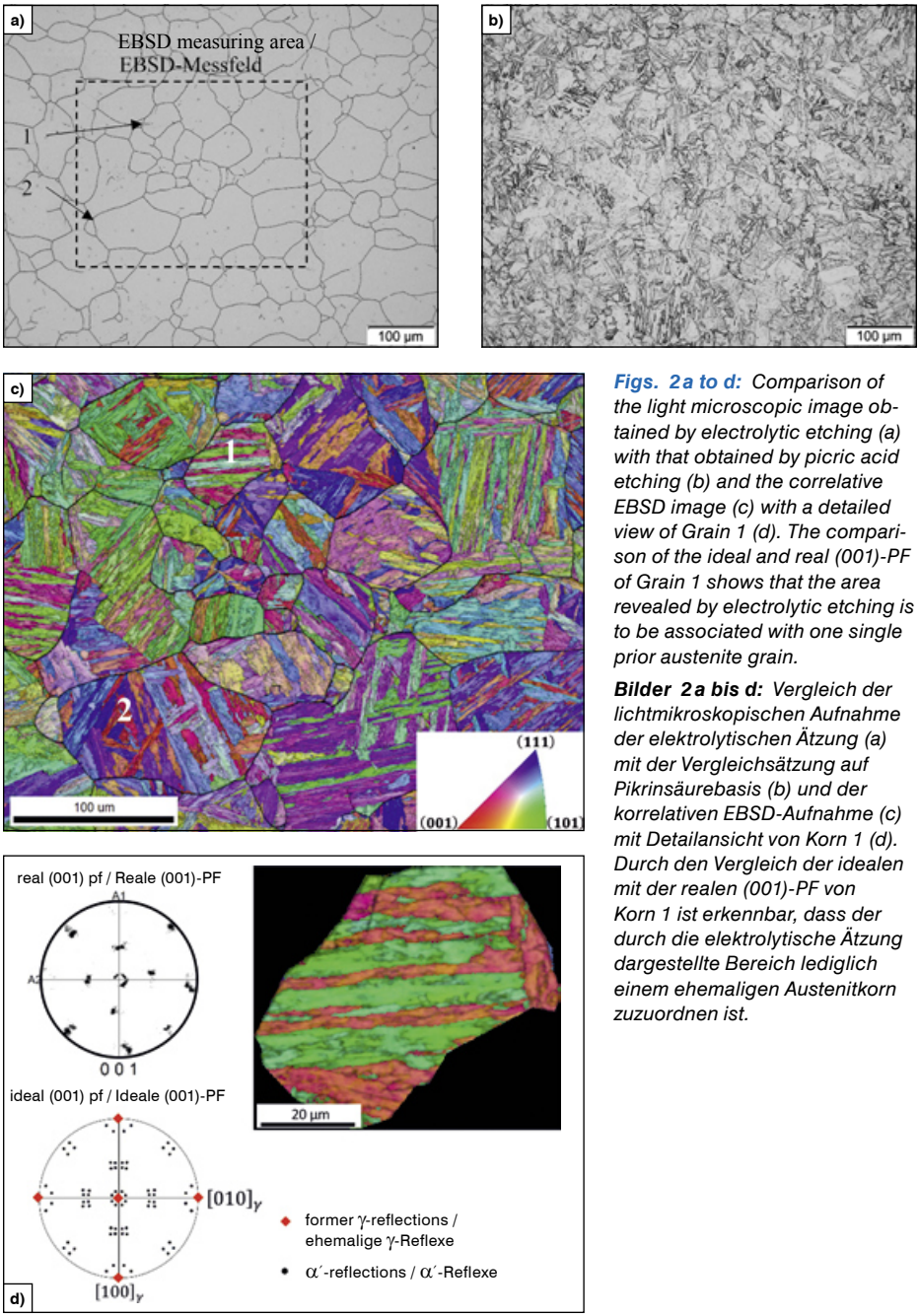

Figs. 2a to d: *Comparison of the light microscopic image obtained by electrolytic etching (a) with that obtained by picric acid etching (b) and the correlative EBSD image (c) with a detailed view of Grain 1 (d). The comparison of the ideal and real (001)-PF of Grain 1 shows that the area revealed by electrolytic etching is to be associated with one single prior austenite grain.*

Bilder 2a bis d: *Vergleich der lichtmikroskopischen Aufnahme der elektrolytischen Ätzung (a) mit der Vergleichsätzung auf Pikrinsäurebasis (b) und der korrelativen EBSD-Aufnahme (c) mit Detailansicht von Korn 1 (d). Durch den Vergleich der idealen mit der realen (001)-PF von Korn 1 ist erkennbar, dass der durch die elektrolytische Ätzung dargestellte Bereich lediglich einem ehemaligen Austenitkorn zuzuordnen ist.*

presented in this work (Fig. 2a). Due to residues of the martensitic microstructure when using picric acid as an etchant, the prior austenite grain size appears generally finer than is the case with electrolytic etching so that a lower value may be determined when grain size evaluation is carried out.

Verification of this etching was achieved by means of EBSD measurement on the positions marked in Fig. 2a. The verification process also provided information as to the completeness of the reconstructed austenite grain boundaries. A detailed analysis will be conducted on two grains, which are representative of the polished surface. The grains are also marked in Fig. 2a. The result of EBSD measurement is shown in Fig. 2c as an Inverse Pole figure (IPF) and Image Quality (IQ) map. Based on this image, individual grains may be evaluated according to the mapped interfaces revealed by electrolytic etching using the evaluation software OIM. From the defined pattern in pole figures of martensitic structures, which forms due to a strict orientation relationship between austenite (γ) and martensite (α') [10–13], conclusions may be drawn as to whether the investigated area is to be associated with one or several austenite grains. For this purpose, a presumed grain is cut out and its (001)-PF is rotated so that the pattern may be compared with that of an ideal pole figure. Fig. 2d shows the cut-out area of Grain 1 as an IPF and IQ map with the correspondingly rotated (001)-PF showing α' reflections in comparison with the ideal (001)-PF. The ideal PF shows the orientation relationship according to Kurdjumov-Sachs (KS) between the prior γ (red squares) and α' projection points (black dots) of {100} planes. As the measured pole figure compared with the ideal PF does not contain any additional α' reflections, this evaluation method is able to prove that the electrolytically and slightly etched grain which is presented in this work is in fact a prior austenite grain.

lytische Ätzung sauber abgegrenzt (Bild 2a). Durch die Rückstände der martensitischen Mikrostruktur bei der Pikrinsäureätzung erscheint die ehemalige Austenitkorngröße im Allgemeinen feiner als bei der elektrolytischen Ätzung und kann somit zu einem geringeren Wert in der Korngößenauswertung führen.

Eine Verifizierung der Ätzung über eine EBSD Messung an der in Bild 2a markierten Position, liefert Aufschluss über die Vollständigkeit der dargestellten Austenitkorngrenzen. Die Detailauswertung wird an zwei für die Schliffläche repräsentativen Körnern gezeigt, die auch in der Bild gekennzeichnet sind. Das Ergebnis der EBSD Messung wird in Bild 2c anhand der inversen Polfigur (IPF) und der Image Quality (IQ) dargestellt. Auf Grundlage dieser Aufnahme können einzelne Körner nach den dargestellten Grenzflächen der elektrolytischen Ätzung mit der Auswertesoftware OIM ausgewertet werden. Vom definierten Muster in Polfiguren martensitischer Strukturen, das aufgrund einer strikten Orientierungsbeziehung zwischen Austenit (γ) und Martensit (α') entsteht [10–13], können Rückschlüsse gezogen werden, ob der betrachtete Bereich zu einem oder mehreren Austenitkörnern gehört. Dazu wird ein vermeintliches Korn ausgeschnitten und dessen (001)-PF so rotiert, dass ein Vergleich des Musters mit einer idealen Polfigur erfolgen kann. Bild 2d zeigt den ausgeschnittenen Bereich des Korns 1 als IPF- und IQ-Darstellung mit der dazugehörenden rotierten (001)-PF der α'-Reflexe im Vergleich zur idealen (001)-PF. Die ideale PF stellt die Orientierungsbeziehung nach Kurdjumov-Sachs (KS) zwischen den ehemaligen γ (rote Quadrate) und α'-Projektionspunkten (schwarze Punkte) der {100}-Ebenen dar. Da die gemessene Polfigur im Vergleich zur idealen PF keine zusätzlichen α'-Reflexe beinhaltet, kann mit Hilfe dieser Auswertemethodik nachgewiesen werden, dass das in dieser Arbeit dargestellte elektrolytisch angeätze Korn tatsächlich ein ehemaliges Austenitkorn ist.

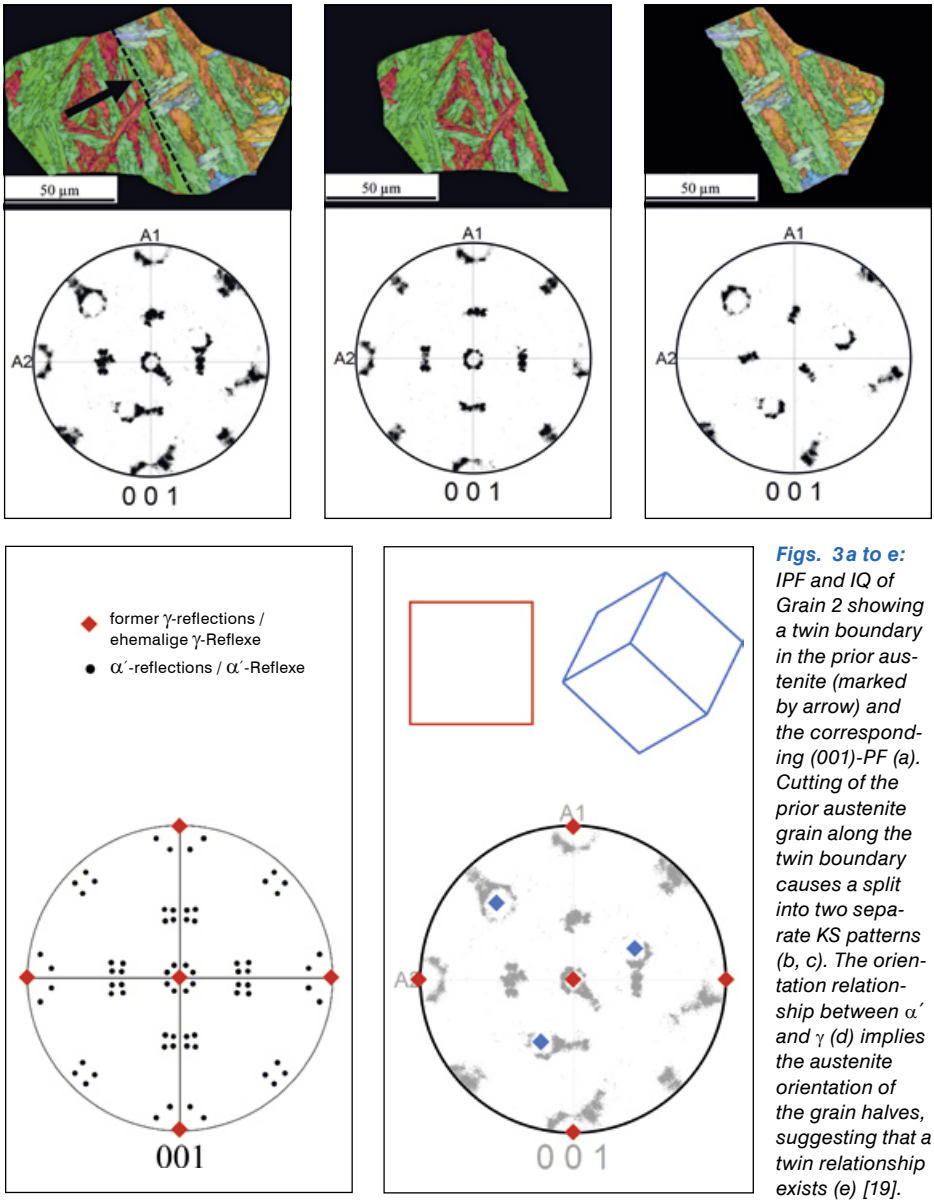

Figs. 3a to e: *IPF and IQ of Grain 2 showing a twin boundary in the prior austenite (marked by arrow) and the corresponding (001)-PF (a). Cutting of the prior austenite grain along the twin boundary causes a split into two separate KS patterns (b, c). The orientation relationship between α´ and γ (d) implies the austenite orientation of the grain halves, suggesting that a twin relationship exists (e) [19].*

Bilder 3a bis e: *IPF und IQ von Korn 2 mit der Kennzeichnung einer Zwillingsgrenze im ehemaligen Austenit (mit Pfeil markiert) und der dazugehörenden (001)-PF (a). Ein Zerschneiden des ehemaligen Austenitkorns entlang der Zwillingsgrenze bewirkt eine Aufspaltung in zwei separate KS-Muster (b, c). Aufgrund der Orientierungsbeziehung zwischen α´ und γ (d) kann auf die Austenitorientierung der beiden Kornhälften geschlossen werden, welche auf eine Zwillingsbeziehung hindeuten (e) [19].*

Further conclucions may be drawn from EBSD analyses with regards to prior twin boundaries in the austenitic grains. Fig. 3a, for example, shows a grain with a superimposed KS pattern (Grain 2). Upon closer inspection, 2 complete KS patterns which are displaced relative to each other by a certain angle (Fig. 3b, c) may be identified. It may be assumed that there is a strict orientation relationship between a´ and γ, as shown in Fig. 3d by an ideal KS pattern in the (001)-PF, thus implying the orientation of the prior austenite. The deduced orientation of the austenite is shown in Fig. 3e by means of a schematic drawing of the unit cell and the corresponding projection points in a (001)-PF. As originally proved by Blewitt et al. [19], the relationship of those two orientations within the prior austenite grain suggests a twin relationship. This means that the analyzed grain also contained twins which could not be identified in the electrolytically etched sample, however. As this was also the case with other grains in this material, it may be assumed that the presented two-step etching technique slightly etches only prior austenite grain boundaries and that twin boundaries as well as lath boundaries are not considered. This facilitates the evaluation of the prior austenite grain size according to many standards (e. g. ASTM E112) as those have to ignore twin boundaries.

4. Acknowledgements

We would like to express our special thanks to the Austrian Research Promotion Agency (FFG, Österreichische Forschungsfördergesellschaft) and to our partners *Böhler Schmiedetechnik GmbH & Co KG* and *Böhler Edelstahl GmbH und Co KG* for funding this work. We would also like to thank the *Materials Center Leoben Forschung GmbH* for the resources made available to us.

Des weiteren können EBSD Untersuchungen Aufschlüsse zu ehemaligen Zwillingsgrenzen in den austenitischen Körnern geben. Bild 3a zeigt beispielsweise ein Korn mit überlagertem KS-Muster (Korn 2). Bei genauerer Betrachtung kann erkannt werden, dass es sich um 2 vollständige KS-Muster handelt, die zueinander um einen bestimmten Winkel verschoben sind (Bild 3b, c). Kann davon ausgegangen werden, dass es eine strikte Orientierungsbeziehung zwischen a´ und γ gibt, wie in Bild 3d anhand eines idealen KS-Musters in der (001)-PF gezeigt wird, so lässt sich auf die Orientierung des ehemaligen Austenits schließen. Bild 3e zeigt die daraus abgeleiteten Orientierungen des Austenits anhand schematischer Skizzen der Einheitszelle und den dazugehörenden Projektionspunkten in einer (001)-PF. Wie ursprünglich von Blewitt et al. [19] nachgewiesen, deutet dieses Verhältnis der beiden Orientierungen innerhalb des ehemaligen Austenitkorns auf eine Zwillingsbeziehung hin. Dies bedeutet, dass das untersuchte Korn ebenfalls Zwillinge beinhaltete, allerdings in der elektrolytisch geätzten Probe diese nicht identifiziert werden konnten. Da dies auch bei anderen Körnern in diesem Material festgestellt wurde, kann somit davon ausgegangen werden, dass anhand der präsentierten zweistufigen Ätzmethode nur die ehemaligen Austenitkorngrenzen angeätzt und Zwillingsgrenzen sowie Lattengrenzen nicht berücksichtigt werden. Dies erleichtert die Auswertung der ehemaligen Austenitkorngröße nach vielen Normungsstandards (z. B. ASTM E112), da in diesen die Zwillingsgrenzen ignoriert werden müssen.

4. Danksagung

Besonderer Dank gilt der österreichischen Fördergesellschaft (FFG) und den Partnern Böhler Schmiedetechnik GmbH & Co KG und Böhler Edelstahl GmbH und Co KG für die Finanzierung dieser Arbeit sowie dem Materials Center Leoben Forschung GmbH für die uns zur Verfügung gestellten Ressourcen.

References / Literatur

[1] Habibi Bajguirani, H. R.: Mater. Sci. Eng. A 338 (2002), 142–159
DOI: 10.1016/S0921-5093(02)00062-X

[2] Yu, Q.; Dong, C. F.; Liu, Z.B.; Liang, J. X.; Xiao, K.; Li, X. G.: Int. J. Electrochem. Sci. 10 (2015) 3, 2035–2044

[3] Cayron, C.; Artaud, B.; Briottet, L.: Mater. Charact. 57 (2006) 4–5, 386–401
DOI: 10.1016/j.matchar.2006.03.008

[4] Miyamoto, G.; Iwata, N.; Takayama, N.; Furuhara, T.: Acta Mater. 58 (2010) 19, 6393–6403

[5] Germain, L.; Gey, N.; Mercier, R.; Blaineau, P.; Humbert, M.: Acta Mater. 60 (2012) 11, 4551–4562
DOI: 10.1016/j.actamat.2012.04.034

[6] Soshina, T. V.; Zisman, A. A.; Khlusova, E. I.: Metallurgist 57 (2013) 1–2, 128–136
DOI: 10.1007/s11015-013-9702-4

[7] San Martin, D.; Rivera Diaz del Castillo, P. E. J.; Peekstok, E.; van der Zwaag, S.: Mater. Charact. 58 (2007) 5, 455–460
DOI: 10.1016/j.matchar.2006.06.009

[8] Vander Voort, G. F.: Metallography: Principles and practice, 4. Auflage, McGraw Hill, New York, USA, 1999, S. 171 ff.

[9] Baldwin, W.: Metallography and Microstructures 2004 ASM, 9. Auflage, ASM International, Materials Park, USA, 2004, S. 693ff

[10] Cho, K. S.; Sim, H. S.; Kim, J. H.; Choi, J. H.; Lee, K. B.; Yang, H. R.; Kwon, H.: Mater. Charact. 59 (2008) 6, 786–793
DOI: 10.1016/j.matchar.2007.06.013

[11] Mirzadeh, H.; Najafizadeh, A.: ISIJ Int. 53 (2013) 4, 680–689
DOI: 10.2355/isijinternational.53.680

[12] Beckert, M.; Klemm, H.: Handbuch der Metallographischen Ätzverfahren, 4. Auflage,VEB Deutscher Verlag für Grundstoffindustrie, Leipzig, Deutschland, 1984, S. 43ff

[13] Kauczor, E.: Werkstattbücher - Metallographische Arbeitsverfahren, 1. Auflage, Springer-Verlag, Berlin / Göttingen / Heidelberg, 1957, S. 39ff

[14] Bell, F.C.; Sonon, D.E.: Metallography 9 (1976) 2, 91–107
DOI: 10.1016/0026-0800(76)90008-2

[15] Couturier, L.; De Geuser, F.; Descoins, M.; Deschamps, A.: Mater. Des. 107 (2016), 416–425
DOI: 10.1016/j.matdes.2016.06.068

[16] Abbasi, M.; Wie, L. Y.; Nelson, T.W.: Mater. Sci. Technol. Conf. Exhib. 2009, in: Materials Science and Technology, 2009, Curran Associates Inc., Red Hook, 2010

[17] Kitahara, H.; Ueji, R.; Tsuji, N.; Minamino, Y.: Acta Mater. 54 (2006) 5, 1279–1288
DOI: 10.1016/j.actamat.2005.11.001

[18] Nambu, S.; Shibuta, N.; Ojima, M.; Inoue, J.; Koseki, T.; Bhadeshia, H. K. D. H.: Acta Mater. 61 (2013) 13, 4831–4839
DOI: 10.1016/j.actamat.2013.04.065

[19] Blewitt, T. H.; Coltman, R. R.; Redman, J. K.: J. Appl. Phys. 28 (1957) 6, 651–660

Bibliography

DOI 10.3139/147.110497
Pract. Metallogr. 55 (2018) 12; page 800–812

ISSN 0032–678X

Dominik Brandl

graduated at Montanuniversität Leoben, Department Physical Metallurgy and Materials Testing, in 2015. Currently, he is working at the Materials Center Leoben Forschung GmbH on his Ph.D. thesis dealing with structure-property relations of martensitic steels.

Lukas Höfler

is studying materials science at Montanuniversität Leoben since October 2014. He is working as an assistant student with focus on metallographic preparation and grain size analysis at the Materials Center Leoben Forschung GmbH.

Publication B

Evidence of austenite memory in PH 15-5 and assessment of its formation mechanism

D. Brandl, M. Lukas, M. Stockinger, S. Ploberger, G. Ressel

Materials and Design 176 (2019) 107841

Contents lists available at ScienceDirect

Materials and Design

journal homepage: www.elsevier.com/locate/matdes

Evidence of austenite memory in PH 15-5 and assessment of its formation mechanism

Dominik Brandl [a,*], Marina Lukas [a], Martin Stockinger [b,1], Sarah Ploberger [c], Gerald Ressel [a]

[a] Materials Center Leoben Forschung GmbH (MCL), 8700 Leoben, Austria
[b] voestalpine Böhler Aerospace GmbH & Co KG, A-8605 Kapfenberg, Austria
[c] voestalpine Böhler Edelstahl GmbH & Co KG, A-8605 Kapfenberg, Austria

HIGHLIGHTS

- A diffusion controlled transformation from martensite to austenite is evidenced.
- Austenite memory is directly evidenced in PH 15-5.
- Inheritance of low angle grain boundaries from martensite to austenite is proposed.

GRAPHICAL ABSTRACT

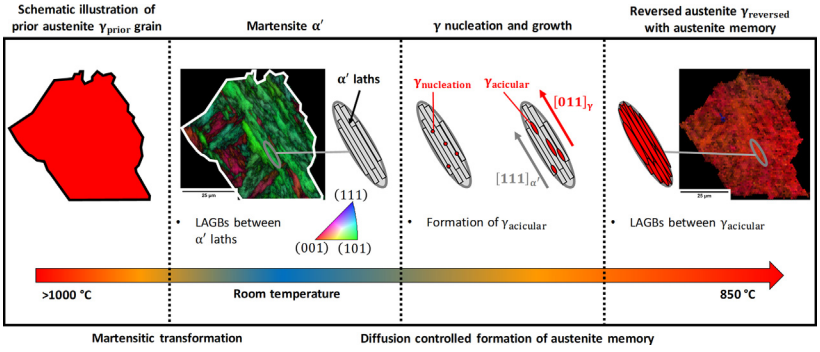

ARTICLE INFO

Article history:
Received 18 February 2019
Received in revised form 24 April 2019
Accepted 7 May 2019
Available online xxxx

Keywords:
Supermartensitic stainless steel
Austenite memory
Reversed austenite
Phase transformation
In-situ characterization
High temperature electron backscatter diffraction

ABSTRACT

Austenite memory and subsequent spontaneous recrystallization during austenitization is stated for some types of soft martensitic stainless steels such as X4CrNiMo16-5-1 or 13Cr—5Ni but have not been proposed for the commercial alloy PH15-5 until now. However, the understanding of the austenitization behavior is defined to be crucial as it influences grain size, dislocation density of austenite and thus the final mechanical properties of the material.

Therefore, this study investigates the austenitization behavior of PH15-5 by means of *in-situ* high temperature electron back scatter diffraction of continuous austenitization and directly evidences austenite memory also in this alloy. In order to characterize the austenite formation mechanism in detail, dilatometer, *in-situ* X-ray diffraction and confocal laser scanning microscope experiments have been carried out. Corroborated with thermokinetic DICTRA simulations, a diffusion controlled transformation exhibiting austenite memory is evidenced. The *in-situ* high temperature electron backscatter diffraction data in comparison with recent literature indicates the inheritance of geometrically necessary dislocations from martensite to austenite. Therefore, a basic model is postulated in order to describe the inheritance of geometrically necessary dislocations due to a diffusion controlled transformation process.

* Corresponding author.
E-mail addresses: Dominik.Brandl@mcl.at (D. Brandl), Marina.Lukas@mcl.at (M. Lukas), Martin.Stockinger@unileoben.ac.at (M. Stockinger), Sarah.Ploberger@bohler-edelstahl.at (S. Ploberger), Gerald.Ressel@mcl.at (G. Ressel).
[1] Present address: Montanuniversität Leoben, Department Product Engineering, A-8700 Leoben, Austria.

https://doi.org/10.1016/j.matdes.2019.107841

1. Introduction

The corrosion resistant and precipitation hardenable steel alloy PH 15-5 combines high strength with good toughness properties and therefore, is used *e.g.* as structural component in aerospace industry. The microstructure consists of lath martensitic matrix with nanometer sized bulk precipitates consisting of Cu [1,2]. PH 15-5 exhibits a Ni/Cr ratio of 0.34 and the carbon content of approximately 0.03 m.-% is predominately precipitated as NbC, which hinders austenite grain coarsening during solution annealing [3]. Generally, controlling the austenite microstructure and therefore, the evolving martensitic substructure is a potential method to tailor strength and toughness of various types of steels [4–13]. However, the austenitization of martensitic Fe-Ni-Cr alloys often shows effects such as a so-called austenite memory which leads to a similar size, shape and orientation of prior and reversed austenite [14–23]. Thus, *ex-situ* examination of prior austenite microstructure is challenging for martensitic steel with high purity and corrosion resistance such as PH 15-5 [24]. For the austenite memory phenomenon, four different formation mechanisms are reported in literature: diffusionless shear transformation [22], variant restriction between reversed austenite, cementite and martensitic laths [16,25], diffusional growth of retained austenite [20,26] and variant restriction between martensitic laths and reversed austenite influenced by an internal stress field [19]. Diffusionless transformations from martensite to austenite is promoted by high heating rates, low carbon content and a high Ni/Cr ratio (*i.e.* low A_1 and A_3 temperatures) [15,27–29]. Tomimura et al. [29] observed diffusionless transformation from martensite to austenite in a metastable austenitic alloy for a Ni/Cr ratio of 0.63. Investigations of Shirazi and Nakada et al. [18,22] on binary iron-nickel alloys suggested austenite memory caused by diffusionless shear-transformation for Ni contents above 18 m.% and without Cr. However, more closely related to PH 15-5 are soft martensitic stainless steels, *i.e.* martensitic steels with 11.5–16 m.% Cr, 4–8 m.% Ni and a carbon content <0.07 m.% [17] but without Cu as precipitating element. Owing to the higher Cr content compared to binary Fe—Ni alloys, A_1 and A_3 temperatures are raised and diffusional martensite to austenite transformation gets favorable [17]. According to Liu et al. [20] the presence of inter-lath retained austenite in soft martensitic steels supports a diffusional transformation mechanism because no nucleation of reversed austenite is needed. However, Nakada et al. [19] postulated a diffusion controlled mechanism for austenite memory without the presence of carbides or retained austenite in a 13Cr—6Ni soft martensitic steel. It is claimed that austenite nucleates at martensite lath-boundaries with Kurdjumov - Sachs (KS) orientation relationship (OR) and grows in a specific direction due to crystallographic restrictions and internal stress fields induced by martensitic transformation. This mechanism is also reported by Shinozaki et al. [30,31] for low alloy steel with a low heating rate of 0.05 °C/s. The commercial steel alloy PH 15-5 distinguishes from soft martensitic steels by Cu precipitations inside martensitic laths and austenite memory phenomenon during continuous austenitization of PH 15-5 is so far not reported in literature. Moreover, most of the prior discussed publications used *ex-situ* analysis of inter-critical annealing experiments in order to investigate austenite memory and its crystallographic OR of soft martensitic steel.

The scope of the recent work is, thus, the direct evidence of the austenite memory phenomenon for the commercial alloy PH 15-5 during a continuous austenitization and an assessment of its formation mechanism. Therefore, *in-situ* high temperature techniques such as dilatometry, X-ray diffraction (XRD) experiments, Confocal Laser Scanning Microscopy (CLSM) and Electron Backscatter Diffraction (EBSD) during continuous austenitization were carried out and evaluated. Furthermore, in order to investigate the diffusional type of austenite formation the transformation was simulated by thermokinetic calculations, compared to experimental findings and assessed in the following.

2. Experimental procedure

2.1. Material

The investigated steel alloy PH15-5 was produced by voestalpine Böhler Edelstahl GmbH with the chemical composition given in Table 1. After casting the ingot was remelted in vacuum and subsequently forged.

The investigated material condition is the as-forged condition in order to analyze the continuous austenitization behavior during solution annealing. XRD measurements of the as-forged material condition at room temperature exhibit no retained austenite (Fig. 1a). Additional reflexes ($(002)_{Mo}$,$(112)_{Mo}$) in the XRD pattern originate from the molybdenum heating band and are, thus, not further considered. Fig. 1b shows a transmission electron microscope bright-field image of martensitic laths of PH 15-5 after solution annealing at 1030 °C for 30 min and aging at 560 °C for 4 h with highlighted lath boundaries and lath widths ranging between 60 and 300 nm. The findings concerning retained austenite fraction and martensite lath width are used for subsequent thermokinetic calculations. Dilatometry measurements of the austenitization process with continuous heating to 1030 °C and a heating rate of 3.3 °C/s exhibit an A_{c1} temperature of 719 °C and an A_{c3} temperature of 837 °C.

2.2. Investigation methods

Dilatometer measurements of austenitization with heating steps at 730 °C and 850 °C and a heating rate of 3.3 °C/s were carried out in a TA instruments DIL 805L/A dilatometer. For measurements the cylindrical specimens with a diameter of 4 mm and a length of 10 mm were fixed in Al_2O_3 rods. Temperature control was ensured by a type S thermocouple mounted on the surface in the middle of the specimen by spot welding.

Cr-Kα radiation was used for *in-situ* high temperature X-ray diffraction (XRD) experiments on a Bruker D8 Advance goniometer with a Mo heating band. The specimens in the size of $20 \times 10 \times 1\ mm^3$ were heated to 850 °C with a heating rates of 0.33 °C/s, 3.3 °C/s and 33 °C/s and held for 1000 s. For the determination of the austenite fraction, peaks were fitted by means of a Pseudo-Voigt profile and a quotient of integrated intensities of austenite (111) and ferrite (110) peak with R-values of 77.2 and 105 cm^{-6}, respectively [32].

In order to underpin experimental results of austenitization behavior, DICTRA simulations were carried out using the thermodynamic database TCFE8 and the diffusion database Mob2. A comprehensive description of DICTRA's basic models is given in Ref. [33]. In present simulations a Fe-Cr-Ni alloying system is considered with 15.0 m.% Cr, 5.1 m.% Ni and balanced Fe. A planar 2-phase-system was defined with moving boundary consisting of a bcc phase (denoted as active in the DICTRA script) for martensite and an fcc phase attached to martensite, which should nucleate during simulation with a nucleation barrier of $1e^{-5}$ J/mol (denoted as inactive in the DICTRA script). The simulation started at 580 °C with heating rates of 0.33, 3.3 and 33 °C/s to 850 °C and subsequent isothermal holding for 1000 s which are the same heat treatment parameters as in the *in-situ* high temperature XRD measurements. A diffusion enhancement of 5 is applied on the martensitic phase because of a higher dislocation density and therefore higher diffusion rate compared to the ferritic phase [17,34,35]. As martensite lath boundaries are assumed as nucleation sites for austenite, the size of the cell was set to 100 nm, which originates from one half of a

Table 1
Chemical composition of PH 15-5 in m.%.

C	Si	Mn	Cr	Ni	Cu	Nb	N
0.032	0.29	0.54	15.01	5.10	3.21	0.27	0.013

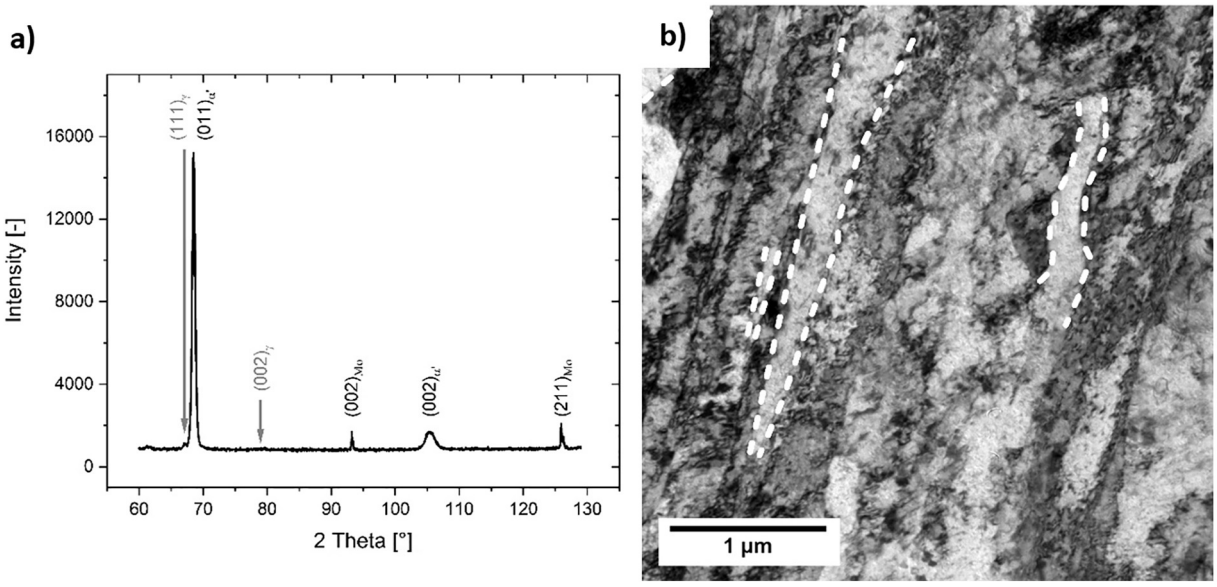

Fig. 1. XRD analysis of the as-forged material condition with no additional heat treatment exhibit no retained austenite is observable (a). Transmission electron microscope bright field image of PH15-5 lath martensitic structure after solution annealing at 1030 °C for 30 min and subsequent aging at 560 °C for 4 h with highlighted lath boundaries in dashed lines (b).

martensite lath width found by transmission electron microscopy investigations of PH 15-5 presented in Fig. 1b.

CLSM measurements were performed in argon atmosphere heated in an infrared heating stage with a heating rate of 3.3 °C/s [36]. For these investigations specimens were prepared in dimensions of 5 × 6 × 0.5 mm^3 by mechanically grinding and finished with a 1 μm diamond suspension polish.

In-situ high temperature observations of crystal orientation during austenitization were performed by EBSD on a scanning electron microscope JSM-7001F with field emission gun (FEG-SEM) equipped with an EDAX/OIM system version 7.1 with DigiView detector from TSL Solutions KK. Stepped heating were carried out by a second-generation high temperature heating stage HSEA-100 from TSL solution KK. The stepped heat treatment for *in-situ* high temperature EBSD measurements involved: Heating from room temperature to 730 °C with a heating rate of 3.3 °C/s, holding for 8 min at this temperature, subsequently heating to 850 °C with the same heating rate, followed by holding for 5 min. EBSD samples exhibited dimensions of 5 × 6 × 0.5 mm^3 and were prepared by mechanically grinding and polishing with a 0.02 μm acidic alumina suspension in the final step. For room temperature and high temperature EBSD measurements, step sizes of 300 nm and 1 μm are chosen, respectively. On the generated EBSD data a grain dilation cleanup is applied with a grain tolerance angle of 5° and a minimum grain size of 4 pixel with the software Orientation Imaging Micrograph (OIM) 7 from EDAX in order to reduce noise of the measurement. The reconstruction of prior austenite orientation of the original martensitic crystal orientation shown in Fig. 2d was carried out with the reconstruction algorithm of Nyyssönen et al. [37] with an inflation power of 1.4 and the MTEX Toolbox 5.1.1 in the MatLab version R2018a.

3. Results

3.1. Orientation memory of freshly formed austenite in the PH15-5 alloy

In order to analyze the crystal orientation of reversed austenite in respect to prior austenite and martensite *in-situ* high temperature EBSD measurements during a continuous austenitization treatment were carried out.

Fig. 2a–c show EBSD measurements of the same position at room temperature, 730 °C and 850 °C, respectively. In order to compare those crystal orientations Fig. 2a is illustrated as an inverse pole figure (IPF) color coding of the martensitic phase, Fig. 2b is illustrated as an IPF color coding of the austenitic phase and Fig. 2c contains an additional overlap of the image quality (IQ) and IPF for the austenitic phase. Grain boundaries with a misorientation angle >15° are calculated and illustrated in Fig. 2b–d. While Fig. 2a (room temperature) shows a fully martensitic microstructure, Fig. 2b and c show an austenite fraction of 0.94 and 0.98, respectively. Latter fact of austenite content indicates a time dependent martensite to austenite transformation and therefore a diffusion controlled mechanism as further heating from 730 °C to 850 °C raises the austenite fraction to 0.98.

Despite an austenitization temperature of 730 °C near A_{c1}, EBSD investigations show an austenite fraction of 0.94 which may be attributed to a delay of about 60 to 100 s between reaching the temperature and start measuring.

Comparing Fig. 2a–c an akin grain structure is already obvious, especially for the encircled grain (solid line) in martensite (Fig. 2a). Furthermore, comparing Fig. 2a with Fig. 2c the highlighted areas (dashed lines) reveal a structure in IQ of reversed austenite which is parallel to martensitic block structure at room temperature. It is remarkable that the IQ in Fig. 2c exhibit fluctuations inside the austenite grains which gives evidence for discontinuities inside the austenite microstructure.

In order to verify the presence of austenite memory, additionally to the EBSD of the reversed austenite a reconstruction of the prior austenite grain structure from the original martensitic microstructure (Fig. 2a) is calculated and shown in Fig. 2d. Comparing the grain size and shape of the reconstructed prior austenite grains (Fig. 2d) and that of the freshly formed austenite (Fig. 2b and c) reveals an almost identical grain structure for prior and reversed austenite. Furthermore, the OR between martensite and reversed austenite for an exemplarily austenite grain (highlighted in Fig. 2a and c with solid lines) is shown in Fig. 2e with a (001) pole figure. The reflexes of martensite and reversed austenite show a near KS-OR with reflexes of austenite inside circles of martensite reflexes which is a characteristic appearance of (001) pole figures showing KS-OR. Therefore, by these results it can be stated that the fresh formed reversed austenite shows the same crystal orientation than the prior austenite and in combination with

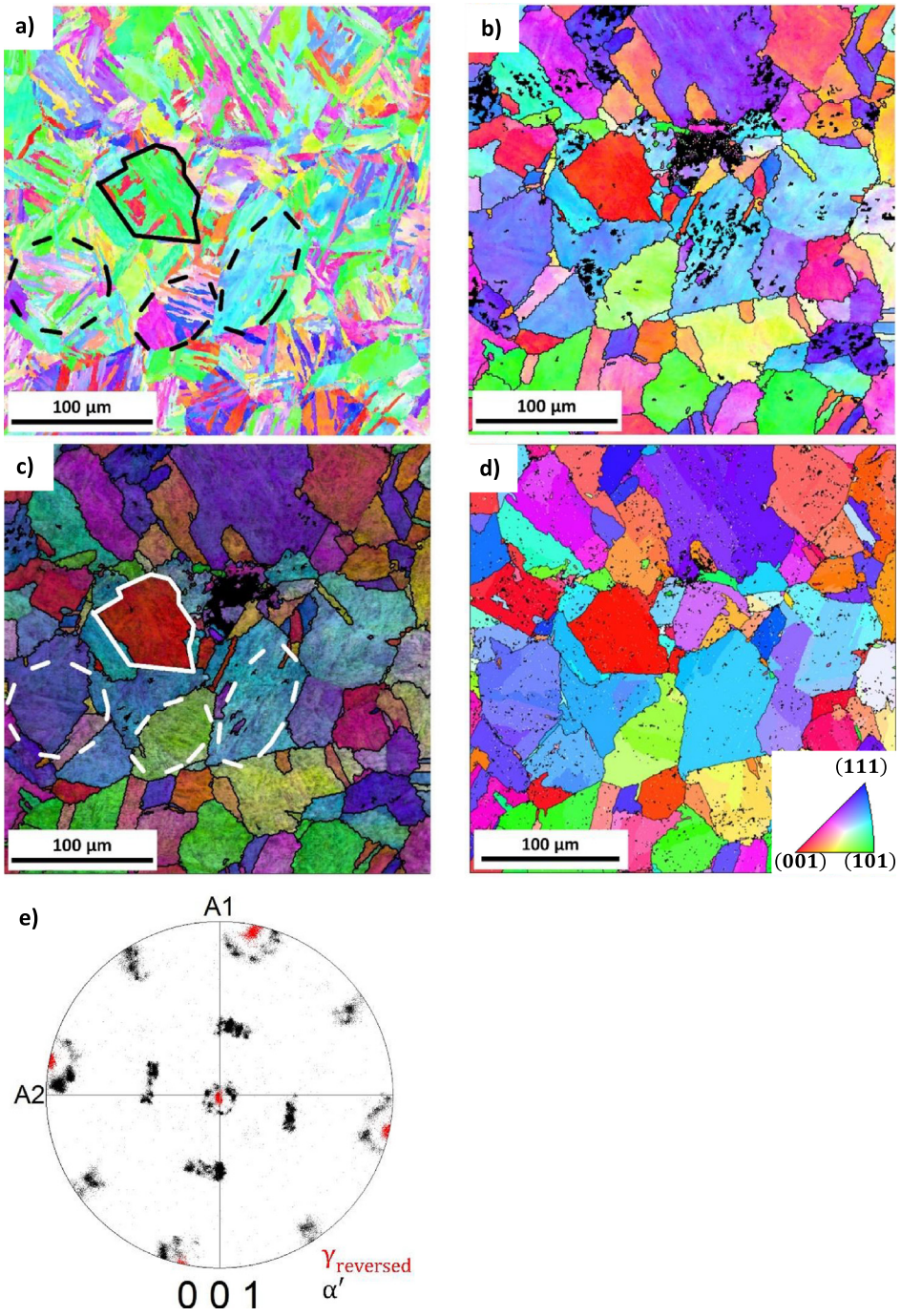

Fig. 2. EBSD measurements of martensitic microstructure are illustrated with IPF color coding at room temperature before heating (a), of freshly formed austenite at 730 °C (b) and 850 °C with additional overlap of the IQ (c). A comparison of the reconstructed prior austenite grains (d) from the martensitic microstructure (a) exhibit the same crystal orientation and grain size for prior and reversed austenite, *i.e.* austenite memory. Additionally, a (001) pole figure with reflexes of martensite and austenite of one exemplary highlighted austenite grain (e) underpin this finding as it shows a near KS-OR. (For interpretation of the references to color in this figure legend, the reader is referred to the web version of this article.)

unchanged grainsize and shape, austenite memory is directly evidenced in the present steel.

3.2. Formation mechanism of austenite reversion

In order to elucidate the formation mechanism of reversed austenite, this work investigates whether the martensite to austenite transformation exhibits a diffusion controlled or a non-diffusional character. Diffusion controlled transformations are time dependent while diffusionless transformations exhibit an athermal behavior with cascade-like transformation steps [22,38]. Therefore, the time dependence of the transformation and the appearance of a surface relief during continuous austenitization are investigated in the following. Furthermore, the findings concerning the formation of reversed austenite are compared to diffusion controlled DICTRA simulations.

3.2.1. Time dependence of austenite reversion

In the present work dilatometer and *in-situ* high temperature X-ray diffraction experiments combined with DICTRA calculations are carried out in order to analyze the time dependence and the transformation mechanism in the commercial PH 15-5 steel that forms austenite memory. A stepped dilatometer heating experiment is performed with the

first step right above A_{c1} at 730 °C and a second step right above A_{c3} at 850 °C. Fig. 3 shows the dilatation and the corresponding temperature as a function of time. At the beginning of the first isothermal holding at A_{c1}, the sample contracts which is caused by the martensite to austenite transformation. Subsequently, the dilatation saturates in a plateau and no further austenite formation is observed. Despite the raised temperature in the second austenitization step, no additional austenite transformation can be detected in dilatation. Therefore, it can be concluded that austenite reversion shows a time dependent transformation behavior in the first austenitization step and no athermal character where martensite to austenite transformation would not proceed with further heating.

In order to get a more detailed information about the influence of the heating rate on the amount of reversed austenite and the time dependence of the transformation, *in-situ* high temperature XRD measurements are performed after continuous heating to 850 °C with heating rates (HR) of 0.33, 3.3 and 33 °C/s. Fig. 4 illustrates *in-situ* measured, reversed austenite fraction against isothermal holding time. The time measurement starts for every heating rate when 850 °C is reached and proceeds during the isothermal holding. Results show that the higher the heating rate, the higher is the amount of reversed austenite at 850 °C. A difference of approximately 10 vol% can be stated between the heating rates of 0.33 and 33 °C/s at the time reaching 850 °C. Additionally, results show a somewhat larger increase of reversed austenite as function of time for specimens heated with lower heating rate. This fact agrees with the findings of dilatometry indicating a strong time dependence of the martensite to austenite transformation and no evidence of an athermal character for a heating rate of 3.3 °C/s. However, while the martensite to austenite transformation seems to be finished at 837 °C by dilatometry, XRD measurements reveal a fraction of 0.92 austenite. This might be explained by a sluggish transformation over a wide temperature range too low for measuring a dilatation by dilatometry.

Furthermore, to validate the findings of dilatometry and XRD measurements and to elucidate the diffusive character of austenite reversion, DICTRA simulations are carried out for different heating rates. The simulation setup is a one dimensional and diffusional move of the martensite/austenite phase boundary with nucleation of austenite at martensite lath boundaries and therefore a diffusional phase transformation (Note: Cu precipitations are not considered in these calculations).

Fig. 5a shows the austenite phase fraction for continuous heating with different heating rates and subsequent isothermal holding. The simulation confirms that higher heating rates lead to higher austenite fraction for continuous heating at 850 °C and agree with results of *in-situ* high temperature XRD measurements. Furthermore, two stages

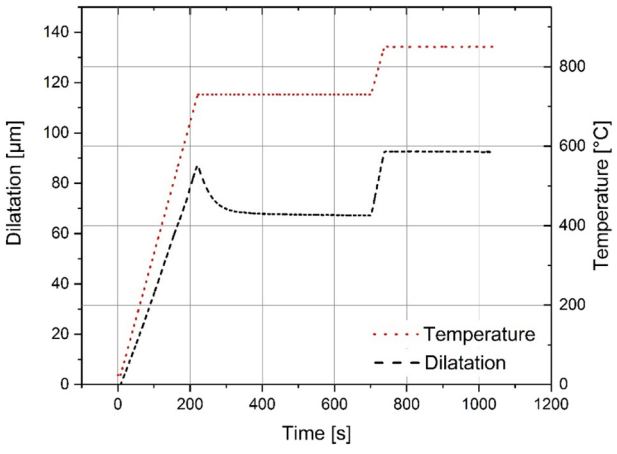

Fig. 3. Dilatation and temperature against time of the implemented dilatation experiments. Austenite formation can be detected at 730 °C and no further transformation at 850 °C.

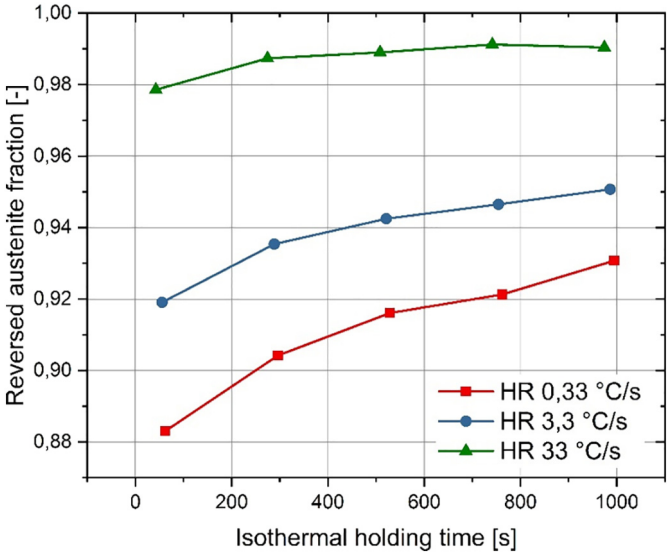

Fig. 4. Amount of reversed austenite during isothermal holding at 850 °C after continuous heating with heating rates of 0.33 °C/s, 3.3 °C/s and 33 °C/s.

with different austenitization behavior are visible and can be differentiated by their transformation rate. For all heating rates the transformation rate of the first stage is higher than of the second stage. It is also demonstrated that lower heating rates result in a lower start temperature for austenite formation and a lower transition temperature between the first and the second transformation stage but retard the finish of the martensite to austenite transformation during continuous heating.

The calculations shown in Fig. 5b yielded that the transformation is linked to a continuous diffusional partitioning of Ni and Cr in the microstructure consisting of martensite and freshly formed austenite for all simulated heating rates. The austenitic phase enriches in Ni and depletes in Cr during the first austenitization stage and homogenize during the second stage. This behavior indicates the formation of a chemically more stable austenite during the first stage of austenitization owing to a higher Ni/Cr ratio compared to the second stage. For low heating rates, such as 0.33 °C/s and 3.3 °C/s, more time for the Ni/Cr partitioning is available and therefore, the partitioning starts at lower temperatures and is more pronounced compared to the heating rate of 33 °C/s. Therefore, lower heating rates exhibit a lower transformation start but a higher transformation finish temperature. The temperatures for the drawn isothermal concentration profiles (712 °C, 745 °C and 850 °C) in Fig. 5b are highlighted in Fig. 5a with grey dashed lines in order to indicate the progress of transformation. Points of discontinuity in the concentration profiles (*i.e.* vertical lines) indicate the martensite/austenite phase boundary.

Concentration profiles of the first austenitization step, *i.e.* 712 °C for all heating rates, indicate diffusion of Ni from martensite to austenite and expulsion of Cr out of the new formed austenite and are shown in solid lines in Fig. 5b. For 745 °C (shown in dashed lines in Fig. 5b) the simulation with a heating rate of 0.33 °C/s has already achieved the second stage of austenitization, whereas the other heating rates are still in stage one. The second austenitization stage is indicated by a horizontal concentration profile line of Ni and Cr in ferrite, *i.e.* the transformation speed is now limited by the diffusion coefficient of austenite instead of martensite [34]. The diffusion coefficient of substitutional alloying elements in austenite is much lower than in martensite and therefore, the transformation rate decreases in the second austenitization stage [34]. For further heating to 850 °C simulations of all heating rates have achieved the second austenitization step and the formation of new austenite is restricted by the diffusional homogenization of Ni and Cr during the subsequent isothermal holding.

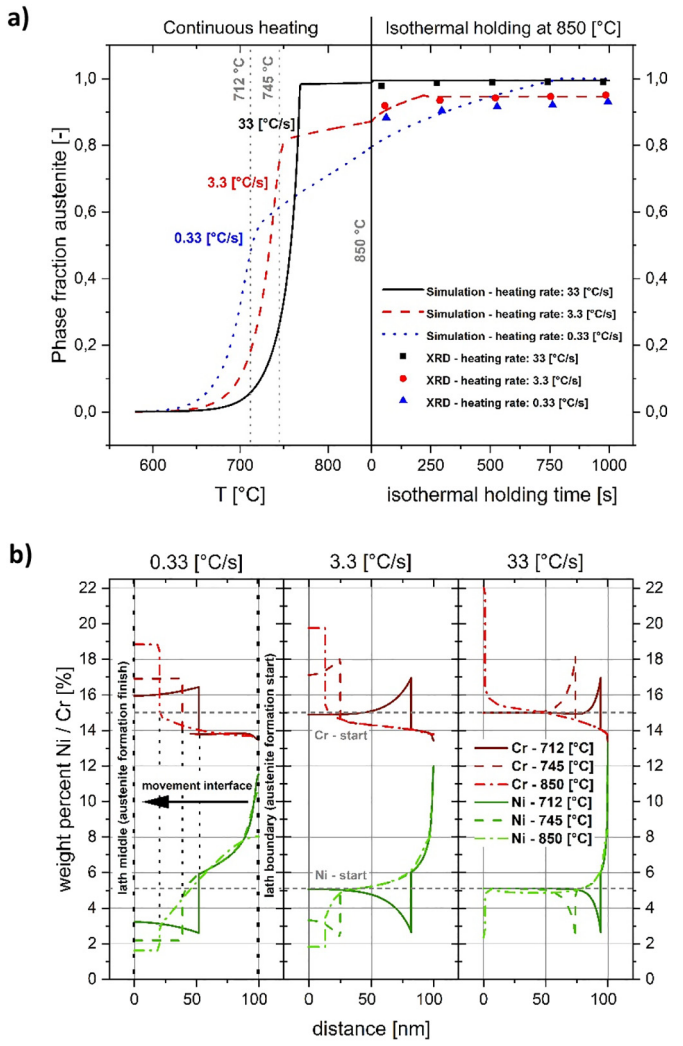

Fig. 5. DICTRA simulated austenite phase fraction for continuous heating and subsequent isothermal holding at 850 °C (a). The simulation results confirm that higher heating rates lead to a higher austenite phase fraction at 850 °C and are validated by *in-situ* high temperature XRD measurements. The corresponding Ni and Cr concentration profiles are given in (b) for the highlighted temperatures 712 °C, 745 °C (grey dashed lines) and 850 °C in (a).

All in all, the thermokinetic calculations evidenced that the experimentally measured austenite fractions can be obtained by diffusional processes supporting prior results that the martensite to austenite transformation is diffusion controlled and time-dependent.

3.2.2. Continuity of the formation of a surface relief

In order to analyze the lateral surface appearance and morphology of the evolving austenite microstructure during continuous austenitization, CLSM observations are carried out. For diffusionless transformations, a cascade-like appearance of a surface relief is reported [22] and therefore the CLSM measurements should give additional information about the austenite formation mechanism.

Fig. 5a–d show the formation of a lath-shaped surface relief (highlighted by dashed lines), with the morphology akin to martensitic microstructures, in the temperature region of austenitization between 500 °C and 850 °C. The appearing surface relief arises continuously at the observed sample surface during heating in the temperature region between A_{c1} and A_{c3}. This is in contrast to the cascade-like appearance of martensitic phase transformations. The simultaneous appearance of the austenite surface relief, additionally gives a hint for a diffusion controlled martensite to austenite transformation. Highlighted areas indicate parallel block structures of martensite (Fig. 5a) and its corresponding surface relief at different temperatures (Fig. 5b–d).

4. Discussion

4.1. Evidence of austenite memory in PH 15-5

In this work, austenite memory is directly evidenced for the first time in the commercial alloy PH 15-5 by *in-situ* high temperature EBSD measurements of austenite crystal orientation and grain size during austenitization at 730 °C and 850 °C. Shirazi et al. [22] also detected the austenite memory phenomenon with *in-situ* high temperature EBSD measurements of binary Fe—Ni alloys with significantly higher Ni contents of 18 and 24 m.% and suggested a martensitic transformation from martensite to austenite because of austenite memory. However, also in other alloys [14–16,19,23,39–42] austenite memory is detected, which all have Ni or Mn as alloying element in common. Zhang et al. [14,16] for example correlated the austenite memory phenomenon in a Fe-2Mn-1.5Si-0.3C alloy predominantly with the formation of acicular austenite (*i.e.* lath-like morphology) which forms, in respect to heating rate and annealing temperature, simultaneously with globular austenite during inter-critical annealing. The investigation of austenite memory after inter-critical annealing is an effective way to analyze the early stages of austenite formation but to evaluate the austenitization treatment itself *in-situ* techniques at higher temperatures are more appropriate. In these references austenite memory have been investigated by means of common approaches such as *ex-situ* TEM or EBSD measurements of austenite crystal orientation after inter-critical annealing in the two phase α/γ region. Therefore, in such experiments only the amount of stable austenite at room temperature is observable which can be significantly lower depending on the annealing temperature and chemical composition. Liu et al. [20,21] used *in-situ* CLSM to indicate austenite memory in super martensitic 13Cr—5Ni steel during continuous heating to the austenitization temperature of 830 °C. However, only the similar coarse grain size of freshly formed austenite compared to prior austenite grain size infers the presence of austenite memory phenomenon. Hence, no crystallographic information is analyzed for the determination of an orientation relationship between martensite and freshly formed austenite.

By *in-situ* high temperature EBSD measurements the actual work evidences directly the austenite memory phenomenon by analyzing austenite grain size and crystal orientation in PH 15-5 in the final stage of austenitization. It is shown that austenite memory is present in PH 15-5 at austenitization temperatures up to 850 °C and an austenite phase fraction of approximately 100%. All of the observed austenite has, according to CLSM and high temperature EBSD analysis, a lath-like morphology and exhibits a near KS-OR with martensite. Referring to actual literature [14–16,20,21] this austenite is referred to as acicular austenite.

KS is a common used model to describe the OR of the austenite to martensite transformation in low carbon steels, claiming that close packed planes and close packed directions of parent and daughter phase are parallel, *i.e.* $\{111\}_\gamma \| \{011\}_{\alpha'}$ and $\langle 011\rangle_\gamma \| \langle 111\rangle_{\alpha'}$ [43]. This OR causes 24 possible crystal orientations for martensite (*i.e.* variants) out of one austenite crystal orientation exhibiting a characteristic pattern in the (001) pole figure. For the reverse transformation from martensite to austenite with KS-OR every martensite variant has also theoretically 24 possible crystal orientations for reversed austenite. However, such behavior is not observed in the actual work. The EBSD data, especially Fig. 2e, show that only one austenite variant inside of a prior austenite grain is formed and its crystal orientation is equivalent to the crystal orientation of prior austenite and therefore causes austenite memory.

4.2. Assessment of the formation mechanism of austenite reversion

Four different mechanisms are described in literature for the formation of austenite memory involving (1) variant restriction between reversed austenite, cementite and martensitic laths [16,25], (2) diffusional growth of retained austenite [20,26] (3) diffusionless shear transformation [22] and (4) variant restriction between martensite laths and reversed austenite influenced by an internal stress field [19].

For mechanism (1) austenite nucleates adjacent to martensite lath boundaries and precipitated cementite. According to this theory a combination of Pitch OR from austenite to cementite and KS OR from austenite to martensite causes austenite memory [16,25]. However, no cementite is found in the PH 15-5 alloy by TEM or SEM due to the low carbon content of 0.032 m.%. Therefore, mechanism (1) can be excluded. Couturier et al. [1] reported enrichments of Ni and Mn surrounding Cu precipitates after inter-critical annealing which is an indicator for a potential austenite nucleation site. Cu precipitations with fcc crystal structure (*i.e.* overaged state) show a KS-OR with the martensitic matrix [3] and therefore a relation with austenite memory cannot be excluded. However, in the present work only the forged material condition without additional heat treatment is investigated and therefore it is assumed that Cu precipitates cannot achieve the overaged fcc state in a sufficient amount. Hence, Cu precipitates are not further considered as a source for austenite memory in the present work although the influence on austenite reversion kinetics due to trapping of Ni and Mn is still part of ongoing research.

Another potential nucleation site for reversed austenite is retained austenite. Although, thin films of inter-lath retained austenite can be present in soft martensitic steels [20], no retained austenite can be evidenced by XRD in the present material condition (Fig. 1a). Therefore, mechanism (2), *i.e.* the growth of retained austenite, is not further considered as main mechanism for austenite memory in the present work but the influence of small amounts of inter-lath retained austenite (*i.e.* austenite amounts under the XRD detection limit) on the austenitization is still part of ongoing research.

The previous results of dilatometry, XRD and EBSD exhibit a time-dependent transformation from martensite to austenite and therefore indicate a diffusion controlled austenitization mechanism for a heating rate of 3.3 °C/s which is the heating rate of the *in-situ* evidence of austenite memory by EBSD. The thermokinetic simulations underpin a diffusion controlled martensite to austenite transformation as the simulated austenite fractions are in good agreement with *in-situ* high temperature XRD measurements. Furthermore, *in-situ* CLSM observations of the austenitization treatment reveal the continuous appearance of a surface relief in course of the formation of austenite. This disagrees with the cascade-like appearance of the surface relief during austenitization caused by a diffusionless transformation mechanism observed by Shirazi et al. [22] and therefore contradict mechanism (3). Additionally, for austenite reversion by a shear mechanism, superheating above martensite/austenite equilibrium temperature T_0 is necessary and therefore predominantly takes place in alloys with low T_0 (*i.e.* high Ni/Cr ratio) or heating rates of 100 °C/s and above for low alloyed steels [28,44]. Therefore, a diffusionless shear reversion

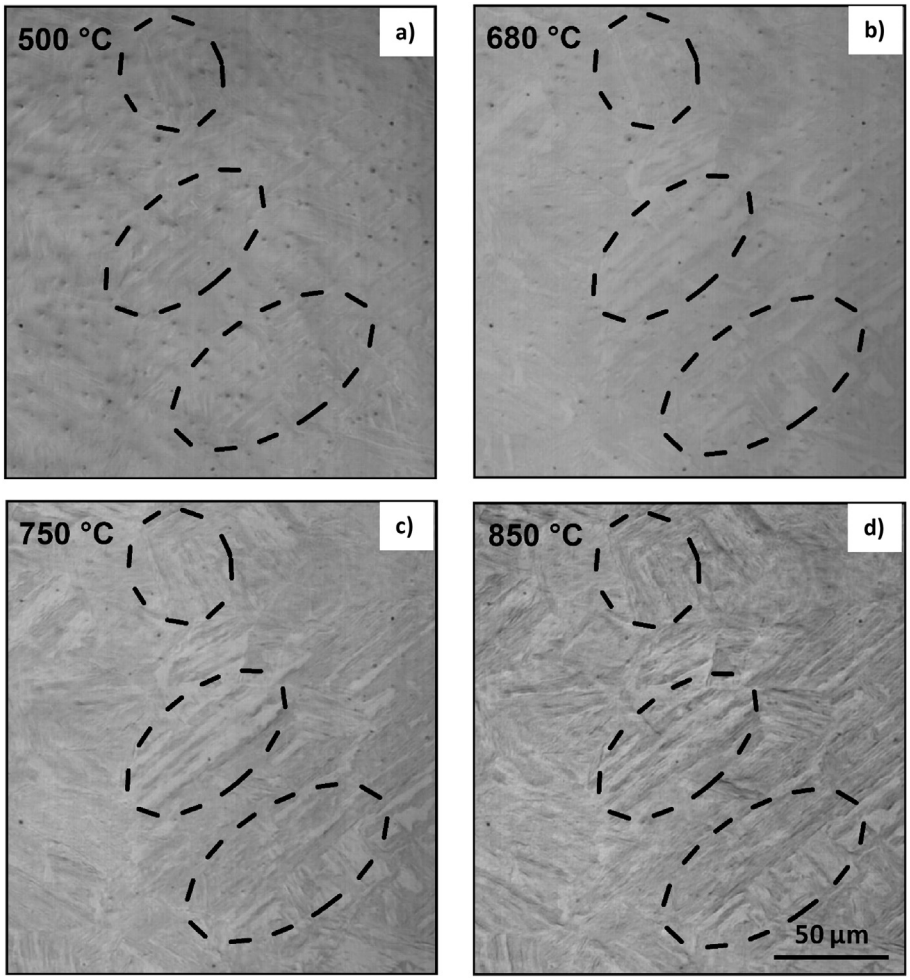

Fig. 6. Continuous appearance of a lath shaped surface relief between A_{c1} and A_{c3} parallel to martensitic substructure (CLSM).

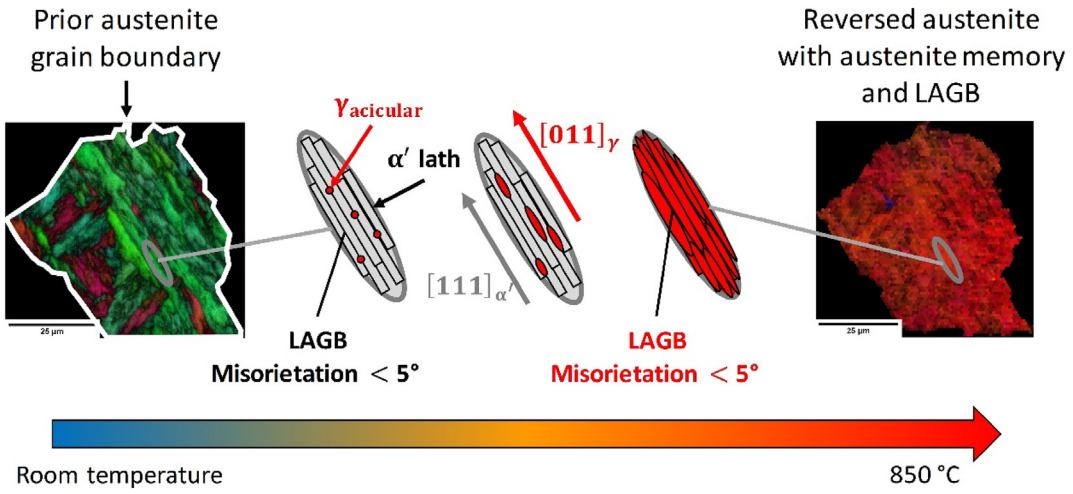

Fig. 7. Heritage of low angle grain boundaries (LAGB) by diffusion controlled austenite (γ) formation with variant restriction to martensite (α') laths.

(3) can also be excluded as feasible transformation mechanism for PH 15-5 and a heating rate of 3.3 °C/s.

According to this work mechanism (4), *i.e.* a variant restriction for reversed austenite nucleating on martensite lath boundaries, is the most probable. The results agree with the work of Nakada et al. [19] who suggested that for such variant restriction a combination of crystallographic limitations for nucleation (*i.e.* reduction of nucleation activation energy for $\{111\}_\gamma \| \{011\}_{\alpha'}$) and growth (*i.e.* reduction of interfacial energy for growth in $\langle 011\rangle_\gamma \| \langle 111\rangle_{\alpha'}$) and additionally internal stress fields of the martensitic microstructure are necessary. Additionally to martensite lath boundaries also packet, block and sub-block boundaries are reported as nucleation sites supporting austenite memory [16,17,19].

For mechanism (4) Nakada et al. [19] reports that austenite planes close to $\{111\}_\gamma$ are parallel to the martensite lath boundary plane $\{011\}_{\alpha'}$ and directions close to $[011]_\gamma$ are parallel to the$[111]_{\alpha'}$ longitudinal direction of the martensite lath. Hence, fresh formed austenite has a lath-like morphology (*i.e.* acicular austenite) which is nearly parallel to the longitudinal direction of the martensitic block-structure. This acicular shape of austenite is clearly visible for early stages of austenitization (*e.g.* after inter-critical annealing) [14,16]. In the present work, the lath-like morphology of reversed austenite parallel to martensitic block-structure observed with *in-situ* high temperature EBSD and CLSM (Figs. 2a, c and 6a–d respectively) gives an indication for the existence of acicular shaped austenite in the early stages of austenitization. Though, acicular austenite cannot be directly observed in separated regions as it is reported for inter-critical annealing experiments because of the advanced stage of austenitization and thus high fraction of austenite as well as the limited resolution as it is described in the following.

Zhang et al. [14] postulated that reversed austenite formed by mechanism (4) requires a coherent interface to the surrounding martensite laths. The martensite laths are separated by low angle grain boundaries (LAGB) with a misorientation up to 5° [45]. Therefore, coalescence of reversed austenite, nucleated and grown on neighboring martensitic laths with only a small orientation deviation, can lead to the generation of LAGB (*i.e.* geometrically necessary dislocations) in reversed austenite. The fluctuations of IQ inside the austenite grains observed by EBSD (Fig. 2c) indicates discontinuities of crystal orientations and gives a hint for the presence of LAGB. It is assumed that the width of acicular austenite regions is in the magnitude of martensitic lath width of approximately 200 nm and therefore cannot be resolved with an EBSD step size of 1 μm. Based on the presented comparison of literature with results of the actual work, a basic model is postulated in Fig. 7 which illustrates the nucleation and growth of reverted austenite based on mechanism (4) and furthermore describes the heritage of LAGB during austenitization due to coalescence of neighboring acicular austenite regions with coherent interface to the martensitic matrix.

These considerations are consistent to the work of Shinozaki et al. [30,31] which also discuss the potential misorientation enhancement inside austenite grains formed by mechanism (4). However, the chemical composition of the investigated low alloy steel distinguishes strongly from PH 15-5 and additionally contains an amount of approximately 4% cementite which makes it difficult to isolate mechanism (4) as the only present formation mechanism for austenite memory.

Recent literature [22,28,18] reports about a higher dislocation density of reversed austenite compared to prior austenite formed by a shear mechanism but not for diffusion controlled reversion. The actual work, however, suggests that the proposed diffusion controlled austenitization mechanism can also lead to an enhanced dislocation density which is distinctly higher than austenite formed by the classical diffusion controlled transformation (*i.e.* the migration of incoherent high angle grain boundaries).

5. Conclusions

The transformation mechanism of austenite reversion during continuous heating of the commercial alloy PH 15-5 was investigated in this study. The main results are summarized as follows:

- The austenite memory effect during austenitization is directly evidenced by *in-situ* high temperature electron back scatter diffraction in the PH15-5 alloy.
- According to the results of dilatometry, XRD, DICTRA simulations and CLSM, martensite transforms diffusion controlled to austenite during continuous heating with a heating rate up to 3.3 °C/s.
- Only reversed austenite with acicular shape, parallel to martensite block boundaries is observed by *in-situ* high temperature EBSD and CLSM measurements respectively for an austenitization temperature of 850 °C.
- A basic model for diffusion controlled acicular austenite formation and the inheritance of LAGB from martensite lath boundaries to acicular austenite is proposed.

CRediT authorship contribution statement

Dominik Brandl: Conceptualization, Methodology, Formal analysis, Writing - original draft. **Marina Lukas:** Formal analysis, Software, Writing - review & editing. **Martin Stockinger:** Resources, Writing - review & editing. **Sarah Ploberger:** Resources, Writing - review & editing. **Gerald Ressel:** Methodology, Formal analysis, Supervision, Writing - review & editing.

Acknowledgement

The research leading to these results has received funding from Take Off program. Take Off is a Research, Technology and Innovation Funding Program of the Austrian Federal Ministry for Transport, Innovation and Technology (BMVIT) (850471). The Austrian Research Promotion Agency (FFG) has been authorized for the Program Management.

The authors also gratefully acknowledge Dr. Seiichi Suzuki (TSL Solutions KK, Japan) for his support during the high temperature EBSD measurements and Nora Fuchs MSc (Montanuniversität Leoben, Chair of Ferrous Metallurgy, Austria) for the support during the CLSM measurements.

Data availability

The raw/processed data required to reproduce these findings cannot be shared at this time as the data also forms part of an ongoing study.

Appendix A. Supplementary data

Supplementary data to this article can be found online at https://doi.org/10.1016/j.matdes.2019.107841.

References

[1] L. Couturier, F. De Geuser, M. Descoins, A. Deschamps, Evolution of the microstructure of a 15-5PH martensitic stainless steel during precipitation hardening heat treatment, Mater. Des. 107 (2016) 416–425, https://doi.org/10.1016/j.matdes.2016.06.068.
[2] D. Ye, J. Li, W. Jiang, J. Su, K. Zhao, Effect of Cu addition on microstructure and mechanical properties of 15%Cr super martensitic stainless steel, Mater. Des. 41 (2012) 16–22, https://doi.org/10.1016/j.matdes.2012.04.036.
[3] H.R. Habibi Bajguirani, The effect of ageing upon the microstructure and mechanical properties of type 15-5 PH stainless steel, Mater. Sci. Eng. A 338 (2002) 142–159, https://doi.org/10.1016/S0921-5093(02)00062-X.
[4] J.W. Morris, Z. Guo, C.R. Krenn, Y. Kim, The limits of strength and toughness in steel, ISIJ Int. 41 (2001) 599–611, https://doi.org/10.2355/isijinternational.41.599.
[5] J.W. Morris, C. Kinney, K. Pytlewski, Y. Adachi, Microstructure and cleavage in lath martensitic steels, Sci. Technol. Adv. Mater. 14 (2013), 014208. https://doi.org/10.1088/1468-6996/14/1/014208.
[6] J.W. Morris Jr., On the ductile-brittle transition in lath martensitic steel, ISIJ Int. 51 (2011) 1569–1575, https://doi.org/10.2355/isijinternational.51.1569.
[7] E.I. Galindo-Nava, P.E.J. Rivera-Díaz-Del-Castillo, A model for the microstructure behaviour and strength evolution in lath martensite, Acta Mater. 98 (2015) 81–93, https://doi.org/10.1016/j.actamat.2015.07.018.
[8] E.I. Galindo-Nava, W.M. Rainforth, P.E.J. Rivera-Díaz-del-Castillo, Predicting microstructure and strength of maraging steels: elemental optimisation, Acta Mater. 117 (2016) 270–285, https://doi.org/10.1016/j.actamat.2016.07.020.
[9] G. Krauss, Martensite in steel: strength and structure, Mater. Sci. Eng. A 273–275 (1999) 40–57, https://doi.org/10.1016/S0921-5093(99)00288-9.
[10] A. Ghosh, S. Kundu, D. Chakrabarti, Effect of crystallographic texture on the cleavage fracture mechanism and effective grain size of ferritic steel, Scr. Mater. 81 (2014) 8–11, https://doi.org/10.1016/j.scriptamat.2014.02.007.
[11] A. Chatterjee, A. Ghosh, A. Moitra, A.K. Bhaduri, R. Mitra, D. Chakrabarti, The role of crystallographic orientation of martensitic variants on cleavage crack propagation, Philos. Mag. Lett. (2016) 1–18 Under revi.
[12] D. Raabe, S. Sandlöbes, J. Millán, D. Ponge, H. Assadi, M. Herbig, P.P. Choi, Segregation engineering enables nanoscale martensite to austenite phase transformation at grain boundaries: a pathway to ductile martensite, Acta Mater. 61 (2013) 6132–6152, https://doi.org/10.1016/j.actamat.2013.06.055.
[13] B.R. Kumar, S. Sharma, P. Munda, R.K. Minz, Structure and microstructure evolution of a ternary Fe – Cr – Ni alloy akin to super martensitic stainless steel, Mater. Des. 50 (2013) 392–398, https://doi.org/10.1016/j.matdes.2013.03.035.
[14] X. Zhang, G. Miyamoto, T. Kaneshita, Y. Yoshida, Y. Toji, T. Furuhara, Growth mode of austenite during reversion from martensite in Fe-2Mn-1.5Si-0.3C alloy: a transition in kinetics and morphology, Acta Mater. 154 (2018) 1–13, https://doi.org/10.1016/j.actamat.2018.05.035.
[15] P. Song, W. Liu, C. Zhang, L. Liu, Z. Yang, Reversed austenite growth behavior of a 13% Cr-5%Ni stainless steel during intercritical annealing, ISIJ Int. 56 (2016) 148–153, https://doi.org/10.2355/isijinternational.ISIJINT-2015-280.
[16] X. Zhang, G. Miyamoto, Y. Toji, S. Nambu, T. Koseki, T. Furuhara, Orientation of austenite reverted from martensite in Fe-2Mn-1.5Si-0.3C alloy, Acta Mater. 144 (2018) 601–612, https://doi.org/10.1016/j.actamat.2017.11.003.
[17] F. Niessen, Austenite reversion in low-carbon martensitic stainless steels – a CALPHAD-assisted review, Mater. Sci. Technol. 0836 (2018) 1–14, https://doi.org/10.1080/02670836.2018.1449179.
[18] N. Nakada, R. Fukagawa, T. Tsuchiyama, S. Takaki, D. Ponge, D. Raabe, Inheritance of dislocations and crystallographic texture during martensitic reversion into austenite, ISIJ Int. 53 (2013) 1286–1288, https://doi.org/10.2355/isijinternational.53.1286.
[19] N. Nakada, T. Tsuchiyama, S. Takaki, S. Hashizume, Variant selection of reversed austenite in lath martensite, ISIJ Int. 47 (2007) 1527–1532, https://doi.org/10.2355/isijinternational.47.1527.
[20] L. Liu, Z.G. Yang, C. Zhang, Effect of retained austenite on austenite memory of a 13% Cr-5% Ni martensitic steel, J. Alloys Compd. 577 (2013) S654–S660, https://doi.org/10.1016/j.jallcom.2012.04.021.
[21] L. Liu, Z.G. Yang, C. Zhang, W.B. Liu, An in situ study on austenite memory and austenitic spontaneous recrystallization of a martensitic steel, Mater. Sci. Eng. A 527 (2010) 7204–7209, https://doi.org/10.1016/j.msea.2010.07.083.
[22] H. Shirazi, G. Miyamoto, S. Hossein Nedjad, T. Chiba, M. Nili Ahmadabadi, T. Furuhara, Microstructure evolution during austenite reversion in Fe-Ni martensitic alloys, Acta Mater. 144 (2018) 269–280, https://doi.org/10.1016/j.actamat.2017.10.068.
[23] D. Ye, S. Li, J. Li, W. Jiang, J. Su, K. Zhao, Study on the crystallographic orientation relationship and formation mechanism of reversed austenite in economical Cr12 super martensitic stainless steel, Mater. Charact. 109 (2015) 100–106, https://doi.org/10.1016/j.matchar.2015.09.013.
[24] D. Brandl, L. Höfler, M. Stockinger, S. Ploberger, S. Marsoner, G. Ressel, Presentation and verification of an electrolytic etching technique for the determination of prior austenite grain boundaries in the steel PH15-5, Pract. Metallogr. 55 (2018) 800–812, https://doi.org/10.3139/147.110497.
[25] S. Watanabe, T. Kunitake, On the formation of austenite grains from prior martensitic structure, Tetsu-Do-Hagane 61 (1975) 96–106.
[26] S.T. Kimmins, D.J. Gooch, Austenite memory effect in 1Cr-1 Mo-O-75V (Ti, B) steel, Met. Sci. 17 (1983) 519–532.
[27] S.J. Lee, Y.M. Park, Y.K. Lee, Reverse transformation mechanism of martensite to austenite in a metastable austenitic alloy, Mater. Sci. Eng. A 515 (2009) 32–37, https://doi.org/10.1016/j.msea.2009.02.010.
[28] N. Nakada, T. Tschiyama, S. Takaki, D. Ponge, D. Raabe, Transition from diffusive to displacive austenite reversion in low-alloy steel, ISIJ Int. 53 (2013) 2275–2277.
[29] K. Tomimura, S. Takaki, Y. Tokunaga, Reversion mechanism from deformation induced martensite to austenite in metastable austenitic stainless steels, ISIJ Int. 31 (1991) 1431–1437, https://doi.org/10.2355/isijinternational.31.1431.
[30] T. Shinozaki, Y. Tomota, T. Fukino, T. Suzuki, Microstructure evolution during reverse transformation of austenite from tempered martensite in low alloy steel, ISIJ Int. 57 (2017) 533–539.
[31] Y. Tomota, W. Gong, S. Harjo, T. Shinozaki, Scripta Materialia Reverse austenite transformation behavior in a tempered martensite low-alloy steel studied using in situ neutron diffraction, Scr. Mater. 133 (2017) 79–82, https://doi.org/10.1016/j.scriptamat.2017.02.017.
[32] G. Faninger, Gezielte Untersuchungen zur quantitativen röntenographischen Phasenanalyse (RPA), HTM. 30 (1975) 231–244.
[33] A. Borgenstam, DICTRA, a tool for simulation of diffusional transformations in, 21 (2000) 269–280.
[34] F. Niessen, M. Villa, J. Hald, M.A.J. Somers, Kinetics analysis of two-stage austenitization in supermartensitic stainless steel, Mater. Des. 116 (2017) 8–15, https://doi.org/10.1016/j.matdes.2016.11.076.
[35] J.D. Escobar, G.A. Faria, L. Wu, J.P. Oliveira, P.R. Mei, A.J. Ramirez, Austenite reversion kinetics and stability during tempering of a Ti-stabilized supermartensitic stainless steel: correlative in situ synchrotron x-ray diffraction and dilatometry, Acta Mater. 138 (2017) 92–99, https://doi.org/10.1016/j.actamat.2017.07.036.
[36] C. Bernhard, S. Schider, A. Sormann, G. Xia, S. Ilie, Erste Ergebnisse des neuen Hochtemperatur-Konfokalmikroskops am Lehrstuhl fuer Metallurgie, Berg- Und Huettenmaennische Mont. 156 (2011) 161–167, https://doi.org/10.1007/s00501-011-0645-4.
[37] T. Nyyssönen, M. Isakov, P. Peura, V.T. Kuokkala, Iterative determination of the orientation relationship between austenite and martensite from a large amount of grain pair misorientations, Metall. Mater. Trans. A Phys. Metall. Mater. Sci. 47 (2016) 2587–2590, https://doi.org/10.1007/s11661-016-3462-2.
[38] S. Nambu, N. Shibuta, M. Ojima, J. Inoue, T. Koseki, H.K.D.H. Bhadeshia, In situ observations and crystallographic analysis of martensitic transformation in steel, Acta Mater. 61 (2013) 4831–4839, https://doi.org/10.1016/j.actamat.2013.04.065.
[39] C.N. Hsiao, C.S. Chiou, J.R. Yang, Aging reactions in a 17-4 PH stainless steel, Mater. Chem. Phys. 74 (2002) 134–142.
[40] Park, et al., Formation of reversed austenite during tempering of 14Cr-7Ni-0. 3Nb, Met. Mater. Int. 10 (2004) 521–525.
[41] U.K. Viswanathan, S. Banerjee, R. Krishnan, Effects of aging on the microstructure of 17-4 PH stainless steel, Mater. Sci. Eng. 104 (1988) 181–189, https://doi.org/10.1016/0025-5416(88)90420-X.
[42] S. Zhang, P. Wang, D. Li, Y. Li, Investigation of the evolution of retained austenite in Fe-13%Cr-4%Ni martensitic stainless steel during intercritical tempering, Mater. Des. 84 (2015) 385–394, https://doi.org/10.1016/j.matdes.2015.06.143.
[43] S. Morito, X. Huang, T. Furuhara, T. Maki, N. Hansen, The morphology and crystallography of lath martensite in alloy steels, Acta Mater. 54 (2006) 5323–5331, https://doi.org/10.1016/j.actamat.2006.07.009.
[44] H.K.D.H. Bhadeshia, Bainite in steels, Theory Pract. (2015) https://doi.org/10.1017/CBO9781107415324.004.
[45] J.G. Back, G. Engberg, Investigation of parent austenite grains from martensite structure using EBSD in a wear resistant steel, Materials (Basel) 10 (2017) https://doi.org/10.3390/ma10050453.